# The effects of fluid flow and epiphytes on submerged aquatic vegetation

A DISSERTATION
SUBMITTED TO THE FACULTY OF THE GRADUATE SCHOOL
OF THE UNIVERSITY OF MINNESOTA
BY

Amy Therese Hansen

IN PARTIAL FULFILLMENT OF THE REQUIREMENTS
FOR THE DEGREE OF
DOCTOR OF PHILOSOPHY

Advisors:
Dr. Miki Hondzo
Dr. Jacques Finlay

May 2012

# Acknowledgements

I am grateful for the guidance given to me by my advisors Miki Hondzo and Jacques Finlay. Both advisors generously provided their time, knowledge and insight. Both are excellent scientists, critical thinkers and have held me to a high standard throughout the PhD process. I thank Kimberly Hill and Heinz Stefan for the commitment they each made by being part of my committee. I have received valuable lessons relevant to both science and life from all committee members.

Financial support was provided by; the National Science Foundation's Integrative Graduate Education and Research Traineeship Program (NSF IGERT Grant No. DGE-0504195), the National Center for Earth-surface Dynamics (NCED), a Science and Technology Center funded by the office of Integrative Activities of the National Science Foundation (under agreement number EAR-0120914), the Dosdall Fellowship, the Silbermann Fellowship, and a Block grant from the University of Minnesota, Department of Ecology, Evolution and Behavior.

Chapter 2 was originally published in Hydrobiologia in 2011. Chapter 3 was originally published in Marine Ecology Progress Series in 2011. Complete citations for both are included in the References section of the dissertation.

I was fortunate to visit the laboratory of Catriona Hurd at the University of Otago, Duniden, New Zealand whose knowledge of kelp physiology and optimistic nature kept me on track with publishing chapter 3. Claudia Neuhauser, the PI for IGERT during my first 2 years, was a mentor and role model. Jian Sheng's interest, digital holographic

system and just in time programming were instrumental in completing the research in chapter 4. I am grateful to have had the opportunity to collaborate with Rebecca Stark, an EEB graduate student at the time, on Chapter 2. I learned from her focus on detail in experimental planning and in laboratory analysis.

I would like to acknowledge the many acts of indispensible generosity that I experienced during my dissertation work. During my stay in New Zealand, Chris Hepburn, Daniel Pritchard, and Stewart Bell, Department of Botany, University of Otago, provided assistance with kelp sample collection, experimental setup and kiwi wit. The researchers associated with the Angelo Coast Range Reserve, especially Mary Power, Paula Furey, and Mike Limm were generous hosts as well as collaborators, providing site identification, analyzing epiphyte assemblage composition, and collecting and sending algal samples. John Ferguson and Michael Sadowsky provided cultured algal samples freely and at a moment's notice. Sandy Brovold, Anika Bratt, John Jaka, Morgan Greenfield, and Laura Kimball assisted with water chemistry analysis and wetland sample collection for chapter 5. I had the good fortune to mentor two undergraduate students during graduate school, Jordan Theissen and Audra Huffmeyer, whose enthusiasm and excitement were as valued as their assistance. The City of Roseville Minnesota allowed me access to the Villa Park Wetland System and Capital Region Watershed District shared their data from previous years. Graduate students in IGERT, the Hondzo group, the Finlay group and the Sheng group all provided valuable knowledge, advice, encouragement and criticism.

With gratitude, I thank my MN family and friends that together formed my amazing support system throughout my PhD experience. I thank my parents for easing the financial burden of daycare by spending 1-2 days a week, as well as some sick days, caring for my children. My husband Scott was always willing to try to switch his work day around to accommodate my sometimes odd schedule. My parents, my brothers, Laura Kimball, Laura Hampton, and Cheryl Taylor have all provided emergency childcare for sick kids, intense work periods and late schedule switches.

# Dedication

I dedicate this dissertation to my husband, Scott Terry, whose love, respect, support and flexibility have made it possible for me to complete a PhD and raise two wonderful children simultaneously.

# Abstract

The intent of this research was to investigate the effects of fluid flow characteristics and epiphyte colonization on submerged aquatic vegetation (SAV) photosynthesis and dissolved material uptake. SAV, with its stems and leaves completely submerged in the water column, is strongly affected by both the physical characteristics of the water, such as dissolved material concentrations and fluid motion, and by factors that alter its interaction with the water, such as epiphyte colonization of SAV surfaces. The nature of these interactions was investigated through a series of four separate studies. First, through a laboratory mesocosm experiment, epiphyte uptake and SAV uptake of a dissolved contaminant (nickel) were shown to occur at different rates and due to different mechanisms. Second, a model of photosynthetic rates, based on mass transfer theory, was developed requiring only three parameters that accounted for the effect of water motion on photosynthetic rates. This model was experimentally validated with dissolved oxygen and velocity profiles over blades of giant kelp, *Macrocystis pyrifera*. Third, using two separate microscale velocity imaging methods, photosynthesis was shown to alter fluid motion near the surface of a *Cladophora spp*. filament by more than doubling velocity gradients and thus surface shear stress. In this investigation, bacterial epiphytes had no effect on shear stresses but assemblages consisting primarily of diatom epiphytes strongly decreased the surface shear stress from what would have been experienced during photosynthesis without epiphytes present; indicating a harmful interaction with

epiphytes. Fourth, in agreement with the microscale results in the third study, epiphyte removal was shown to increase local dissolved oxygen concentrations throughout the water column as well as decrease water column soluble reactive phosphorus concentrations due to higher photosynthetic rates in field research in a constructed wetland. In a related laboratory study, epiphyte detachment rates were functionally related to water velocity. Overall, I have shown through laboratory and field experiments that SAV photosynthesis is closely linked to fluid flow characteristics, SAV and epiphyte uptake are not equally affected by flow conditions, and epiphyte colonization decreases SAV photosynthetic rates.

# Table of Contents

**ACKNOWLEDGEMENTS** ..... **I**

**DEDICATION** ..... **IV**

**ABSTRACT** ..... **V**

**TABLE OF CONTENTS** ..... **VII**

**LIST OF TABLES** ..... **IX**

**LIST OF FIGURES** ..... **X**

**CHAPTER 1 INTRODUCTION** ..... **1**

1.1 RESEARCH SIGNIFICANCE ..... 1
1.2 OBJECTIVES ..... 4
1.3 OVERVIEW OF DISSERTATION ..... 5
1.4 OVERALL CONCLUSIONS ..... 8

**CHAPTER 2 UPTAKE OF DISSOLVED NICKEL BY *ELODEA CANADENSIS* AND EPIPHYTES INFLUENCED BY FLUID FLOW CONDITIONS** ..... **10**

2.1 INTRODUCTION ..... 11
2.2 MATERIALS AND METHODS ..... 14
*2.2.1 Model of Nickel Uptake* ..... *14*
*2.2.2 Description of mesocosm* ..... *16*
*2.2.3 Measurement procedure* ..... *19*
2.3 RESULTS ..... 21
*2.3.1 Mesocosm conditions* ..... *21*
*2.3.2 Flow characteristics* ..... *23*
*2.3.3 Nickel uptake* ..... *25*
*2.3.4 Relating nickel uptake to flow conditions* ..... *27*
2.4 DISCUSSION ..... 29
2.5 CONCLUSION ..... 33

**CHAPTER 3 PHOTOSYNTHETIC OXYGEN FLUX BY *MACROCYSTIS PYRIFERA*: A MASS TRANSFER MODEL WITH EXPERIMENTAL VALIDATION** ..... **35**

3.1 INTRODUCTION ..... 35
3.2 METHODS ..... 39
*3.2.1 Model derivation* ..... *39*
*3.2.2 Flux estimation for no flow condition* ..... *43*
*3.2.3 Sample collection and preparation* ..... *43*
*3.2.4 Laboratory experiments* ..... *44*
3.3 RESULTS ..... 47
*3.3.1 Flow conditions* ..... *47*
*3.3.2 Dissolved oxygen* ..... *51*
*3.3.3 Local surface oxygen flux* ..... *53*

*3.3.4 Blade averaged surface oxygen flux* ..... *54*
*3.3.5 NPP estimate for entire kelp forest* ..... *55*
3.4 DISCUSSION ..... 56
3.5 SUPPLEMENT: DETAILED MODEL DERIVATION ..... 60

**CHAPTER 4 PHOTOSYNTHESIS INCREASES SURFACE SHEAR STRESS INSIDE ALGAL MATS ..... 64**

4.1 INTRODUCTION ..... 65
4.2 METHODS ..... 67
*4.2.1 Field velocity measurements* ..... *67*
*4.2.2 Sample preparation* ..... *68*
*4.2.3 Laboratory experimental setup* ..... *69*
*4.2.4 Light-dark experimental setup* ..... *70*
*4.2.5 Determination of the velocity gradient* ..... *71*
4.3 RESULTS ..... 72
4.4 DISCUSSION ..... 78
*4.4.1 Nutrient uptake* ..... *78*
*4.4.2 Bubbles* ..... *80*
*4.4.3 Epiphyte colonization* ..... *81*
*4.4.4 Surface roughness* ..... *82*
4.5 CONCLUSION ..... 83

**CHAPTER 5 EPIPHYTES DECREASE SUBMERGED AQUATIC VEGETATION UPTAKE OF PHOSPHORUS IN A CONSTRUCTED WETLAND ..... 84**

5.1 INTRODUCTION ..... 85
5.2 METHODS ..... 88
*5.2.1 Site description* ..... *88*
*5.2.2 Field measurements and sample collection* ..... *89*
*5.2.3 Laboratory analysis* ..... *91*
*5.2.4 Epiphyte removal rates* ..... *92*
*5.2.5 Treatment mechanism* ..... *93*
5.4 RESULTS ..... 94
*5.3.1 Dissolved oxygen* ..... *94*
*5.3.2 SRP concentrations* ..... *98*
*5.3.3 Treatment quantification and mechanism* ..... *99*
*5.3.4 Epiphyte removal rates* ..... *102*
*5.3.5 Environmental conditions* ..... *103*
5.5 DISCUSSION ..... 104
*5.4.1 Dissolved oxygen* ..... *104*
*5.4.2 SRP concentrations* ..... *105*
*5.4.3 Treatment mechanism* ..... *106*
*5.4.4 Effect of flow on epiphyte removal rates* ..... *107*

**BIBLIOGRAPHY ..... 109**

# List of Tables

2.1. Experimental conditions within mesocosm.....22

2.2. Coefficients generated from model of nickel uptake. .....27

3.1. Experimental DO data used in flux model for five replicate blades .....45

3.2. Flow characteristics based on experimental velocity profiles above *M. pyrifera* blades. .....50

5.1. Physical conditions during wetland sampling events.....97

5.2. Treatment removal effect .....101

# List of Figures

1.1. Conceptual diagram illustrating SAV-epiphyte interactions. .....4

2.1. Schematic and photographs of experimental mesocosm, in a re-circulating flume ...18

2.2. Span-wise averaged root mean square velocity profiles for all flow conditions. .....24

2.3. Turbulent intensities profiles taken a) in the open channel in front of the *E. canadensis* canopy and b) in mid-canopy. .....25

2.4. Experimental measurements of nickel concentration over time (symbols) and nickel flux model (dashed and solid lines). .....26

2.5. Relationships between nickel uptake parameters and canopy Reynolds number for epiphytes and *E. canadensis* .....28

2.6. $Re_c Sc^{-1/2}$ versus Sh for *E. canadensis* and epiphytes. .....29

3.1. Schematic representation of mass transfer system above kelp blade within flume setup. .....40

3.2. Comparison between experimental velocity and concentration profile data and power functions used in model. .....49

3.3. Relationship between local Reynolds number, $Re_x$ and the parameters $a_c$ and n used in the model.....52

3.4. Measured DO concentration, $C_s$, on the surface of all kelp blades. .....53

3.5. Variation of local surface DO flux from blade, $J_s$ with $Re_x$.....55

3.6. Relationship between mass transfer velocity k and $u_\infty$ based on numerical solution to Eq. 9 .....56

4.1. $\mu$PIV system schematic .....70

4.2. A. Photograph of the mat of *Cladophora* where velocity through the mat was measured. B. Vertical time-averaged stream-wise velocity profiles through mat. C. Reynolds stresses, $-\overline{u'w'}$ ($m^2$ $s^{-2}$) do not extend into the mat. .....74

4.3. A. Illustration of time-averaged velocity data as measured using μPIV. B. Time-averaged and spatially averaged velocity profiles next to a single filament .....76

4.4. A. Microscope images of some of the filaments used for the experiments. B. Experimental results demonstrating the relationship between the drag coefficient, $C_D$, and the Reynolds number, Re. .....77

4.5. Bubbles at *Cladophora* surface .....82

5.1. Field site and sampling setup .....90

5.2. Seasonal dissolved oxygen measurements within SAV canopy. .....95

5.3. Dissolved oxygen at the air-water interface as function of solar radiation .....96

5.4. DO profiles within SAV canopy before and after epiphyte removal for 4 sampling events .....98

5.5. SRP profiles within the SAV canopy before and after epiphyte removal for 4 sampling events .....100

5.6. Vertical DO profiles from treatment mechanism study. .....102

5.7. Average water SRP concentrations from treatment mechanism study. .....103

5.8. Relationship between epiphyte removal and Reynolds number as measured in a laboratory flow cell.....104

# Chapter 1 Introduction

## 1.1 Research significance

Submerged aquatic vegetation (SAV), consisting of aquatic plants and attached macroalgae, is present in surface waters worldwide. SAV influences its surrounding environment through altering water motion, uptake and release of dissolved materials, shading incoming irradiation from reaching the benthos, and as habitat for other organisms. In shallow lakes, aquatic macrophytes are attributed with maintaining water quality through nutrient drawdown, and sediment stabilization (Madsen et al. 2001). In oceanic coastal waters, SAV largely consists of macroalgae such as kelp, and alters coastal hydrodynamics and transport (Rosman et al. 2007) as well as serving as the foundation for coastal marine habitats (Graham et al. 2007). SAV also includes less desirable forms such as the attached filamentous alga *Cladophora glomerata*, common in eutrophic systems and credited with harboring elevated concentrations of pathogenic bacteria (Whitman et al. 2003, Vanden Heuvel et al. 2010).

Through photosynthesis and other uptake processes, such as absorption, adsorption and passive diffusion, aquatic plants and algae modify the chemical characteristics of surface waters. In low nutrient or low light conditions, photosynthetic rates may be constrained by resource availability and photosynthesis is said to be mass transfer or light limited. For example, in the ocean in the summer when demand for C and N is high, the water near algal surfaces can become depleted and growth may be limited by the rate of nutrient replenishment in water near the plant surface (Hepburn &

Hurd 2005). In contrast, in highly eutrophic environments, such as a wetland, where dissolved organic material and suspended sediment concentrations are high, light extinction can be rapid (Pokorny et al. 1984, Chimney et al. 2006) and growth may be light limited (Higgins et al. 2008, Asaeda et al. 2004).

Mass transfer of dissolved materials to SAV surfaces is controlled by fluid motion and material concentration within the fluid (e.g. Kays et al 2005). In turn, SAV canopies modify fluid motion and thus the delivery of the dissolved materials to SAV surfaces (Nepf & Ghisalberti 2008). SAV canopies decrease mean velocities within the canopy and create a shear layer near the top of the canopy by resisting movement in the flow direction and breaking apart larger eddies (Ghisalberti & Nepf 2002). The shear layer enhances vertical mixing through the generation of coherent, canopy scale eddies that, in sparse canopies, can penetrate to the substrate surface (Raupach et al. 1996, Ghisalberti & Nepf 2002, Nepf & Ghisalberti 2008). Macroscale changes in fluid flow characteristics have been shown to alter the exposure of SAV to dissolved substances and thus alter photosynthetic rates and uptake (Wheeler 1980, Hurd et al. 1996, Enriquez & Rodriguez-Roman 2006). At high velocities, physical damage or stress responses may occur. At low velocities or in stagnant fluid diffusive flux rates to and from the plant surface can be slower than the physiological capacity of SAV and limit physiological processes (Hurd 2000). For example, in dense canopies, such as algal mats, or canopies submerged within the benthic boundary layer, uptake is driven by diffusion processes near the cell surfaces. Although discussed conceptually by (Larned et al. 2004), the effect of fluid motion on

uptake at low velocities has not been studied at the microscale at which these processes occur.

SAV surfaces provide important habitat for microbial organisms, referred to collectively as epiphytes, such as algae, diatoms, bacteria, fungus, and animals that form the base of the aquatic food web. Epiphytes contribute to dissolved material cycling through effects on SAV metabolism and uptake and through their own uptake (e.g. Koch 1994, Lakatos et al. 1999). Understanding the potential impact of epiphytes on overall dissolved contaminant removal in various flow conditions would allow phytoremediation practitioners to manage for favorable levels of epiphyte colonization of SAV. Although small, the potential impact of microscopic organisms on dissolved material concentrations is great due to their rapid cycling and abundance (Pelton et al. 1998). Epiphyte abundance is greatly magnified by SAV; which has been referred to as a 'surface multiplier', due to the enhanced colonizable surface area they provide. For example, the filamentous algae *Cladophora* is estimated to increase underwater surface area by 2000-20,000 times what would be available from only the benthos (Power et al. 2009).

There is no consensus in the literature regarding the effect of epiphytes on the host plant: studies support harmful, beneficial and neutral effects. Epiphytes, generally considered more palatable to grazers, may benefit the host plant by deflecting grazing pressure (Hutchinson 1975). Epiphytes are reported to harm the SAV host by competing for nutrients and light (Sand-Jensen 1977, Sand-Jensen et al. 1985, Roberts et al. 2003) (Fig. 1.1). Other studies report a mutualistic nutrient cycle in which nutrient leaching

from plant tissue benefits the epiphytes (Moeller 1988, Burkholder et al. 1990) and conversely, nutrient release from microbial turnover is easily accessed by the plant, thus overcoming the otherwise nutrient replete boundary layer (Fig. 1.1). The presence of epiphytes on the SAV surface has also been reported to enhance nutrient availability by increasing the surface roughness (Koch 1994). The research presented in this dissertation adds to the understanding of epiphyte effects on SAV and how fluid motion alters these effects

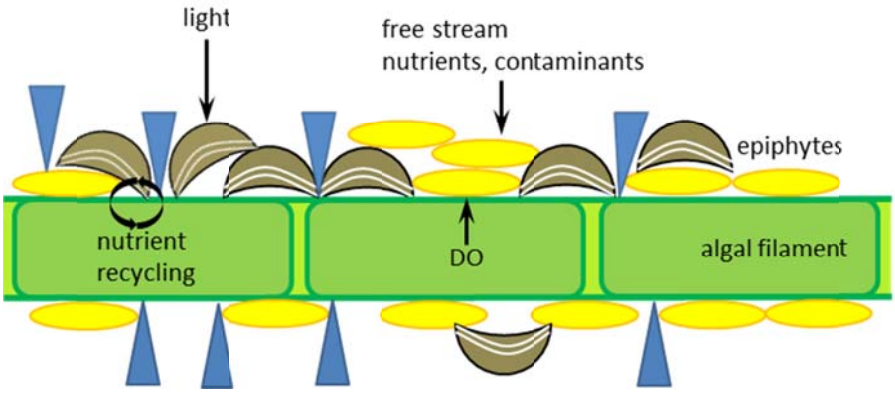


**Fig. 1.1** Conceptual diagram illustrating SAV-epiphyte interactions.

## 1.2 Objectives

The purpose of this research was to examine the interrelationship of SAV, epiphytes and fluid motion in order to predict their impact on dissolved material cycling. This is approached with three objectives in mind:

1. Examine the effect of SAV on fluid flow characteristics.

2. Examine the effect of fluid flow characteristics on dissolved materials uptake by SAV and epiphytes.

3. Determine the effect of epiphytes on SAV dissolved material uptake.

The above objectives were investigated in four separate studies on 3 different SAV species; a freshwater submerged macrophyte, *Elodea canadensis*, a marine macroalga, *Macrocystis pyrifera*, and a filamentous alga, *Cladophora glomerata*. Laboratory and field experiments were used to quantify all objectives.

The effect of SAV on fluid flow characteristics (Objective 1) was investigated at the microscale, at which nutrient exchange occurs, near the surface of *Cladophora glomerata*, using μPIV techniques (Chapter 4). The effect of fluid flow characteristics on dissolved material uptake (Objective 2) was studied for uptake of dissolved nickel by *E. canadensis* and its associated epiphytes (Chapter 2) and for modeling photosynthetic rates of *M. pyrifera* (Chapter 3). Photosynthesis can be thought of as an uptake and release process, where dissolved carbon and nutrients are taken up from the water column and oxygen is released back into the water column. The effect of epiphytes on dissolved material uptake was quantified in three studies on three different processes; heavy metal uptake in a re-circulating flume (Chapter 2), phosphorus drawdown in a constructed wetland (Chapter 5), and microscale photosynthetic rates (Chapter 4).

## 1.3 Overview of dissertation

Chapter 2 addresses the second and third objectives, listed above, in a laboratory experiment using live plants and epiphytes grown in a re-circulating flume. Dissolved

nickel uptake by the SAV-epiphyte complex was measured under a range of flow conditions. A flux model was developed and applied to the measured tissue nickel concentration data and generated three parameters descriptive of nickel uptake; uptake rate, equilibrium concentration, and time to equilibrium. The relationship of these parameters to flow conditions, represented by the dimensionless variable Reynolds number, was compared between epiphytes and plants. Water flow was shown to have a stronger effect on the uptake performance of epiphytes than that of plants, implying that water-side mass transfer plays a more important role in epiphytic nickel uptake than it does in plant nickel uptake. Although nickel concentrations were much higher in the epiphyte community than in *Elodea canadensis*, more total nickel was sequestered in *E. canadensis*. This research indicates that fluid flow conditions alter nickel uptake by *E. canadensis* and the epiphytic community and that the two have different preferential flow regimes.

Chapter 3 also investigates the effect of fluid flow on dissolved material uptake (Objective 2) through the development of a mass transfer model to determine rates of photosynthetic oxygen flux from the giant kelp, *Macrocystis pyrifera* in a moving fluid. The model can be used to calculate local dissolved oxygen flux, blade averaged oxygen flux and daily average net primary productivity for a kelp forest. Predicted rates of photosynthetic oxygen flux agree well with previously reported direct measurements. This model was derived from the fundamental principles of conservation of mass and momentum over a flat plate using an integral method approach and is applicable in laminar, transitional and turbulent flows. It predicts oxygen flux as an explicit function

of fluid flow conditions above the kelp blade. Experimental velocity profiles and dissolved oxygen concentration profiles, measured under a range of fluid flow conditions, followed power-law scaling and demonstrated local similarity between oxygen and velocity distribution within the boundary layers above the kelp blade. The proposed model provides a useful tool for estimating rates of photosynthesis with minimal data collection.

Chapter 4 explores the effect of SAV on fluid flow characteristics (Objective 1) at the microscale at which dissolved material uptake through SAV surfaces is occurring. The impact of epiphyte assemblages at this scale is also quantified (Objective 3). Chapter 4 describes a laboratory experiment investigating the effect of micro-scale surface characteristics, altered by the presence and type of epiphytes, on surface shear stress, or local skin drag, and thus indirectly, nutrient availability. Surface shear stresses on filamentous algae were found to be higher during photosynthesis than when the alga was not actively photosynthesizing and that the presence of attached diatom assemblages reduces this affect. An enhanced local shear stress creates a positive feedback loop where, by increasing local shear rates, nutrient concentration boundary layers also become thinner, increasing the rate of metabolic exchange, and thus increasing photosynthetic flux. This could be an important mechanism to overcome diffusion limited nutrient supply within a dense algal mat thereby self-promoting *Cladophora* survival.

In chapter 5, the effect of epiphytes on water column concentrations of soluble reactive phosphorus (SRP) and dissolved oxygen (DO) inside a SAV canopy (Objective

3) within an urban constructed wetland was investigated. Further, epiphyte detachment was investigated under controlled laboratory conditions. The results showed that water column DO increased after epiphyte removal for all depths and on all sample dates. SRP concentrations also decreased after epiphyte removal. Above a minimum velocity threshold, epiphyte detachment rates were linearly related to discharge velocity. The findings could be used to better design and operate constructed wetlands through active management of the SAV epiphyte load.

## 1.4 Overall conclusions

Although each of these studies was conducted in systems that varied in many important ways, some general conclusions can be drawn.

All SAV access metabolically required substances such as nitrogen and phosphorus from the water column (although submerged macrophytes may supplement this supply through root access to sedimentary materials) and release metabolic byproducts, mainly oxygen, back into the water column. Therefore, although photosynthetic rates will vary by species and light availability, the conclusions drawn in Chapters 3 and 4, that photosynthesis modifies mass and momentum transfer near SAV surfaces, should be universal. Depending on the flow rate and the SAV metabolic rate, photosynthesis could induce higher surface shear stresses for all SAV (Chapter 4). Depending on the blade or leaf morphology and the flow conditions, photosynthetic rates for other species could be modeled using the model presented in Chapter 3. These results

show fluid flow characteristics and SAV dissolved material uptake are tightly intertwined.

The results for nickel uptake (Chapter 2), that SAV had a larger contribution to dissolved nickel uptake than epiphytes under all flow conditions, may not be applicable to other metals or other SAV species. The capacity to uptake dissolved heavy metals is species specific and *E. canadensis* has been shown to be a heavy accumulator of dissolved nickel (Fritioff & Greger 2003, Samecka-Cymerman & Kempers 2003). Epiphyte abundance and assemblage composition can also vary widely across water bodies and host SAV species (Gross et al. 2003). Equally, the conclusions from Chapter 5 relating epiphyte contribution to phosphorus concentrations in a constructed wetland are dependent on epiphyte abundance and assemblage composition, SAV species photosynthetic rate and access to sedimentary phosphorus pools. One general conclusion of this work is that epiphytes can have a large effect on dissolved material cycling and uptake rates and mechanisms are not the same as SAV.

# Chapter 2 Uptake of dissolved nickel by *Elodea canadensis* and epiphytes influenced by fluid flow conditions

Using a laboratory mesocosm consisting of live plants and epiphytes grown in a re-circulating flume, dissolved nickel uptake by *Elodea canadensis* Michaux is compared with nickel uptake by the associated epiphytic community under a range of flow conditions. A flux model was developed and applied to the measured tissue nickel concentration data and generated three parameters descriptive of nickel uptake; uptake rate, equilibrium concentration, and time to equilibrium. The relationship of these parameters to flow conditions, represented by the dimensionless variable Reynolds number, was compared between epiphytes and plants. Water flow was shown to have a stronger effect on the uptake performance of epiphytes than that of plants, implying that water-side mass transfer plays a more important role in epiphytic nickel uptake than it does in plant nickel uptake. Although nickel concentrations were much higher in the epiphyte community than in *E. canadensis*, more total nickel was sequestered in *E. canadensis*. This research indicates that fluid flow conditions alter nickel uptake by *E. canadensis* and the epiphytic community and that the two have different preferential flow regimes. It also suggests the promising bioremediation potential of both in moving fluids in aquatic environments.

## 2.1 Introduction

Aquatic plants have received much attention recently for their potential use for bioremediation of heavy metals in contaminated surface waters (Dhir et al. 2009, Rai 2009). Phytoremediation is especially promising for removing low dose metal contamination where more traditional methods are either not effective or costly. Submerged aquatic macrophytes and floating plants remove metals directly from the surrounding water as well as from the sediment (Weis & Weis 2004). The submerged aquatic macrophyte *Elodea canadensis* (Michaux) has been identified to have potential for phytoremediation due to its ability to accumulate heavy metals in eutrophic water (Fritioff & Greger 2003, Samecka-Cymerman & Kempers 2003). Nickel is taken up by aquatic macrophytes both actively via ion transport systems (Chen et al. 2009) and passively through adsorption and absorption (Dhir et al. 2009).

Aquatic macrophytes often grow in association with epiphytic microbial communities consisting of bacterial, algal, and fungal microorganisms. Gosselain et al. (2005) found that *E. canadensis* had the highest epiphytic biomass of the five macrophytes in their study. Field studies have shown that epiphytes and macrophytes uptake heavy metals at differing capacities (Lakatos et al. 1999, Kljakovic-Gaspic et al. 2004, Schlacher-Hoenlinger & Schlacher 1998). Differences in uptake rates and equilibrium concentrations between macrophytes and epiphytes may be due to the relative importance of mass transfer versus kinetics and macrophyte-epiphyte interactions. Due to their small size, epiphytes have a high surface area to volume ratio and adsorption may be a dominant uptake mechanism (Haferburg & Kothe 2007).

Water motion has been demonstrated to have a strong influence on macrophyte and epiphyte metabolism, affecting photosynthesis and nutrient acquisition (Koch 1994, Hurd et al. 1996, Baldy et al. 2007). In return, plant-epiphyte communities, called submerged canopies, influence water motion by creating a shear layer due to resisting movement in the flow direction and breaking apart larger eddies (Ghisalberti & Nepf 2002). The shear layer at the top of a submerged canopy enhances vertical mixing through the generation of coherent, canopy scale eddies that, in sparse canopies, can penetrate to the sediment surface (Raupach et al. 1996, Ghisalberti & Nepf 2002). Some characteristics of a mixing layer include an inflection in the mean velocity profile and vertical heterogeneity in Reynolds stresses within the canopy, (Raupach et al. 1996). Higher flow rates and turbulence result in thinner diffusive boundary layers at the plant surface and higher mass transfer rates (Kays et al. 2005). The presence of epiphytes on the macrophyte surface could either enhance the mass transfer effects of turbulence by increasing the surface roughness (Koch 1994) or the epiphytes may shield the macrophytes surface and create a thicker diffusive boundary layer (Sand-Jensen et al. 1985).

Experiments to date have reported nickel uptake by aquatic plants either under controlled laboratory settings where ambient nickel concentration is varied in a stagnant fluid (e.g. Kahkonen & Manninen 1998, Maleva et al. 2009) or have collected field data comparing biotic heavy metal concentrations in various water bodies without characterizing the fluid flow environment (e.g. Mortimer 1985, Samecka-Cymerman & Kempers 2003). These approaches contribute important insights regarding the biotic

mechanism of heavy metal uptake in the former and metal fate in the environment in the latter, but do not address the potential coupling of fluid flow conditions with nickel uptake. Although there are many studies that examine the relationship between flow conditions and uptake of macronutrients by submerged macrophytes or macroalgae (e.g. Koch 1994, Hurd et al. 1996), we are not aware of any that have quantified the effect of flow conditions on heavy metal uptake by macrophytes or epiphytes. In field studies, where fluid flow conditions are not quantified, heavy metal concentrations in epiphytes have been shown to be quite different than in their macrophyte hosts (Lakatos et al. 1999, Kljakovic-Gaspic et al. 2004, Schlacher-Hoenlinger & Schlacher 1998). Cornelisen and Thomas (2002, 2006) have elaborated how flow conditions affect nitrogen uptake by seagrass and the associated epiphyte community and found that epiphytes accounted for the largest uptake level and epiphytic uptake was controlled by mass transfer. As heavy metals are essential micronutrients yet toxic in large quantities, uptake patterns of micronutrients are not expected to behave similarly to macronutrient uptake.

This study is the first to examine the relationships between nickel uptake and fluid flow conditions in both epiphytes and macrophytes. By creating a laboratory mesocosm within a re-circulating flume, it was possible to vary fluid flow conditions and measure nickel concentration responses beyond what could have been done in a field study. At the same time, the mesocosm consisted of living plants populated with a naturally colonizing epiphyte community, similar to what would been found in the natural environment and in contrast to the idealized array of cylinders often used in engineering studies on the effects of flow conditions on mass transfer.

## 2.2 Materials and methods

### *2.2.1 Model of Nickel Uptake*

The rate of change in nickel concentration over time within the control volume around the plant or epiphyte due to uptake from the surrounding water can be expressed as:

$$\frac{dC}{dt} = \frac{W(t)}{V} - \lambda C \qquad (2.1)$$

where C (mg Ni (g DW)$^{-1}$) is the nickel concentration in the plant or epiphyte, t (s) is the time since nickel addition to the system, W(t) (m s$^{-1}$) is the rate that nickel is entering the control volume around the plant or epiphyte, in this case a step function, V (m$^3$) is the plant or epiphyte volume, and $\lambda$ (s$^{-1}$) is the rate of uptake. Note that $\lambda$ captures both water-side, mass transfer controlled uptake and plant-side, kinetic controlled uptake. Assuming $\lambda$ and V are constant, the initial tissue nickel concentration is $C_o$, and that after a large time the concentration approaches an equilibrium concentration, $C_{eq}$, Eq. 2.1 can be integrated and results in an expression for the tissue nickel concentration as a function of the exposure time,

$$C(t) = C_o e^{-\lambda t} + C_{eq}(1 - e^{-\lambda t}) \qquad (2.2)$$

The nickel flux, J (kg m$^{-2}$ s$^{-1}$), across the plant or epiphyte frontal surface area, $A_{fr}$ (m$^2$), is defined as the rate of change of the nickel concentration, dC dt$^{-1}$, within the control volume:

$$\int_{A_f} -J \cdot \hat{n} dA = \int_{C.V.} \frac{dC}{dt} dV \qquad (2.3)$$

After integrating both sides of Eq. 2.3 and evaluating J at t = 0, when the flux is maximum,

$$J = \left( \frac{V}{A_{fr}} \right) \lambda \left( C_{eq} - C_0 \right) \qquad (2.4)$$

The flux can be expressed non-dimensionally as the Sherwood number (Sh); the ratio of the total mass transfer to the diffusive mass transfer: $Sh = J_{total}/J_{diffusive}$. A Sherwood number of one indicates that flux is purely due to molecular diffusive transport and reaction kinetics such as in non-moving fluid. A Sherwood number greater than one indicates that fluid motion is enhancing uptake. To examine the effect of water motion on nickel uptake, Sh is commonly expressed as a function of two other dimensionless variables, the Schmidt number, $Sc = \nu/D$ where $\nu$ ($m^2\ s^{-1}$) is the kinematic viscosity, and D ($m^2\ s^{-1}$) is the diffusion coefficient, and a characteristic Reynolds number, $Re = uL/\nu$, where u ($m\ s^{-1}$) and L (m) are characteristic velocity and length scales, respectively. The Reynolds number is the dimensionless ratio of inertial forces to viscous forces. Low Reynolds number flows tend to be less turbulent that high Reynolds number flows.

Due to the dominance of canopy scale eddies, much of the turbulence within the canopy is not locally generated (Raupach et al. 1996), and a measure of velocity that accounts for the turbulent fluctuations within the entire flow field is appropriate (Cornelisen & Thomas 2006). For this reason, the characteristic velocity scale used to

describe nickel flux is the mid-canopy, profile averaged root-mean-square velocity, $\langle u_{rms} \rangle$ (m $s^{-1}$), defined as:

$$\langle u_{rms} \rangle = \sqrt{\frac{1}{3}\left(\langle \overline{u'^2} \rangle + \langle \overline{v'^2} \rangle + \langle \overline{w'^2} \rangle\right)} \qquad (2.5)$$

where u', v', w', are the fluctuating velocity components in the stream-wise, span-wise and vertical direction. The triangular brackets $\langle\ \rangle$ signify spatial averaging and the overbar indicates temporal averaging. The effective height of the canopy, $h_c$ (m), is used as the characteristic length scale since canopy geometry drives the flow characteristics. Other canopy length scales, such as plant spacing or stem diameter have been used as the characteristic length scale for canopy flow studies but these don't lend themselves well to the heterogeneity found when using real plants. Effective canopy height is defined as the point of inflection in the mean velocity profile (Raupach et al. 1996). For the analysis presented in this paper, Reynolds number, $Re_c$, is defined as:

$$Re_c = \frac{\langle u_{rms} \rangle h_c}{\nu} \qquad (2.6)$$

### *2.2.2 Description of mesocosm*

A laboratory mesocosm consisting of live *E. canadensis* plants, colonized with epiphytes and held in place by a washed sand substrate, was constructed in a 1065 L variable flow rate, re-circulating flume (Fig. 2.1). For each experiment, 50 live *E. canadensis* plants, canopy density of 122 plants $m^{-2}$, were arranged in ten rows placed 10 cm apart with five plants per row spaced 8 cm apart and staggered to minimize wake interference. The foremost row was 2.6 m downstream from the channel entrance to

minimize entrance effects. The flume channel dimensions were 0.31 m height, 0.47 m width, and 5.2 m length emptying into a 400 L reservoir. The flume return valve was adjusted to control discharge and create free stream velocities of approximately 0, 2, 3, and 5 cm $s^{-1}$; similar to the range reported in field studies of submerged macrophyte canopies including *E. canadensis* (Losee & Wetzel 1993, Madsen & Warncke 1983; Sand-Jensen & Pedersen 1999). Water from the Upper Mississippi River with no additional nutrients was used. Light was provided by three overhead growth lights, controlled on a 12 hour cycle, with 145 μmol quanta $m^{-2}s^{-1}$ maximum irradiance as measured at the washed sand surface. A constant volume of water was maintained by adding water daily to a prescribed level to avoid concentrating the soluble nickel by evaporative water losses. Prior to the start of the experiment, sand was washed repeatedly until no fines were visually present in the water when sand was agitated. Washed sand was used as a substrate to minimize nickel adsorption to sediment as well as discourage *E. canadensis* root formation and root nickel uptake. Before each experiment, the flume water was replaced twice and the flume walls were cleaned to minimize residual nickel in the system from the previous experiment. All plants were removed after each experiment and replaced with fresh, non-nickel exposed *E. canadensis* grown at the laboratory.

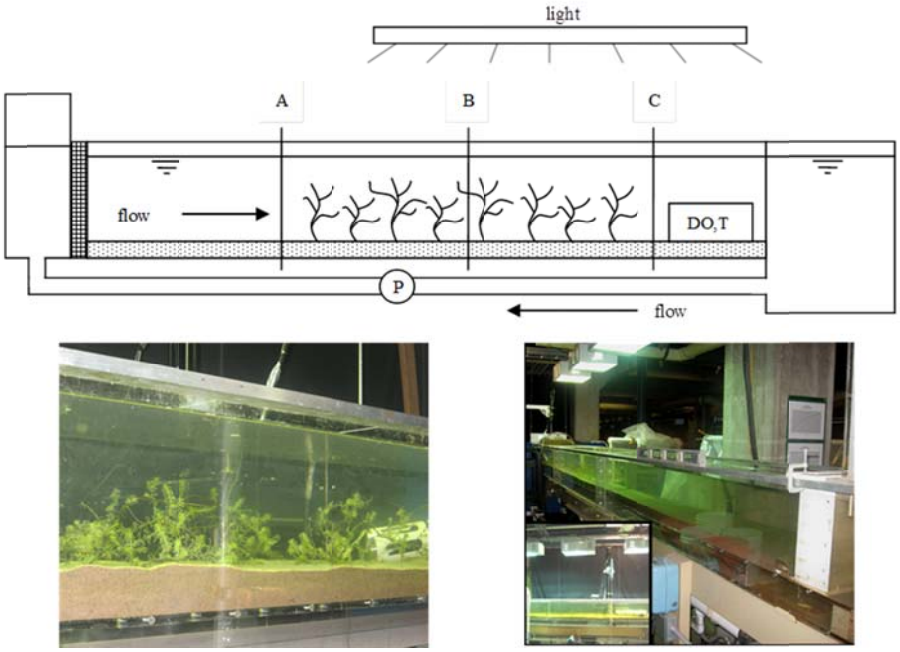


**Fig. 2.1** Schematic and photographs of experimental mesocosm, in a re-circulating flume with channel dimensions; 0.47 m width, 5.2 m length, and 0.2 m water depth. The mesocosm elements included a canopy of live *E. canadensis* and associated epiphytes, three overhead growth lights, Mississippi River water, and washed sand. A, B, and C represent velocity profile locations. Environmental parameters such as dissolved oxygen and temperature were measured continuously by a Sonde, labeled DO, T in the schematic.

Associated epiphytes originated from both the original plant clippings and through colonization by ambient, free-floating algae and bacteria in Mississippi River water. An acclimation period of three to seven days allowed the epiphytic community to establish. Once epiphytic communities appeared to be thriving, diluted nickel in the form of nickel chloride hexahydrate ($NiCl_2(6H_2O)$) at a nominal concentration of 0.5 mg $L^{-1}$, was added to the flume reservoir and allowed to mixed through the system.

### *2.2.3 Measurement procedure*

Velocity fields were quantified before nickel addition for each experiment using an ADV (Sontek YSI Incorporated, San Diego, California, U.S.A.). Flow was seeded with two $\mu$m diameter silica particles to improve the signal-to-noise ratio. Raw data was filtered using WinADV software (U.S.A. Bureau of Reclamation) to remove measurements with correlation scores less than 70 percent, data spikes and signal-to-noise ratios greater than five percent. Velocity measurements were made with an acoustic Doppler velocimeter at 50 Hz sampling frequency for one minute in each sample location (3000 data measurements per location per profile per experiment). Three cross sectional profiles consisting of 50 measurement points were completed for each experiment located in front of the canopy, in the middle of the canopy, and behind the canopy. From the raw data, the time averaged, and span-wise spatially averaged velocity profiles $\langle \overline{U} \rangle$ (m $s^{-1}$), the span-wise spatially averaged root-mean-square velocity, $\langle u_{rms} \rangle$, and the dimensionless ratio of fluctuation level to free stream velocity, commonly referred to as turbulent intensity, Tu (%):

$$Tu\,(\%) = 100\frac{\langle u_{rms} \rangle}{\overline{U}_{\infty}} \quad . \qquad (2.7)$$

were determined where $\overline{U}_{\infty}$ (m $s^{-1}$), is the free stream velocity measured in front of the canopy.

All samples for determination of nickel content were immediately processed after collection from the flume. Sampling intervals ranged from one half hour interval at the

beginning of the experiments when concentration was rapidly increasing to once a day after equilibrium was expected to have been achieved. At each sample time, two plants were harvested. Plants were harvested every other plant from the back of the canopy first to minimize canopy disturbance. Experiments lasted between 48 hours for the highest Reynolds number to six days for the stagnant water experiment.

Immediately after harvest, *E. canadensis*-epiphyte samples were placed in 50 mL of 65 mM phosphate buffer solution rinse (pH 6.8) to maintain osmolarity of the samples and thus prevent nickel leaching via cell lysis during the separation process (Zhang et al., 2003). Epiphytes were separated from plants using gentle mechanical agitation; a method reported to result in 90 % removal efficiency (Zimba and Hopson 1997). The epiphyte slurry rinse was filtered onto a pre-weighed, pre-combusted Whatman GF/F filter (nominal pore size 0.7 μm). Both plant and epiphyte samples were air dried, dried for 2 hrs at 105 ºC, then weighed to determine dry weight DW (g). Plant and epiphyte samples were dry-ashed in a muffle furnace for 2 hrs at 450 $^{o}$C, dissolved in 5 mL of 50% HCl, and diluted to volume with de-ionized water (Azcue & Mudroch 1994, Zheljazkov & McNeil 2008). The flume wall epilithic community was sampled via scraping a known area and prepared for analysis using the same procedure as for plant and epiphyte samples. Water samples were filtered through a Whatman GF/F filter before measuring nickel content. Unfiltered water samples were also collected for nickel concentration analysis to determine the contribution of the plankton community. Nickel content was measured using atomic absorption spectroscopy (Perkin Elmer AAnalyst 100, Waltham, Massachusetts, U.S.A.). $Ni(NO_3)_2$ in 0.1 mol $L^{-1}$ $HNO_3$ was used to determine the

calibration standard curve. Samples were run blind with periodic checks of reagent blanks. All lab ware was acid-washed prior to use. The detection limit of the atomic absorption spectrometer was 0.14 mg $L^{-1}$.

Plant volume was measured before and after each experiment using a water volume displacement method. Plant frontal surface area was determined digitally, using an image analysis program, ImageJ 1.37v (National Institute of Health, USA) on individual plant photographs. For plants, the volume-to-frontal area ratio, $V A_{fr}^{-1}$, was determined by linear regression to be 0.089 cm ($r^2 = 0.65$, n = 40). Linear regression was also used to relate plant volume to dry weight (DW = 0.046V, $r^2 = 0.79$, n = 42). For epiphytes, a five $\mu$m diameter spherical shape was assumed which results in $V A_{fr}^{-1} = 1.7 \times 10^{-4}$ cm. The dry weight to volume ratio for epiphytes was assumed to be the same as for plants.

Temperature, T ($^{o}$C), pH, and dissolved oxygen, DO (mg $L^{-1}$), were monitored using a calibrated Hydrolab DS5 Water Quality Sonde (Hach Corporation, Loveland, Colorado, United States of America (USA)). The molecular diffusion coefficient used for nickel in water, D ($m^2 s^{-1}$), was $1.01 \times 10^{-9}$ $m^2 s^{-1}$ (Sato et al. 1996).

## 2.3 Results

### *2.3.1 Mesocosm conditions*

Mesocosm dissolved oxygen concentration was diurnally periodic, indicating a functioning biotic system, with approximately 0.3 mg $L^{-1}$ amplitude periodicity. The mean pH was 8.8 for all experiments (Table 2.1). Water temperatures averaged 31.6 $^{o}$C for the three experiments with flowing water and 26.7 $^{o}$C for the experiment with

stationary water (Table 2.1). Although the flume was washed and the water was replaced between experiments, there was residual nickel in the mesocosm that altered initial conditions and had to be accounted for in the model (Table 2.2).

| $Re_c$ | $\overline{U}_\infty$ | $\langle u_{rms} \rangle$ | DW *E. canadensis* | Epiphyte biomass | pH | T | $\nu$ x $10^{-6}$ |
|---|---|---|---|---|---|---|---|
| (-) | (cm $s^{-1}$) | (cm $s^{-1}$) | (g) | (g g $DW^{-1}$) | | ($^oC$) | ($m^2$ $s^{-1}$) |
| 0 | 0 | 0 | 0.023 ± 0.015 | 0.690 ± 0.303 | 8.7 | 26.7 ± 0.6 | 0.861 |
| 220 | 1.96 | 0.21 | 0.040 ± 0.014 | 0.185 ± 0.067 | 8.9 | 31.4 ± 0.9 | 0.777 |
| 340 | 3.06 | 0.32 | 0.015 ± 0.007 | 0.473 ± 0.166 | 8.9 | 32.3 ± 0.9 | 0.763 |
| 460 | 5.27 | 0.45 | 0.031 ± 0.014 | 0.183 ± 0.053 | 8.8 | 31.0 ± 0.8 | 0.784 |

**Table 2.1** Experimental conditions within mesocosm. Average values of free stream velocity ( $\overline{U}_\infty$ ), pH, and temperature are provided. Reported epiphyte biomass is averaged across all plants for each experiment. *E. canadensis* DW is the average dry weight of an individual plant for that experiment. The kinematic viscosity of water ($\nu$) was calculated for each experiment based on the average water temperature. All reported errors are one standard deviation.

Individual *E. canadensis* biomass ranged from 15 to 40 mg DW (Table 2.1). The change in plant biomass over the course of the experiment, measured as the difference between initial and final plant displacement volume, showed no trend with exposure time. Neither total biomass nor change in biomass was related to Reynolds number. Epiphyte biomass, defined as the epiphyte community dry weight per plant dry weight, averaged over the duration of an experiment, ranged from 183-690 mg $g^{-1}$ DW. There was no correlation between epiphyte biomass and Reynolds number (Table 2.1). There was no change in epiphyte biomass after nickel addition. Average epiphyte biomass was on the

low side of reported *Elodea* epiphytic field densities which range from 273 mg g AFDW$^{-1}$ (Gross et al. 2003) to 2.81 g (g DW)$^{-1}$ (Pelton et al. 1998).

### *2.3.2 Flow characteristics*

Profiles of span-wise averaged $u_{rms}$ are reported both in front of the canopy and within the canopy, where a peak $u_{rms}$ occurs at the canopy height for $Re_c$ = 340 and 460 (Fig. 2.2). Effective canopy height, $h_c$, was found to be 8 cm for these cases and used as $h_c$ for all experiments. Experimental flow conditions ranged from non-moving water to free stream velocities of 5.3 cm s$^{-1}$ with unsteady flow (Table 2.1). Profile averaged $u_{rms}$ values within the canopy, used to calculate $Re_c$, are reported in Table 2.1. Turbulent intensity collapsed within the canopy but outside of the canopy, retained the open channel flow distribution that was seen in front of the canopy (Fig. 2.3).

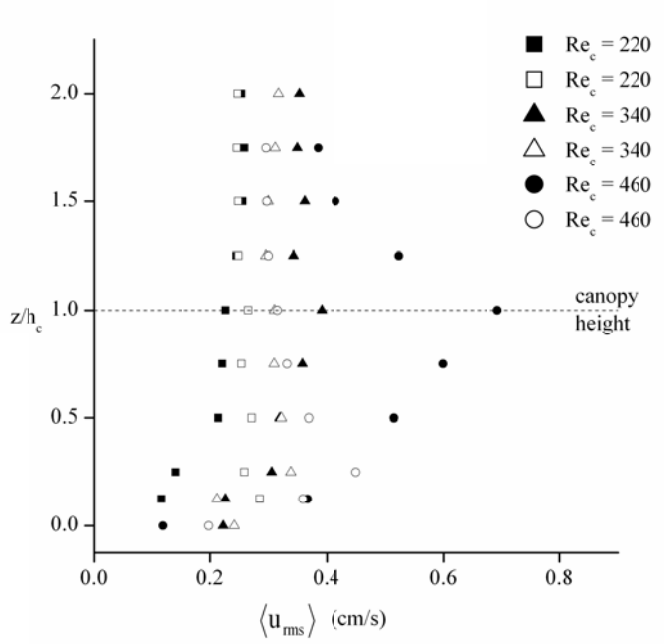


**Fig. 2.2** Span-wise averaged root mean square velocity profiles for all flow conditions. Closed symbols represent measurements within the *E. canadensis* canopy. Open symbols represent measurements in front of the canopy in the open channel. Height is normalized by an effective canopy height of eight centimeters.

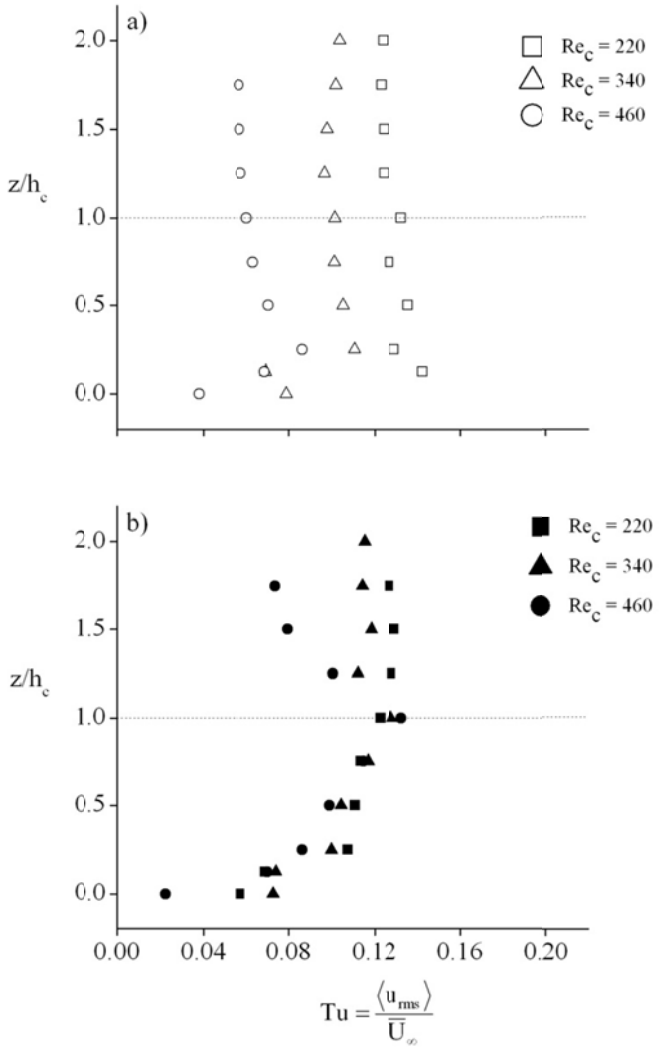


**Fig. 2.3** Turbulent intensities profiles taken a) in the open channel in front of the *E. canadensis* canopy and b) in mid-canopy.

### *2.3.3 Nickel uptake*

For both epiphytes and *E. canadensis*, at all Reynolds numbers, the nickel concentration initially increased rapidly then gradually approached an equilibrium concentration (Fig. 2.4). The mass balance model presented in Eq. 3.2 was applied to the

experimental data set to generate parameters that could be compared with $Re_c$ (Table 2.2). The quantification of nickel content in the washed sand substrate was unsuccessful. Nickel levels in epilithic, planktonic, and episammic biota were negligible.

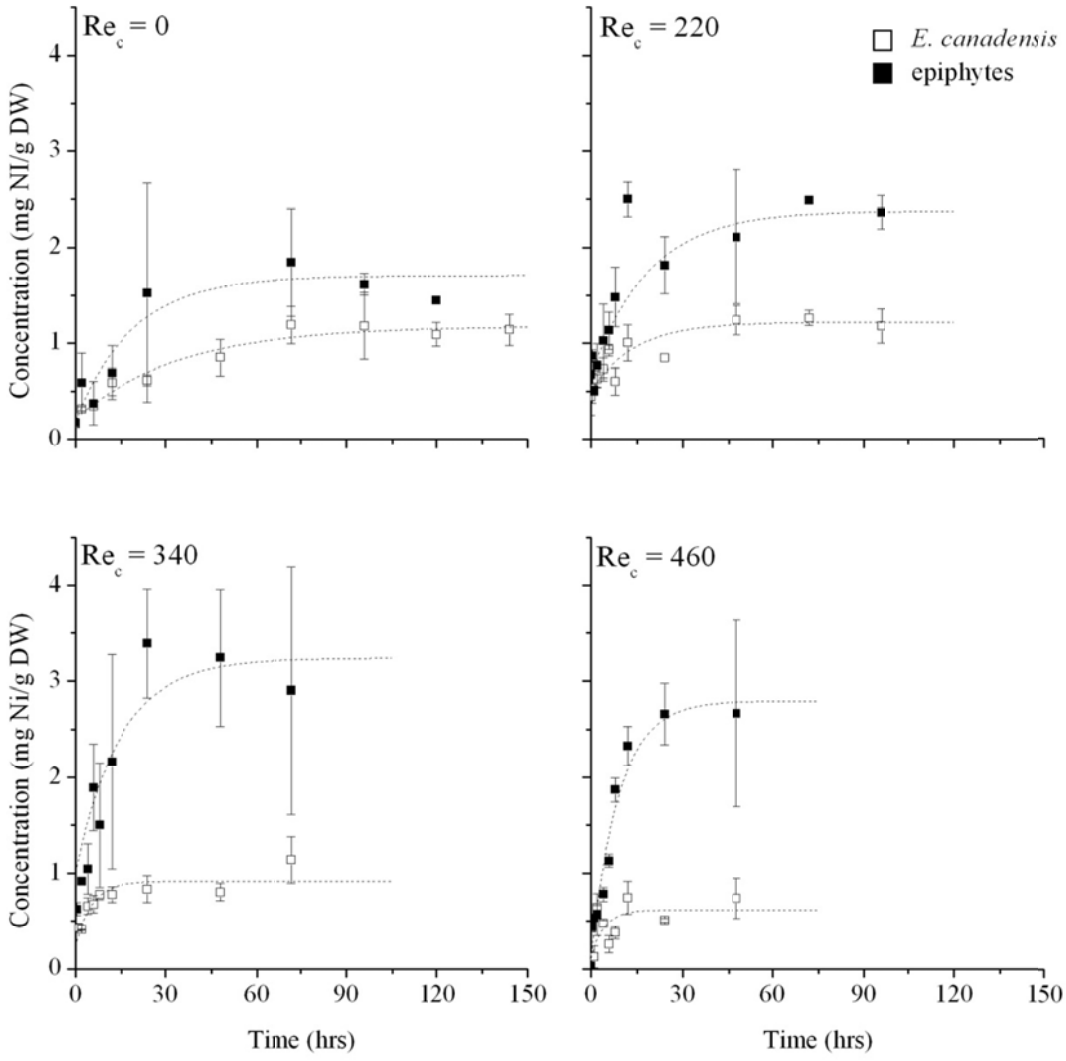


**Fig. 2.4** Experimental measurements of nickel concentration over time (symbols) and nickel flux model (dashed and solid lines). Error bars on data points indicate one standard deviation in measurement value for that sample time. Values for model coefficients and $R^2$ for the non-linear regression of the data to the model are given in Table 2.2.

| | $Re_c$ | $\lambda$ | $C_o$ | $C_{eq}$ | $t_{eq}$ | $R^2$ |
|---|---|---|---|---|---|---|
| | - | ($hr^{-1}$) | (mg Ni g $DW^{-1}$) | (mg Ni g $DW^{-1}$) | (hr) | - |
| *E. canadensis* | 0 | 0.03 | 0.211 | 1.178 | 151.3 | 0.86 |
| *E. canadensis* | 220 | 0.07 | 0.400 | 1.218 | 58.1 | 0.76 |
| *E. canadensis* | 340 | 0.19 | 0.237 | 0.919 | 23.0 | 0.81 |
| *E. canadensis* | 460 | 0.23 | 0.120 | 0.618 | 19.2 | 0.45 |
| Epiphytes | 0 | 0.05 | 0.197 | 1.708 | 85.8 | 0.57 |
| Epiphytes | 220 | 0.05 | 0.665 | 2.380 | 79.6 | 0.86 |
| Epiphytes | 340 | 0.07 | 1.020 | 3.238 | 63.3 | 0.48 |
| Epiphytes | 460 | 0.11 | 0.105 | 2.798 | 41.4 | 0.89 |
| Water | 0 | 0.03 | 0.713* | 0.229* | 182.9 | 0.98 |
| Water | 220 | 0.06 | 0.570* | 0.267* | 75.7 | 0.92 |
| Water | 340 | 0.13 | 0.452* | 0.250* | 34.1 | 0.92 |
| Water | 460 | 0.06 | 0.492* | 0.160* | 87.0 | 0.95 |

* Water nickel concentration in mg Ni $L^{-1}$.

**Table 2.2** Coefficients generated from model of nickel uptake. Coefficients include uptake rate, λ, initial concentration, $C_o$, equilibrium concentration, $C_{eq}$, and time to equilibrium, $t_{eq}$. Values of $R^2$ for each model are also given. $Re_c = \langle u_{rms} \rangle h_c / \nu$.

### *2.3.4 Relating nickel uptake to flow conditions*

For both epiphytes and *E. canadensis*, the uptake rate $\lambda$ increased with Reynolds number with a stronger $Re_c$ response seen in *E. canadensis* (Fig. 2.5a). Equilibrium tissue concentrations were normalized by water equilibrium concentrations to account for possible effects of varying water nickel concentrations. The resulting biological concentration factor, BCF (mg Ni (g DW)$^{-1}$ per (mg Ni $L^{-1}$)), is graphed versus $Re_c$ (Fig. 2.5b). In plants BCF was constant for low Reynolds numbers then decreased with increasing $Re_c$. For epiphytes, BCF increased with increasing Reynolds number. For both macrophytes and epiphytes the time to equilibrium, $t_{eq}$, decreased as $Re_c$ increased

with a stronger response seen in the macrophytes (Fig. 2.5c). For all nonzero $Re_c$, epiphytes take longer to reach equilibrium than plants do.

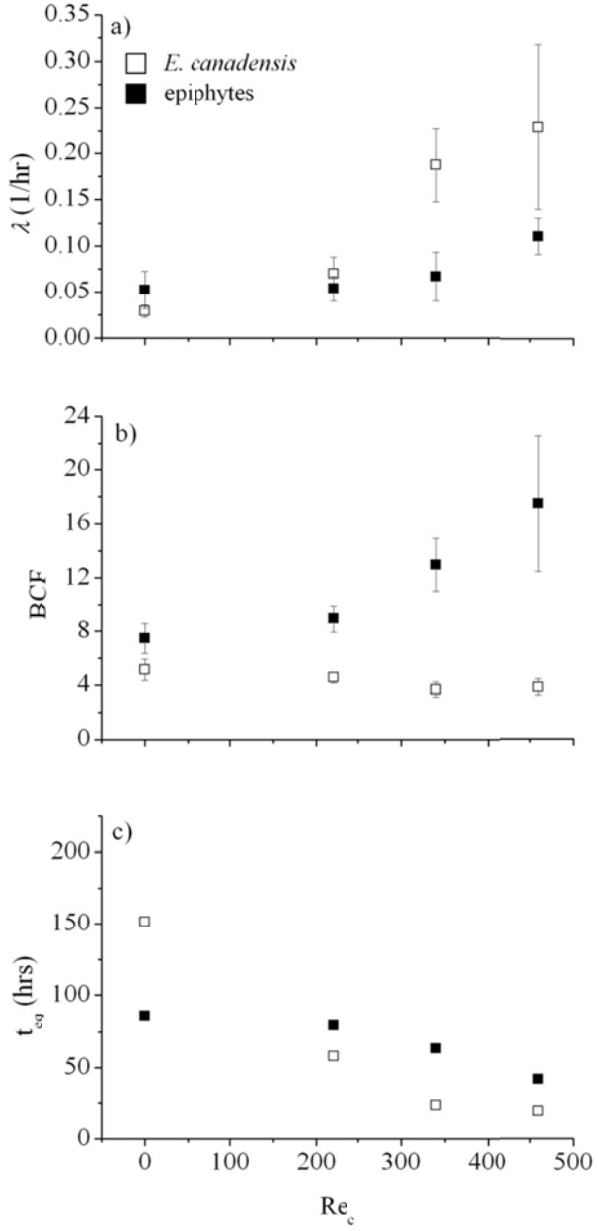


**Fig. 2.5** Relationship between nickel uptake parameters and canopy Reynolds number for epiphytes and *E. canadensis*; a) nickel uptake rate λ, b) equilibrium concentration $C_{eq}$, and c) time to equilibrium $t_{eq}$. Error bars are calculated from confidence interval on the non-linear regression of the model.

The Sherwood number integrates initial and equilibrium parameters described above into one number representing the actual flux as compared to purely diffusional flux. The relationship of Sh to $Re_c$, based on flux calculations from Eq. 2.3 is shown in Fig. 2.6. For both epiphytes and *E. canadensis*, Sh increased with increasing $Re_c$.

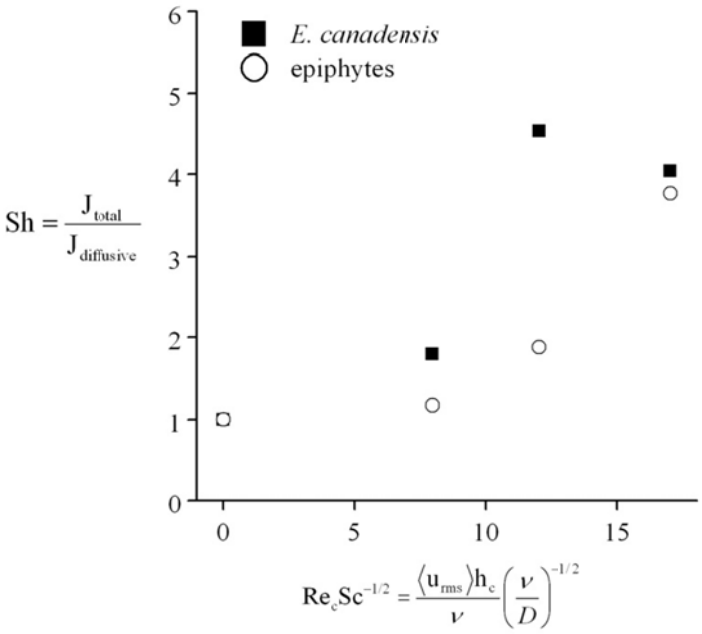


**Fig. 2.6** Sh versus $Re_c Sc^{-1/2}$ for *E. canadensis* and epiphytes.

## 2.4 Discussion

Turbulent intensity (Tu) distributions in front of the canopy agreed with what is expected for open channel flow (Fig. 2.3a) (Laufer 1951). Tu collapsed to one curve within the canopy, which supports the earlier use of $\langle u_{rms} \rangle$ and $h_c$ as the characteristic length and velocity scales, respectively. Within the canopy, Tu increased (as compared

to flow in front of the canopy) for $Re_c = 460$ and decreased for $Re_c = 220$. This suggests that the morphology and geometry of the canopy has a stronger effect on flow conditions within the canopy than the approaching flow. Physically, at low Reynolds numbers with low turbulent kinetic energy, the canopy is dissipating kinetic energy and at higher Reynolds numbers the canopy enhances turbulence by producing canopy scale eddies. Locally, mixing and transport are greatest at the top of the canopy where turbulent intensity and shear stress peak (Wilson & Shaw 1977). This high level of mixing may enhance nickel uptake by rapidly replenishing the source at the edge of the boundary layer or it may degrade nickel uptake through surface scour. Further research examining the variations in spatial distribution of nickel within the canopy, for both epiphytes and macrophytes would strengthen our understanding of the relevant transport mechanisms.

BCF values for *E. canadensis* in stationary water, $Re_c = 0$, are nearly identical to that reported in Maleva et al. (2009). The change in plant biomass over the course of the experiment, measured as the difference between initial and final plant displacement volume, showed no trend with exposure time, either indicating that nickel exposure was sublethal or that plant production response time was longer than the duration of the experiment. In plants, BCF was constant for low Reynolds numbers then decreased with increasing $Re_c$. If uptake was due to a mass transfer process such as adsorption, $C_{eq}$ would be expected to increase as $Re_c$ increases. A BCF that decreases with increasing $Re_c$, indicates that *E. canadensis* is exhibiting a physiological response to increased flow rates. BCF was higher in the epiphytes than in *E. canadensis* for all $Re_c$. For epiphytes, BCF increased with increasing Reynolds number. This indicates either mass transfer

control or dual mass transfer/kinetic control (Sanford & Crawford 2000, Thomas & Atkinson 1997). Epiphytic nickel equilibrium concentrations for all Reynolds numbers were greater than 1000 μg Ni $(g\ DW)^{-1}$; the value used to define a plant as a hyper-accumulator (Brooks et al. 1977). The opposing trends in BCF with increasing $Re_c$ indicate that different mechanisms control nickel uptake between *E. canadensis* and the epiphyte community. It is not possible from this data to separate out how macrophyte-epiphyte interactions, such as epiphytic shielding, altered roughness or excretion, may have altered the relative distribution of nickel. Epiphyte biomass, which would be expected to correlate with interaction effects, did not show a trend with $Re_c$ although BCF did.

For both *E. canadensis* and the epiphyte community, $t_{eq}$ decreased with increasing $Re_c$ and $\lambda$ increased with increasing $Re_c$. This demonstrates how much more efficiently uptake occurs with fluid motion than under only molecular diffusion. For comparison, $\lambda$ for nickel uptake by *E. canadensis* in stationary water based on the data from Kahkonen and Manninen (1998) was calculated by applying a first order model to their data then averaging across their three reported concentrations ($\lambda = 0.045\ hr^{-1}$). For all but one experiment the biota reached equilibrium before the water, indicating that water equilibrium concentrations were not controlling the equilibrium concentration in the biota (Table 2.2).

In the nickel flux model it was assumed that the nickel loading rate was a constant once the nickel had been added to the system. However, dissolved nickel levels in the mesocosm water decreased as a first order process over time (Table 2.2). In evaluating

the validity of the original model assumption it is important to recall that the control volume is around the biota. The central assumption in this model is that the concentration of water in the system greatly exceeded the biota's ability to process it. This assumption would be incorrect if a passive process such as adsorption was the dominant nickel uptake mechanism. Typically, adsorption accounts for a negligible level of heavy metal uptake in macrophytes (Hudson 1998) but may be significant for epiphytes. To examine the potential effect of decreasing water nickel concentration, biotic nickel uptake was modeled using the exponential decay equation to describe the water nickel concentration as the loading rate, W(t). This resulted in a first order, linear, non-homogeneous differential equation with an exact solution. After fitting this equation to the experimental tissue nickel concentration data, equilibrium concentration levels were found to not change from the original model but the tissue uptake rate, $\lambda$, was limited by the decay model to be lower that the water nickel decay rate.

It is possible that the uptake of nickel was influenced by temperature. In the three experiments with moving fluid the pump input heat into the mesocosm resulting in a four degree Celsius difference between the moving water temperatures and the stationary experiment water temperature (Table 2.1). There was no significant difference between water temperatures in the three moving water experiments. Water temperature is indirectly included in the uptake dependency on $Re_c$ seen in Figs. 2.5 and 2.6, through the variation of $\nu$ with water temperature. Fritioff et al. (2005) found that increasing the water temperature from 5 °C to 20 °C resulted in higher nickel concentrations in *E. canadensis* plants at the higher temperature. In contrast, the data presented here does not

reflect a trend in BCF with temperature nor is water temperature correlated with $Re_c$. For *E. canadensis*, the coolest experiment, $Re_c = 0$, had the highest nickel concentration.

The curve reflecting Sh versus $Re_c$ on *E. canadensis* nickel uptake flattens out below $Re_c = 340$, indicating that for $Re_c$ higher than this, fluid flow conditions no longer influenced nickel uptake (Fig. 2.6). The Sh versus $Re_c$ curve for epiphytes does not shown saturation of the effect of fluid flow conditions within the tested range of $Re_c$. It is expected that for some $Re_c$ greater than what was tested, the capacity of the epiphyte community to uptake nickel will be fully utilized and the Sh versus. $Re_c$ graph would also flatten out.

## 2.5 Conclusion

Through laboratory mesocosm experiments with live *E. canadensis* and naturally colonizing epiphytes grown in a re-circulating flume, fluid flow conditions are shown to have a negative effect on *E. canadensis* ability to concentrate nickel, as measured by BCF, and a positive effect on the rate of uptake. In contrast, increasing $Re_c$ resulted in an increased biological nickel concentration factor for the epiphytic community with no saturation of this effect seen within the fluid flow range tested. Although tissue nickel concentrations were much higher in the epiphyte community than in *E. canadensis*, more total nickel was sequestered in *E. canadensis*. This result would be reversed if mesocosm epiphyte densities reflected the higher epiphyte densities previously reported in field studies. This research indicates that fluid flow conditions alter nickel uptake by *E. canadensis* and the epiphytic community and that the two have different preferential flow

regimes. It also suggests the promising bioremediation potential of both in moving fluids in aquatic environments.

# Chapter 3 Photosynthetic oxygen flux by *Macrocystis pyrifera*: A mass transfer model with experimental validation

This chapter elaborates the development of a mass transfer model to determine rates of photosynthetic oxygen flux from the giant kelp, *Macrocystis pyrifera* in a moving fluid. The model can be used to calculate local dissolved oxygen flux, blade averaged oxygen flux and daily average net primary productivity for a kelp forest. Predicted rates of photosynthetic oxygen flux agree well with previously reported direct measurements. This model was derived from the fundamental principles of conservation of mass and momentum over a flat plate using an integral method approach and is applicable in laminar, transitional and turbulent flows. It predicts oxygen flux as an explicit function of fluid flow conditions above the kelp blade. Experimental velocity profiles and dissolved oxygen concentration profiles, measured under a range of fluid flow conditions, followed power-law scaling and demonstrated local similarity between oxygen and velocity distribution within the boundary layers above the kelp blade. The proposed model provides a useful tool for estimating rates of photosynthesis with minimal data collection.

## 3.1 Introduction

*Macrocystis pyrifera*, commonly known as giant kelp, forms large, highly productive forests in temperate coastal waters worldwide (Graham et al. 2007). It typically grows in near shore, subtidal regions that can be either current or wave

dominated (e.g. Gaylord et al. 2004). At reported growth rates of 2 kg dry mass $m^{-2}$ $yr^{-1}$ and a standing biomass of 10 fronds $m^{-2}$ (Reed et al. 2008, Rosman et al. 2007), *M. pyrifera* heavily influences local concentrations of dissolved gases and water velocity, creating an important microhabitat that maintains biodiversity (Dayton 1985, Steneck et al. 2002). Within *M. pyrifera* forests, velocities have been reported to be 25-33% of those measured in adjacent open waters (Fram et al. 2008).

Experimental studies have demonstrated that water motion can modify the rate of photosynthesis and thus primary productivity, by *M. pyrifera* through three distinct processes (Wheeler 1980, Gerard 1982, Hurd et al. 1996). Low nitrate concentrations, such as occur in the summer, coupled with low seawater velocities, have been shown in both field and laboratory investigations to decrease photosynthesis (Jackson 1977, Zimmerman & Kremer 1986, Hepburn & Hurd 2005). Dissolved inorganic carbon (DIC) limitation of photosynthesis can occur at free-stream velocities less than 7 cm $s^{-1}$ with water DIC concentrations under 6 $\mu$mol $L^{-1}$ (Wheeler 1980). DIC limitation is thought to result from either boundary layer resistance or from the buildup of the photosynthetic waste product $OH^-$ in the boundary layer (Maberly 1990, Gonen 1993, Hurd 2000). Recent research suggests that reduced efflux of dissolved oxygen (DO) from the blade surface may increase photorespiration and thus lower photosynthetic rates (Mass et al. 2010).

The influence of water motion on the supply of dissolved nutrients and the removal of metabolic byproducts at the blade surface is referred to as mass transfer (e.g. Hurd 2000). During photosynthesis, local gradients of DIC, dissolved nutrients, and DO

form concentration boundary layers adjacent to the surface of kelp blades due to the difference in the free-stream water concentration and the concentration at the blade surface. Similarly, a velocity gradient is formed by the stress generated by fluid motion near the blade surface (e.g. Kays et al., 2005). When water motion limits mass transport, the supply of DIC and dissolved nutrients to the blade surface is replenished slower than the blade consumes them and photosynthetic rates are limited by mass transfer processes. The occurrence of mass transfer limitation of photosynthesis depends on the relative rates of kelp intracellular metabolic processes to the water side mass transfer processes (Sanford & Crawford 2000). At higher velocities, intracellular processes are often more limiting to photosynthesis than are mass transfer processes (Enriquez & Rodriguez-Roman 2006).

Estimating rates of photosynthesis *in situ* continues to challenge researchers. Common methods include measuring electron transport rates (ETR) or measuring evolution of DO. A direct measurement of photosynthetic rate can be made by placing a tissue segment in an enclosed chamber and recording the change in bulk water DO concentration , which is not practical *in situ* without altering the flow conditions (e.g. Wheeler 1980, Koch 1994). While ETR measurements can be made relatively easily *in situ*, laboratory experiments have demonstrated that they are accurate predictors of photosynthetic flux only under conditions where light is limiting (Longstaff et al. 2002). Alternatively, DO concentration profiles, measured with micro-sensors, have been used with Fick's Law to estimate photosynthetic flux (Sand-Jensen et al. 1985, Miller & Dunton 2007, Nishihara & Ackerman 2007). This method preserves variations along the

blade, but the accuracy is strongly affected by the function used to describe the concentration profile and results vary depending on how the concentration is described mathematically (Hondzo et al. 2005, Nishihara & Ackerman 2006). Additionally, relevant information about the momentum transfer is not explicitly incorporated into the estimation.

Previous efforts to model photosynthetic flux using mass transfer theory have assumed fully turbulent flow conditions and used empirical constants to adjust for disagreements between field measurements and model predictions (e.g. Koch 1994, Falter et al. 2004, Cornelisen & Thomas 2009). Although this may be justified for applications in habitats such as coral reefs, measured velocities in the interior of moderate sized *M. pyrifera* forests have been reported between 0.1 cm $s^{-1}$ to 5 cm $s^{-1}$ (Gaylord et al. 2007, Fram et al. 2008), corresponding to laminar or transitional flow conditions. Laboratory experiments have demonstrated through flow visualization studies that flow unsteadiness around kelp blades starts around 2 cm $s^{-1}$ (Wheeler 1980, Hurd & Stevens 1997). Flow that exhibits unsteadiness but has not developed to full turbulence, which occurs around Reynolds numbers of $10^5$ for flow over a smooth flat plate, is termed transitional and is characterized by intermittent bursts of eddies (e.g. Schlichting 1979). At the velocities experienced inside a kelp bed, the assumption of fully turbulent flow would predict a thinner boundary layer, higher mass flux rate, and earlier saturation of mass transfer controlled flux than what occurs under the more realistic transitional flow.

Fluid motion has been reported to mediate photosynthesis. Fluid flow conditions within a kelp forest span laminar, transitional, and turbulent flow regimes. The objective

of this study was to measure and model the effect of fluid motion on kelp photosynthesis over the velocity range typically reported within kelp forests. The model has been applied to experimentally measured DO and velocity profiles above single blades of *M. pyrifera* to estimate local surface DO flux, blade averaged flux, and entire forest net primary productivity (NPP).

## 3.2 Methods

### *3.2.1 Model derivation*

The proposed model was derived from the laws of conservation of mass and momentum applied to control volumes extending from a kelp blade surface to the edge of the respective boundary layers. It was assumed that the DO concentration at the blade surface, $C_s$ (mg $L^{-1}$), the free stream DO concentration, $C_\infty$ (mg $L^{-1}$), and the free stream velocity, $u_\infty$ (m $s^{-1}$), were constant. It was further assumed the blade was hydrodynamically smooth; requiring that for typical velocities within a kelp bed ($u_\infty < 5$ cm $s^{-1}$) the maximal blade corrugation height is less than 0.25 cm.

Under the above assumptions the integral form of conservation of momentum into and out of a control volume of height $\delta$ (m) and length dx (m) was expressed as:

$$-\tau_s = \frac{d}{dx}\left(\int_0^\delta \rho u^2 dy\right) - u_\infty \frac{d}{dx}\left(\int_0^\delta \rho u dy\right) \qquad (3.1)$$

where x (m) is distance in the stream-wise direction, y (m) is the vertical distance from the blade surface, u (m $s^{-1}$) is the stream-wise velocity, $\tau_s$ (kg $m^{-1}$ $s^{-2}$) is the surface

shear stress, and $\rho$ (kg m$^{-3}$) is the water density (Fig. 3.1). All velocity terms are time-averaged.

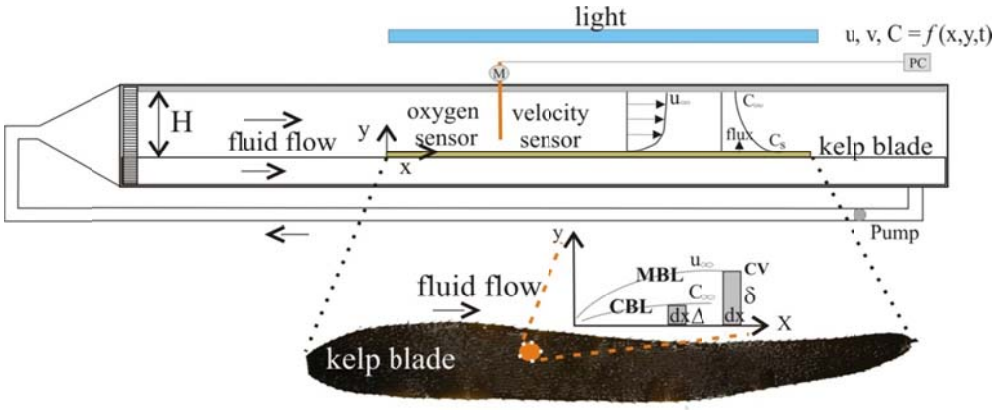


**Fig. 3.1** Schematic representation of mass transfer system above kelp blade within flume setup. Filtered seawater was re-circulated with an adjustable motor driven propeller through the 46 L (test section dimensions of 0.2 m width, 0.15 m height, 0.85 m length) flume. The control volumes used for the derivation of the integral forms of conservation of momentum, length dx and height $\delta$, and for conservation of DO, length dx and height $\Delta$, are shown.

Following a similar approach to that used with conservation of momentum, conservation of DO mass was evaluated using the mass flux into and out of a control volume of height $\Delta$ (m) with width dx (Fig. 3.1). In integral form, conservation of DO mass is:

$$J_s = \frac{d}{dx}\left(\int_0^{\Delta} \rho u\left(C - C_\infty\right)dy\right) \qquad (3.2)$$

where $J_s$ (mg m$^{-2}$ s$^{-1}$) is the DO flux at the kelp blade surface, and C (mg L$^{-1}$) is the DO concentration. All concentrations are time-averaged.

Power functions were used to represent the velocity and DO profiles respectively:

$$\frac{u}{u_\infty} = \left(\frac{y}{\delta}\right)^{1/n} \tag{3.3}$$

$$\frac{C_s - C(y)}{C_s - C_\infty} = \left(\frac{y}{\Delta}\right)^{1/n} \tag{3.4}$$

where n is a constant. The major assumption, resulting in the same exponential dependency on y $\delta^{-1}$ in Eq. 3.3 and y $\Delta^{-1}$ in Eq. 3.4, was that the shape of the dimensionless concentration profile and dimensionless velocity profile were locally similar. The right sides of Eqs. 1 and 2 were integrated using Eqs. 3 and 4. To evaluate $\tau_s$ Eq. 3.3 was written in terms of the commonly used dimensionless variables $u^+$ and $y^+$, where $u^+ = u\, u_*^{-1}$, $y^+ = y u_* \nu^{-1}$, $\nu$ ($m^2\ s^{-1}$) is the kinematic viscosity, and $u_*$ ($m\ s^{-1}$) is the shear velocity. Eq. 3.3 was rearranged to the form:

$$u^+ = a_c\left(y^+\right)^{1/n} \tag{3.5}$$

where $a_c = (u_\infty\, u_*^{-1})(\nu (u_* \delta)^{-1})^{1/n}$ and is typically treated as an empirical constant (Schlichting 1979). Following the procedure developed by Reynolds to evaluate $\tau_s$ in Eq. 3.1, the ratio of $\tau$ at y to $\tau$ at $\delta$ was evaluated then used with the mixing layer analogy for shear stress in a turbulent flow, $\tau / \rho = [\nu + \varepsilon_m]\partial u/\partial y$ to solve for $[\nu + \varepsilon_m]$, where

$\varepsilon_m$ ($m^2\ s^{-1}$) is the eddy diffusivity for momentum (Kays et al. 2005). For a high Schmidt number ($Sc = \nu D^{-1}$) fluid, such as seawater, where D is the molecular diffusion coefficient, the turbulent Schmidt number ($Sc_T = \varepsilon_m D_T^{-1}$), where $D_T$ ($m^2\ s^{-1}$) is the

turbulent mass diffusion coefficient, is approximately one near a surface (Bird et al. 2002, Kays et al. 2005). Using $Sc_T = 1$ with $\nu >> \varepsilon_m$ within the concentration boundary layer, the sum of the D and $D_T$ was expressed in terms of $[\nu + \varepsilon_m]$ as:

$$[D + D_T] \approx Sc^{-1}[\nu + \varepsilon_m] \tag{3.6}$$

This expression was then substituted into Fick's First Law, $J = -[D + D_T]\frac{\partial C}{\partial y}$, and evaluated at the blade surface. The final expression for local surface oxygen flux is:

$$J_s(x) = ASc^{-\left(\frac{n+1}{n+2}\right)} Re_x^{-\left(\frac{2}{n+3}\right)} u_\infty (C_s - C_\infty) \tag{3.7}$$

where A is the dimensionless constant:

$$A = \left( \frac{n}{a_c^n (n+3)(n+2)} \right)^{\left(\frac{2}{n+3}\right)} \tag{3.8}$$

A detailed derivation of the model can be found in the Supplement.

Eq. 3.7 is an analytical solution to the conservations equations (Eq. 3.1 & 3.2) with the velocity and DO profiles approximated by a power function (Eq. 3.3 & 3.4). It contains two model parameters, $a_c$ and n.

To estimate the blade averaged DO flux, $\bar{J}_{s,blade}$ (mol $cm^{-2}$ $hr^{-1}$), Eq. 3.7 can be integrated over the area of the blade using the blade length L (m) and the blade width B(x) (m) where x is the distance from the stipe. The blade averaged DO flux is then defined as:

$$\bar{J}_{s,blade} = \frac{2}{A_s}\int_0^L B(x)J_s(x)dx \qquad (3.9)$$

where $A_s$ ($m^{-2}$) is the total blade area.

### *3.2.2 Flux estimation for no flow condition*

When the water velocity is zero DO is transported through the water by pure diffusion. If the experimental sample time is less than required for the DO gradient to reach equilibrium, concentration variation with time must be included in the governing equation and is given by (e.g. Cussler 1984):

$$\frac{\partial C}{\partial t} = D\frac{\partial^2 C}{\partial y^2} \qquad (3.10)$$

The exact solution to Eq. 3.10, evaluated at the blade surface is:

$$J_s = \sqrt{D/t\pi}(C_s - C_\infty) \qquad (3.11)$$

where t (s) is the elapsed time.

### *3.2.3 Sample collection and preparation*

*M. pyrifera* blades were collected between May and July 2007, near Harrington Point (45º47'03.5" S, 170º43'22.7" E) at the mouth of the Otago Harbour, Dunedin, New Zealand; a site that is sheltered from waves and affected by strong tidal currents (Hepburn & Hurd 2005). Sample blades were selected to be similar distances along the fronds so that the ages of the blades were similar. Blades were cut at the stipe-pneumatocyst junction, placed in an insulated container filled with seawater and transported back to the laboratory, within two hours. At the laboratory, blades were

stored in open, aerated plastic bins containing filtered (Whatman GF/C) seawater in a Conviron Model E15 temperature controlled room kept at 12 ºC with a 12:12 light-dark cycle. An underwater Pulse Amplitude Modulated Chlorophyll fluorometer (Diving PAM, Heinz Walz GmbH), with 650 nm maximum emission wavelength and default internal gain and intensity settings, was used to select experimental blades based on measured fluorescent yield ($F_v$:$F_m$) (Maxwell & Johnson 2000).

### *3.2.4 Laboratory experiments*

Experiments were conducted in a 46 L flume, described fully in Hurd et al. (1994) (Fig. 3.1). Briefly, filtered seawater was re-circulated through a flume consisting of a small motor driven propeller, entrance diffusers, and a test section of dimensions 0.2 m width, 0.15 m height, 0.85 m length. A photon flux density of 130 $\mu$mol photons $m^{-2}$ $s^{-1}$ at the blades surface, chosen to facilitate comparison with Wheeler (1980), was provided by an overhead SONT-ARGO 400 light. Water temperature was monitored but not controlled. The physical water property $\nu$ was calculated based on salinity of 35 g $L^{-1}$ and the average temperature for each experiment (Table 3.2). The value used for the molecular diffusion coefficient D was 1.7 x $10^{-5}$ $cm^2$ $s^{-1}$ (Wheeler 1980). For each replicate, an individual kelp blade was attached to a flat plate and placed in the flume after removing the pneumatocyst.

| Blade ID | $Re_x$ | $C_s$ | $C_\infty$ | $\Delta$ | T | $\bar{J}_{s,blade}$ ($\mu$mol |
|---|---|---|---|---|---|---|
| - | - | (mg $L^{-1}$) | (mg $L^{-1}$) | (cm) | (ºC) | $cm^{-2}$ $hr^{-1}$) |
| 1 | 0 | 21.98 | 9.99 | N/A | 12.2 | 0.08 |
| 1 | 5000 | 23.33 | 9.64 | 0.085 | 11.3 | 0.15 |
| 1 | 8500 | 20.39 | 9.95 | 0.160 | 11.4 | 0.20 |
| 1 | 18200 | 18.46 | 9.78 | 0.052 | 11.3 | 0.25 |
| 4 | 0 | 44.79 | 10.71 | N/A | 11.6 | 0.38 |
| 4 | 5000 | 40.81 | 10.50 | 0.091 | 11.7 | 0.33 |
| 4 | 8500 | 31.57 | 10.37 | 0.075 | 11.8 | 0.40 |
| 4 | 18200 | 27.90 | 10.48 | 0.081 | 12.1 | 0.51 |
| 6 | 0 | 41.52 | 10.36 | N/A | 17.0 | 0.47 |
| 6 | 5000 | 49.19 | 9.90 | .032 | 16.7 | 0.43 |
| 6 | 8500 | 45.48 | 9.97 | .033 | 16.6 | 0.68 |
| 6 | 18200 | 22.77 | 10.03 | .028 | 16.5 | 0.37 |
| 7 | 0 | 31.29 | 9.93 | N/A | 16.1 | 0.15 |
| 7 | 5000 | 29.32 | 9.55 | 0.033 | 15.7 | 0.22 |
| 7 | 8500 | 31.57 | 9.60 | 0.020 | 15.5 | 0.42 |
| 7 | 18200 | 30.27 | 9.57 | 0.018 | 15.5 | 0.60 |
| 8 | 0 | 37.82 | 10.74 | N/A | 12.5 | 0.24 |
| 8 | 5000 | 29.28 | 9.56 | 0.038 | 12.5 | 0.21 |
| 8 | 8500 | 32.52 | 9.62 | 0.051 | 12.7 | 0.44 |

**Table 3.1** Experimental DO concentration data used in flux model for five replicate blades. Surface DO concentration, $C_s$, was measured at the *M. pyrifera* blade surface. Free-stream concentration, $C_\infty$, is the average concentration in the free-stream water above the boundary layer. The concentration boundary layer thickness, $\Delta$, was determined as $C(\Delta)=1.01C_\infty$ after fitting the entire DO concentration profile to a hyperbolic tangent. It is not used explicitly in the flux model.

Velocity was measured with an acoustic-Doppler velocimeter, ($\mu$ADV; Sontek YSI Incorporated) at 50 Hz sampling frequency, for one minute per sample location. Velocity measurements were made every 0.2 cm within 3 cm of the blade and then every 1 cm. Vertical $\mu$ADV position was adjusted manually with 0.1 cm accuracy. Velocity profiles were located at the blade centerline, at a distance of 10 cm from the front of the blade, extending from the blade surface. Shear velocity, $u_*$ (m $s^{-1}$), used in the determination of $a_c$ from experimental data, was estimated three ways: 1. from the slope of the time averaged velocity data in the log-law in the region, using the Law of the Wall, $u^+ = \frac{1}{\kappa}\ln y^+ + B$, where $\kappa$ is the von Karman's constant 0.41 and B is a constant; 2. with the 2-D momentum equation for turbulent flow with boundary layer approximations, $\frac{\tau}{\rho} = -\overline{u'v'} + \nu\frac{du}{dy} = u_*^2(1 - y/H)$, where $\overline{u'v'}$ ($m^2$ $s^{-2}$) is the Reynolds stress and H (m) is the height of the channel (e.g. Nezu & Rodi 1986); and 3. from the definition of shear velocity $u_* \equiv \sqrt{\nu\left.\frac{du}{dy}\right|_{y=0}}$.

DO concentration was measured using an optical oxygen micro-sensor (Microx TX2-A) with a maximum tip diameter of 50 $\mu$m (PreSens Precision Sensing GmBH). DO measurements were made every 0.05 mm near the blade surface then every 0.25 mm. Vertical sensor position was controlled using two mechanical stages with positional accuracy of 0.001 mm for measurements within five mm of the blade surface and 0.1 mm

for measurements further from the blade. The location of the blade surface was determined by lowering the oxygen probe, using the precision stage, until contact of the probe with the blade was confirmed visually. Then, to assure that the probe was not pushing into the blade tissue, the probe was retracted, again with the precision stage, until the DO concentration reading dropped. This was repeated until the location of the kelp surface was determined. Percent oxygen saturation was measured for 1 minute per sample location at 1 Hz sampling rate with temperature compensation enabled. Atmospheric pressure, used to convert DO measurements from percent saturation to mg $L^{-1}$, was taken from www.metservice.co.nz as measured at the Dunedin airport 20 km away at three hour intervals. Sensors were calibrated each day before measurements using a sodium sulfite solution ($Na_2SO_3$) and water saturated air. DO concentration profiles were taken for each of the 5 replicate blades at average free-stream velocities of 0.0, 2.7, 4.6, and 9.8 cm $s^{-1}$. To minimize the effect of the 1 mm tall kelp surface corrugations, measurements were always taken above the apex of a ridge (Hurd & Pilditch 2011).

## 3.3 Results

### *3.3.1 Flow conditions*

Experimental flow data were utilized to determine shear velocity and power functions for the mean velocity profiles. The time-averaged experimental dimensionless velocity data were fit to Eq. 3.3 to determine n and $\delta$ (Fig. 3.2). The experimental free-stream velocity, $u_\infty$, ranged from 2.71 cm $s^{-1}$ to 9.83 cm $s^{-1}$ (Table 3.1). For all velocities,

power function approximations agreed well with the experimental data ($R^2 \geq 0.96$; Table 3.1).

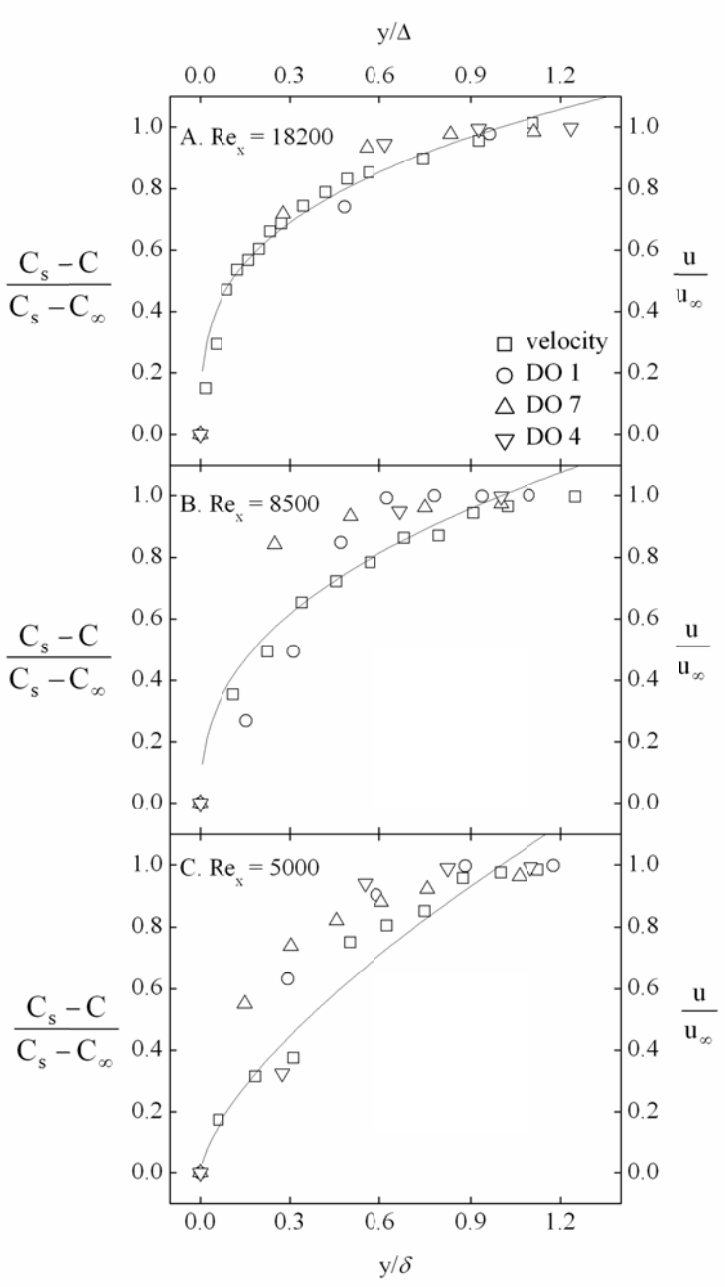


**Fig. 3.2.** Comparison between experimental velocity and concentration profile data and power functions used in model. The three panels represent all data for a given Reynolds number; (A) shows $Re_x$ = 5000,

(B) shows $Re_x$ = 8500, and (C) shows $Re_x$ = 18200. The distance from the blade, y, is made non-dimensional with the boundary layer thicknesses, $\delta$ for velocity profiles and $\Delta$ for concentration profiles. Velocity, u, is normalized with the free-stream velocity, $u_\infty$. DO concentration, C, is made dimensionless using the surface concentration, $C_s$ and the free-stream concentration, $C_\infty$. All variables are time-averaged.

Shear velocity estimates using the log-law method and the Reynolds stresses method agreed within 3% for both $Re_x$ = 8500 and $Re_x$ = 18200. An average of these two results was used for the model (Table 3.1). Insufficient resolution in the velocity profile near the blade surface prevented estimating $u_*$ using the gradient near the blade surface for $Re_x$ = 8500 and $Re_x$ = 18200. Velocity profile data for $Re_x$ = 5000 did not have resolvable Reynolds stresses or a clear log-law region but did have sufficient resolution near the blade that the velocity gradient could be used to estimate $u_*$ (Table 3.1). $U_*$ calculations from experimental data agreed with model estimated values within 12 %. $U_*$, $u_\infty$ , $\delta$, and n were used to calculate $a_c$ from experimental data using Eq. 3.5.

| $Re_x$ | $u_\infty$ | $u_*$ | $\delta$ | n | $R^2$ | $m$ |
|---|---|---|---|---|---|---|
| - | (cm $s^{-1}$) | (cm $s^{-1}$) | (cm) | - | - | - |
| 5000 | 2.71 | 0.16 | 1.6 | 1.49 | 0.96 | 8 |
| 8500 | 4.59 | 0.30 | 2.45 | 2.48 | 0.97 | 10 |
| 18200 | 9.83 | 0.87 | 5.5 | 3.23 | 0.96 | 14 |

**Table 3.2** Flow characteristics based on experimental velocity profiles above *M. pyrifera* blades. Free-stream velocity, $u_\infty$, is the average velocity above the momentum boundary layer. Shear velocity, $u_*$, was

calculated using the slope of the Log-Law and the Reynolds stresses for $Re_x$ = 8500 and 18200 then averaged. The definition of shear velocity was used to calculate shear velocity for $Re_x$ = 5000. The momentum boundary layer thickness, $\delta$, and the exponent n for the power function to the data are reported with the $R^2$ for the nonlinear regression where *m* is the number of data points in the regression.

Model parameters, n and $a_c$, were graphed against $Re_x$ (Fig. 3.3). Previously reported values for $10^5 < Re_x < 2.5\ 10^6$ (Burmeister, 1993) were included in the graph along with the exact Blasius solution for a laminar flow where n = 1, $a_c$ = 0.59, and $Re_x$ = 1850. All graphed points for $Re_x > 10^3$ were used to generate the functional relationships to be used for model parameter determination. The resulting equations are: $n = 1.29\ln(Re_x) - 9.08$; ($R^2$ = 0.97) and $a_c = 1.54\ln(Re_x) - 11$ ($R^2$ = 0.90). For $Re_x$ less than 2000, the parameters were fixed to n = 1, $a_c$ = 0.59.

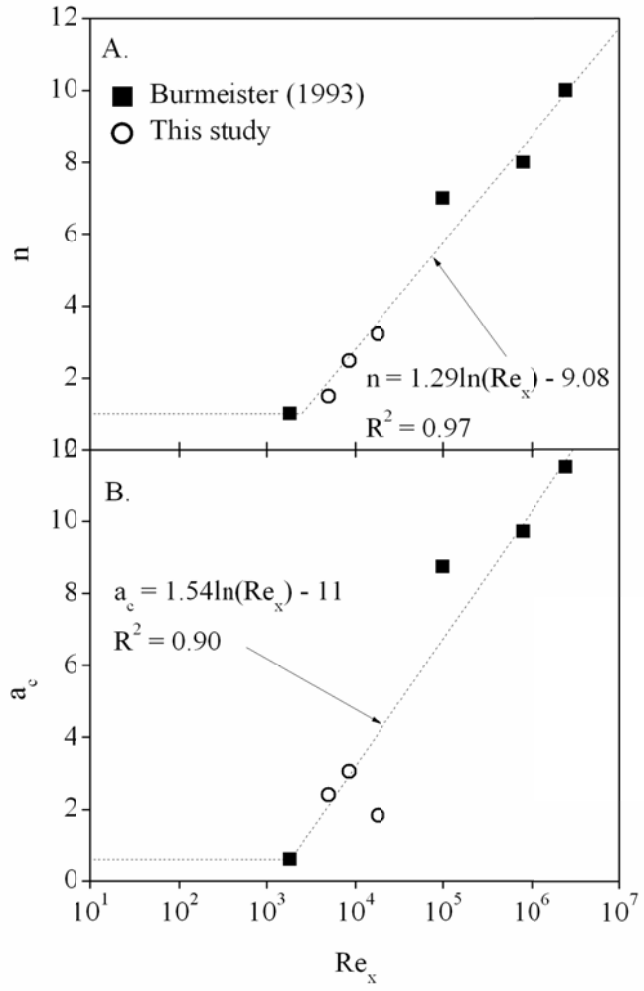


**Fig. 3.3** Relationship between local Reynolds number, $Re_x$ and the parameters $a_c$ and n used in the model. Symbols represent calculated values from experimental measurements in this study (open circles) and reported values (closed squares, Burmeister 1993). The dashed line is the best fit regression to these points.

### *3.3.2 Dissolved oxygen*

Well resolved DO profiles were attained for 3 of the 5 replicate blades. The boundary layers of the other 2 blades fell below the second measurement point and could not be modeled. DO concentration boundary layers were typically on the order of 1 mm thickness. Due to lack of experimental data in the concentration boundary layers at

higher velocities, the concentration boundary layer thickness, $\Delta$ (m) could not be determined from Eq. 3.4, as was done with the velocity data and Eq. 3.3. Instead, the experimental concentration profiles were fit with a hyperbolic tangent function and $\Delta$ was determined as the distance where $C(\Delta) = 1.01C_{\infty}$, a method that compared favorably to integrated DO flux measurements (Nishihara & Ackerman 2007). Experimental measurements of $C_s$, $C_{\infty}$, and $\Delta$ are reported (Table 3.2). Experimental profiles are shown with modeled functions (Fig. 3.2). The collapse of the experimentally measured velocity and DO concentration data onto one curve (Fig. 3.2) validates the model assumption of similarity between these boundary layers. Although boundary layer DO profiles were not always well resolved, $C_s$ was successfully measured for all 5 blades. For 4 of the 5 replicate blades, $C_s$ decreased with increasing $Re_x$ (Fig. 3.4).

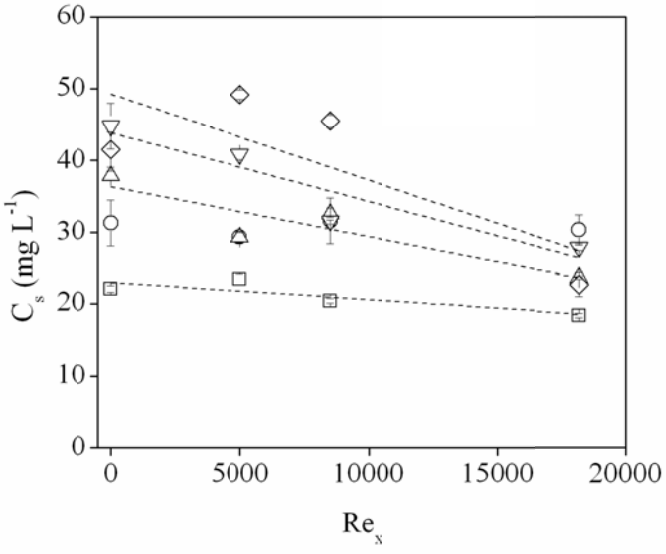


**Fig. 3.4** Measured DO concentration, $C_s$, on the surface of all kelp blades. 4 of the 5 replicates show a trend of $C_s$ decreasing with $Re_x$. Error bars represent one standard deviation (SD) in the 60 measurements that were made for each data point.

### *3.3.3 Local surface oxygen flux*

The model was applied to each blade for non-zero velocities using the parameters n and $a_c$ generated from the velocity profiles and the measured values of $u_\infty$, $C_s$ and $C_\infty$ for individual blades. Water temperature varied by less than 0.6 ºC across experiments for an individual blade (Table 3.2). $\Delta$ was not a variable in the final expression for $J_s(x)$ (Eq. 3.7) and was not used in calculations. Surface flux in the absence of advection ($u_\infty$ = 0) was calculated using Eq. 3.11. Predicted local DO flux from the kelp blades (5 replicates) ranged from 0.27 ± 0.16 $\mu$mol $O_2$ $cm^{-2}$ $hr^{-1}$ for $Re_x$ = 0 to 0.80 ± 0.25 $\mu$mol $O_2$ $cm^{-2}$ $hr^{-1}$ for $Re_x$ = 18200. $J_s(x)$ increased with $Re_x$ (Fig. 3.5). A one-way ANOVA was conducted to compare the effect of $Re_x$ on $J_s(x)$. There was a significant effect of $Re_x$ on $J_s(x)$ for the 4 $Re_x$ conditions [$F(3,16) = 10.08$, $p = 0.001$]. Post-hoc Tukey's HSD tests indicated that $J_s(x)$ for $Re_x$ = 18150 was significantly higher than the other three $Re_x$ conditions at P = 0.05 ($q_{critical} = 4.05$). All other comparisons were not significant.

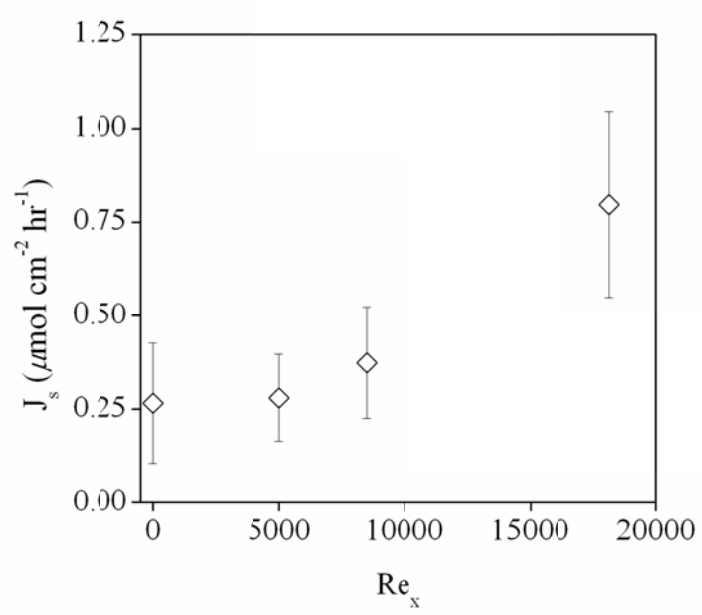


**Fig. 3.5** Variation of local surface DO flux from blade, $J_s$ with $Re_x$. Error bars represent one SD; five replicates.

### *3.3.4 Blade averaged surface oxygen flux*

Eq. 3.9 was integrated numerically using a step size of 0.25 cm to determine the relationship of mass transfer velocity, k (cm $s^{-1}$) to $u_\infty$ where $\bar{J}_{s,blade} = kA_s^{-1}(C_s\text{-}C_\infty)$ (Fig. 3.6). Implicit in this graph is the assumption that salinity = 35 g $L^{-1}$ and the mathematical description of blade morphology $B(x) = \sqrt{x} - 0.1x$ for a blade of length L = 100 cm. B(x) was approximated by applying a nonlinear curve fit to the edge of a blade from photographs of the experimental blades. $\bar{J}_{s,blade}$ was determined for each tested blade (Table 3.2) and was 60% higher, on average, at velocities that saturated mass transfer limitation of photosynthesis than it was in stagnant water (Table 3.1).

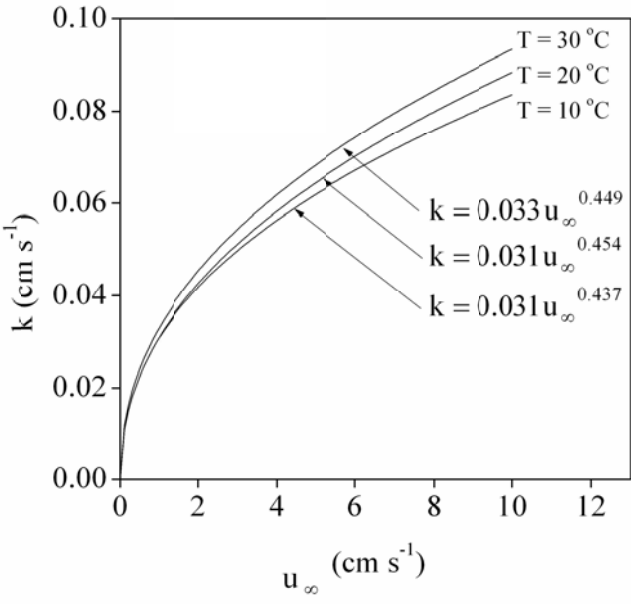


**Fig. 3.6** Relationship between mass transfer velocity k and $u_\infty$ based on numerical solution to Eq. 3.9 and assumptions for blade morphology, B(x) and L.

### *3.3.5 NPP estimate for entire kelp forest*

To illustrate the simplicity and validity of the derived model, the forest averaged daily NPP for the Mohawk Reef forest off the coast of Santa Barbara, CA U.S.A was determined using reported data from November 2006 (Stewart et al. 2009, Reed et al. 2008). November data was chosen to match environmental conditions that affect $C_s$, such as light availability and water temperature. The depth-averaged velocity measured in November 2006 within the Mohawk Reef kelp bed was 2.5 cm $s^{-1}$ (Stewart et al. 2009). Using Fig. 3.6 this corresponds to a mass transfer velocity, k, of 0.035 cm $s^{-1}$. The Mohawk Reef data set does not include measurements of $C_s$ or $C_\infty$, however, the reported November 2006 free stream velocity of 2.5 cm $s^{-1}$ is fairly close to one of the velocities at

which $C_s$ and $C_\infty$ were measured in this experiment (tested $u_\infty = 2.7$ cm $s^{-1}$) so the average value of $C_s$-$C_\infty$ was determined from our data set to use for this estimation. This was 25 mg $L^{-1}$(Table 3.2, $Re_x = 5000$). Assuming our blade morphology is typical for this location, blade area is 332 $cm^2$. A photosynthetic quotient of 1 (Arnold & Manley 1985) was used to convert blade averaged DO flux into blade averaged carbon dioxide ($CO_2$) flux. From the $CO_2$ flux, the molar carbon flux could be determined and converted into grams of carbon per blade surface area per time (g C $m^{-2}$ $day^{-1}$). This was converted to forest averaged daily NPP using the reported blade density for November 2006 of 2 $m^2$ blade area $m^{-2}$ sea surface area (Stewart et al. 2009). The resulting estimate of forest average daily NPP for November 2006 was 2.2 g C $m^{-2}$ $day^{-1}$; the same as determined by Reed et al. (2008).

## 3.4 Discussion

The proposed model can be used to predict local surface oxygen flux, $J_s(x)$, blade averaged surface oxygen flux, $\bar{J}_{s,blade}$, or forest averaged daily NPP. $U_\infty$ and $C_\infty$ are readily measured in the field or in a laboratory and $C_s$ is easily measured in a laboratory. For field experiments, $C_s$ can be measured using either traditional oxygen microprobes with a custom length cable or a self-contained oxygen optode probe positioned by a diver on the surface of the blade. An alternative option is to use $C_s$ measurements made in the laboratory to approximate *in situ* conditions although, as Fig. 3.4 illustrates, flow can have as much influence on $C_s$ as does overall blade physiology and must be carefully replicated. The proposed model does not assume mass transfer limitation but indirectly reflects other factors affecting photosynthesis, such as; photon flux density (PFD), photo-

adaptation, blade age and blade health, in the measurement of $C_s$. For 4 of the 5 blades tested, $C_s$ decreased as $Re_x$ increased (Fig. 3.4), indicating some degree of mass transfer limitation. As velocities increase, transport of dissolved nutrients and waste products is more efficient, resulting in a lower $C_s$. No functional dependency on $Re_x$ was measured for blade # 7 indicating that intracellular processes in the blade were limiting the rate of photosynthesis. For detailed laboratory studies examining local photosynthetic oxygen flux rates along individual blades, Eq. 3.7 can be directly applied with parametric determination from Fig. 3.3. There are no known measurements of local surface oxygen flux, so it was not possible to compare $J_s(x)$ results to the literature.

To determine $\bar{J}_{s,blade}$ or estimate entire forest NPP from *in situ* measurements of $u_\infty$, $C_\infty$, $C_s$ Eq. 3.7 can be integrated as shown in Eq. 3.9 or, if our assumed blade morphology is appropriate, Fig. 3.6 can be used to determine k and then $\bar{J}_{s,blade} = kA_s^{-1}(C_s - C_\infty)$. Since both n and $a_c$ are dependent on x, evaluating Eq. 3.9 analytically is difficult and numerical integration is recommended. $\bar{J}_{s,blade}$ was found to range from 0.27 $\mu$mol $O_2$ $cm^{-2}$ $hr^{-1}$ for $Re_x$ = 5000, to 0.43 $\mu$mol $O_2$ $cm^{-2}$ $hr^{-1}$ for $Re_x$ = 18200. Previously reported $\bar{J}_{s,blade}$ for *M. pyrifera* under similar light and velocity conditions range from 0.3 to 2 $\mu$mol $O_2$ $cm^{-2}$ $hr^{-1}$ (Wheeler 1980, Gerard 1986, Colombo-Pallota et al. 2006). Our blade-averaged fluxes agreed well with reported values at low $u_\infty$ but were lower than has been previous reported at high $u_\infty$. Although the PFD of 130 µmol $m^{-2}$ $s^{-1}$ in our experiment was chosen to match Wheeler (1980), our water temperature was lower and may have slowed physiological processes in comparison to other laboratory studies. The

free-stream velocity that saturates photosynthesis is dependent on conditions such as light level, free-stream nutrient or carbon supply and blade age or health and has been reported between 2 to 8 cm $s^{-1}$(Wheeler 1980, Gerard 1982, Hurd et al. 1996). The proposed model coupled with our experimental data showed an average saturation velocity between 2 to 4 cm $s^{-1}$ (Table 3.2).

The kelp forest averaged NPP estimates from the application of our model agree with the NPP estimates generated by Reed et al. 2008 despite the numerous assumptions made in the application of our model. Although data from the Mohawk Reef in November was chosen to justify using our experimental results for $C_s$, PFD within the forest was not matched. PFD has been measured as high as 1200 $\mu$mol photons $m^{-2}$ $s^{-1}$ on the water surface (Edwards & Kim 2009), but shown to decay to 10% of the surface value by a depth of 1 m (Stewart et al. 2009). The depth-averaged PFD in a 30 m water column was calculated to be approximately 45 $\mu$mol photons $m^{-2}$ $s^{-1}$. However, the biomass is typically greater near the surface so the depth-averaged irradiance experienced by the kelp should be weighted by vertical biomass distribution and 130 $\mu$mol photons $m^{-2}$ $s^{-1}$ may be more reasonable than it initially seems. Direct measurements of $C_s$ at various depths could be used to assess this as well as providing additional spatial resolution to the model. Variability of velocity with respect to position within the forest is available for Mohawk Reef (Gaylord et al. 2007) and could also be included to improve the model.

The appropriate time scale for estimating NPP with this model presented is on the order of a day. The Mohawk Reef kelp forest is reported to turn over 7 times per year (Reed et al. 2008) therefore it is not reasonable to use this model to estimate annual NPP

since it does not take into account the effects of growth rate, recruitment or disturbance history on NPP. It is equally inappropriate to use this model to estimate NPP for time scales of less than a day, since on a shorter time scale, velocity fluctuations due to tides or internal waves can be significant and are not captured in the presented model. On a shorter time scale, the effective $u_\infty$ in a wave dominated environment may be higher than the measured $u_\infty$ due to relative motion between the blade and the water (Denny & Roberson 2002, Stevens et al. 2003, Hepburn et al. 2007) and mass transfer limitation of photosynthesis would be saturated at lower velocities than the proposed model predicts.

The proposed model can be used to estimate local, blade-averaged or forest scale NPP in laminar, transitional and turbulent flows. Developed from the classic engineering integral method, it provides a simple equation requiring minimal measurements and parameter determination. Being equally applicable in transitional flow regimes as in fully turbulent flow, the model accommodates the transitional flow characteristics that have been shown to be prevalent within kelp forests, yet are poorly matched by assumptions based on fully developed turbulent flow. To our knowledge, our model is the first that is applicable to all flow regimes, making it especially useful for the conditions commonly encountered within aquatic canopies such as kelp forests.

## 3.5 Supplement: Detailed model derivation

*Model derivation*- Assuming a unidirectional flow and that the kelp blade behaves as a flat smooth plate, conservation of momentum in integral form is:

$$-\tau_s = \frac{d}{dx}\left(\int_0^{\delta} \rho u^2 dy\right) - u_\infty \frac{d}{dx}\left(\int_0^{\delta} \rho u dy\right) \tag{3.1}$$

In integral form the conservation of DO mass is:

$$J_s = \frac{d}{dx}\left(\int_0^{\Delta} \rho u(C - C_\infty) dy\right) \tag{3.2}$$

The velocity profile in the momentum boundary layer was modeled with a power function:

$$\frac{u}{u_\infty} = \left(\frac{y}{\delta}\right)^{1/n} \tag{3.3}$$

where n is a constant. The dimensionless concentration profile can also be modeled with a power function:

$$\frac{C_s - C(y)}{C_s - C_\infty} = \left(\frac{y}{\Delta}\right)^{1/n} \tag{3.4}$$

The momentum equation was evaluated to determine $\delta$ as a function of x and the relationship of $\tau_s$ to $Re_x$, where $Re_x = u_\infty x/\nu$. The right side of Eq. 3.1 was integrated from zero to $\delta$ after substitution of the power function (Eq. 3.3). This results in the expression:

$$\frac{\tau_s}{\rho u_\infty^2} = \left( \frac{n}{n+1} - \frac{n}{n+2} \right) \frac{d\delta}{dx} \qquad \text{(A1)}$$

To evaluate $\tau_s$, Eq. 3.3 was written in terms of the commonly used dimensionless variables $u^+$ and $y^+$, where $u^+ = u\, u_*^{-1}$, $y^+ = y u_* \nu^{-1}$, and rearranged it to the form:

$$u^+ = a_c \left( y^+ \right)^{1/n} \qquad (3.5)$$

where $a_c = (u_\infty u_*^{-1})(\nu (u_* \delta)^{-1})^{1/n}$ and is typically treated as an empirical constant (Schlichting 1979). Substituting $u_* = \sqrt{\tau_s / \rho}$ into Eq. 3.5 and evaluating it at $\delta$, $\tau_s$ was determined as a function of $\delta$:

$$\frac{\tau_s}{\rho u_\infty^2} = a_c^{\left(\frac{-2n}{n+1}\right)} \left( \frac{u_\infty \delta}{\nu} \right)^{\left(\frac{-2}{n+1}\right)} \qquad \text{(A3.2)}$$

Substituting the expression for surface shear stress provided in Eq. A3.2 into Eq. A3.1, separating terms and integrating, the relationship between $\delta$ and x was determined to be:

$$\delta(x) = \frac{(n+2)(n+3)}{n} A\, Re_x^{-\left(\frac{2}{n+3}\right)} x \qquad \text{(A3.3)}$$

where A is the constant given in Eq. 3.8. Substituting Eq. A3.3 into Eq. A3.1 provides a dimensionless expression relating the local coefficient of friction, $c_f$, to $Re_x$:

$$\frac{c_f}{2} = \frac{\tau_s}{\rho u_\infty^2} = A\, Re_x^{-\left(\frac{2}{n+3}\right)} \qquad \text{(A3.4)}$$

To evaluate the conservation of mass given in Eq. 3.2, we substituted the velocity and concentration profiles (Eqs. 3.3 and 3.4), integrated and obtained:

$$\frac{J_s}{u_\infty (C_s - C_\infty)} = \frac{d}{dx}\left( \Delta \left( \frac{\Delta}{\delta} \right)^{\frac{1}{n}} \right) \tag{A3.5}$$

To determine $J_s$, the procedure developed by Reynolds (Kays et al. 2005) was followed. Briefly, the integral form of the momentum equation is developed for a control volume extending from an arbitrary distance at or above the blade surface, y, to the outer limit of the boundary layer, $\delta$. The resulting form of the momentum integral equation is:

$$-\tau_y = \frac{d}{dx}\int_y^\delta \rho u^2 dy - \rho v_\delta u_\infty - \rho v_y u_y \tag{A3.6}$$

The ratio of Eq. A3.6 evaluated at y = y, to Eq. A3.6 evaluated at y = 0, using the velocity power function approximation from Eq. 3.3 resulted in:

$$\frac{\tau_y}{\tau_s} = 1 - \left( \frac{y}{\delta} \right)^{\left( \frac{n+2}{n} \right)} \tag{A3.7}$$

Combining Eq. A3.7 with the mixing layer analogy of shear stress in a turbulent flow $\tau / \rho = [\nu + \varepsilon_m] \partial u / \partial y$ and solving for $[\nu + \varepsilon_m]$, the following expression was obtained:

$$[\nu + \varepsilon_m] = n \nu \frac{c_f}{2} \left( \frac{\delta}{x} \right) Re_x \left[ 1 - \left( \frac{y}{\delta} \right)^{\left( \frac{n+2}{n} \right)} \right] \left( \frac{y}{\delta} \right)^{\left( \frac{n-1}{n} \right)} \tag{A3.8}$$

Using the approximation $Sc_T \approx 1$ for high Sc fluids (Bird et al. 2002; Kays et al. 2005) and that within the concentration boundary layer $\nu >> \varepsilon_m$, the sum of the molecular diffusion coefficient D ($m^2\ s^{-1}$) and $D_T$ can be expressed in terms of $[\nu + \varepsilon_m]$ as:

$$[D + D_T] \approx Sc^{-1}[\nu + \varepsilon_m] \tag{3.6}$$

Using Fick's First Law:

$$J = -[D + D_T]\frac{\partial C}{\partial y} \tag{A3.9}$$

and evaluating the product of the derivative of Eq. 3.4 and Eq. A3.8 in Eq. 3.6 for y = 0, the surface DO flux, $J_s$ is:

$$J_s = Sc^{-1}\frac{\tau_s}{\rho u_\infty^2} u_\infty \left(\frac{\Delta}{\delta}\right)^{-\left(\frac{1}{n}\right)} (C_s - C_\infty) \tag{A3.10}$$

Substituting Eq. A3.1 into Eq. A3.10 and Eq. A3.10 into Eq. A3.5 and integrating from 0 to x, an expression for the ratio of the two boundary layers was derived:

$$\frac{\Delta}{\delta} = \left(Sc^{-1}\left(1 - \delta^{\left(\frac{n+2}{n+1}\right)}\right)\right)^{\left(\frac{n}{n+2}\right)} \tag{A3.11}$$

Eq. A3.11 can be expressed in terms of x from the expression for $\delta(x)$ given in Eq. A3.3. then substituted into Eq A3.10, to arrive at the final expression for kelp surface DO flux:

$$J_s(x) = ASc^{-\left(\frac{n+1}{n+2}\right)} Re_x^{-\left(\frac{2}{n+3}\right)} u_\infty (C_s - C_\infty) \tag{3.7}$$

# Chapter 4 Photosynthesis increases surface shear stress inside algal mats

The filamentous alga *Cladophora glomerata* is widespread in freshwater ecosystems worldwide with a significant presence in human impacted systems that have either high incident light or high dissolved nutrient levels (Higgins et al. 2008). Although not a preferred food source itself, *Cladophora*'s dense filamentous mats can increase underwater habitable surface areas for micro-organisms more palatable to grazers, thus acting as an important regulator of stream productivity (Marks & Power 2001, Vanden Heuvel et al. 2010, Power et al. 2009). We investigated how micro-scale surface characteristics, altered by the presence and type of attached micro-organisms, affect surface shear stress, or local skin drag, and thus indirectly, nutrient availability in the vicinity of *Cladophora* filaments. We demonstrate that surface shear stresses on filamentous algae are higher during photosynthesis than when the algae are not actively photosynthesizing and that the presence of attached diatom assemblages reduces surface shear stress. We suggest that bubble nucleation within the filament's boundary layer, due to supersaturation of dissolved oxygen, is responsible for increasing surface shear stresses by increasing local velocity gradients. An enhanced local shear stress creates a positive feedback loop where the nutrient concentration boundary layer becomes thinner and nutrient flux to the filament increases leading to higher photosynthetic rates under mass

transfer limited conditions. Higher photosynthetic rates promote larger oxygen efflux and thus generate higher velocity gradients in proximity of the filament. The proposed positive feedback could be an important bio-physical mechanism to overcome diffusion limited nutrient supply within dense algal mats, thereby regulating *Cladophora* survival at high cell densities and prolonged duration of algal blooms.

## 4.1 Introduction

*Cladophora glomerata* is a widespread freshwater filamentous alga found throughout temperate regions worldwide (Dodds 1991, Higgins et al. 2008). It grows quickly, sometimes forming dense mats that cause problems such as clogged water intakes, foul odors and may harbor fecal pathogens (Dodds and Gudder 1992, Ishii et al. 2006). It is tolerant of both eutrophic and high light, oligotrophic conditions (Higgins et al. 2008). As a macroalgae, it obtains all required nutrients from the surrounding water. Nutrient availability is dependent on the bulk and near algal nutrient concentrations and local water motion (Borchardt 1994).

*Cladophora* filaments can host a wide range of attached micro-organisms, such as diatoms, bacteria, and microalgae, whose assemblage composition varies with differences in water chemistry, light, flow and season, resulting in varied and complex 3-D structure around the filament (Lowe 1982, Marks & Power 2001). By providing structural complexity and colonizable surface area, *Cladophora* mats greatly enhance stream micro-organism abundance and have been referred to as stream area multipliers (Power et al. 2009). Although *Cladophora* is not thought to be palatable to grazers itself, the micro-organisms attached to *Cladophora* are an important food source for grazers and thus

*Cladophora* plays a critical supporting role in stream food web dynamics (Dodds & Gudder, 1992). The primary reported effect of attached micro-organism assemblages on submerged aquatic vegetation is increased shading (Dodds 1991) which is detrimental when low light availability is limiting growth (Köhler et al. 2010, Drake et al. 2003). In addition to physically covering the filament surface, attached micro-organisms increase surface roughness, and may change surface wettability properties (i.e. hydrophobicity, hydrophilicity) due to different material composition from the host, such as the silica diatom frustule (Losic et al. 2009).

The recent attention focused on flow through submerged macrophytes and terrestrial canopies (e.g. Ghisalberti & Nepf 2002, Carollo et al. 2002, Raupach et al. 1996) is not directly applicable to flow through algal mats. Algal mats tend to be denser than macrophyte canopies with smaller diameter elements. A few studies have measured flow through algal mats, finding an exponential decay in mean velocity with depth (Dodds & Biggs 2002) and that flow through algal mats is more analogous to porous media flow than to canopy flow (Escartin & Aubrey 1995). To our knowledge, microscale velocity fields near filamentous algae surfaces have not been measured and shear velocity or free stream velocity are typically used to estimate diffusion boundary layer thickness (e.g. Larned et al. 2004). In micro-scale studies on highly engineered surfaces such as silicon wafers, surface roughness, surface hydrophobicity and a near-surface gas layer have been shown to change surface shear stresses and slip velocity in shear flows (reviewed in Neto et al. 2005).

## 4.2 Methods

We investigated how attached micro-organisms and filament physiological state affect surface shear stress and skin drag at the scale most relevant to nutrient uptake and gas exchange of microns. Near-surface velocity fields were measured for a variety of individual *Cladophora* filaments including; filaments with different attached micro-organism assemblages, live vs. preserved filaments, and light vs. dark exposed filaments. Velocity fields near a stainless steel wire were also measured for comparison. From these velocity field measurements, the surface shear stress, $\tau_s$ (kg $m^{-1}$ $s^{-2}$) and the drag coefficient, $C_D$, were determined for various discharge velocities.

### *4.2.1 Field velocity measurements*

Field velocity measurements were conducted on June 23, 2009 within a mat of *Cladophora* in the Eel River (Angelo Range Research Reserve, California, U.S.A.) (Fig. 4.2A). Vertical velocity profiles were measured through a large, dense *Cladophora* mat using a side-facing acoustic-Doppler velocimeter (ADV) (Vectrino model, Nortek AS, Oslo, Norway). Velocity was measured at a maximum vertical spacing of 4 cm with tighter spacing near the top of the *Cladophora* mat where a gradient was expected. A velocity profile was taken above the intact mat then, after cutting an opening, a second profile was taken through the mat to the sediment-water interface. This method, developed by (Ikeda & Kanazawa 1996), has been used successfully by other researchers (Ghisalberti & Nepf 2006, Ghisalberti & Nepf 2002, Plew et al. 2008) and is necessary for in-canopy velocity measurements using an ADV in order to avoid interference within the measurement volume. At each vertical location, velocity was measured for 3 minutes

at a sampling frequency of 200 Hz, resulting in 36,000 measurements per location. These measurements were used to calculate the time-averaged velocity, $\overline{U}$ (m $s^{-1}$) and the Reynolds stresses, $-\overline{u'w'}$, ($m^2$ $s^{-2}$) for each measurement location. The mat height was 0.25 m and the water depth was 0.45 m. Attached micro-organism species were microscopically identified to be 96% the diatom *Cocconeis pediculus*.

### *4.2.2 Sample preparation*

For the laboratory experiment, a variety of algal filaments was selected to exhibit a wide range of roughness characteristics through surface colonization by micro-organisms. Filaments classified as "bare" were cultured in a laboratory mesocosm with diatom growth minimized by limited silicon supply in the growth media and bacteria growth controlled with UV irradiation of the recirculating water. The filament with a bacterial biofilm was a cultured bare filament that was placed in a solution with high levels of bacteria. Bacteria coverage was confirmed visually using a Nikon E400 light microscope with a 100x objective. Filaments with attached diatom assemblages were collected from both the field site at ACRR (Fig 4.3A, images b and d) and locally from the Mississippi River (Fig 4.3A, image e). The preserved filament was a cultured, bare filament, soaked in 70% ethanol for 16 hours, rinsed, then stored at 4 ºC. A single cultured, bare filament was used for the light-dark experiment. Filament diameters ranged from approximately 80 to 150 $\mu$m. After collection all filaments were stored in growth media at 4 ºC for up to 48 hours. 304 stainless steel wire with 127 $\mu$m diameter was used for comparison. Care was taken to not touch the wire with bare hands.

### *4.2.3 Laboratory experimental setup*

Fluid motion was measured using a micro-scale particle image velocimetry system ($\mu$PIV) (Fig. 4.1, TSI Inc., Shoreview, MN, U.S.A.). Conceptually, $\mu$PIV quantifies fluid velocity fields by measuring the displacement of neutrally buoyant seed particles within the measurement plane over a known time interval (e.g. Wereley & Meinhart 2010). These "instantaneous" measurements are typically time-averaged to remove the random noise generated by Brownian motion for particles of this size.

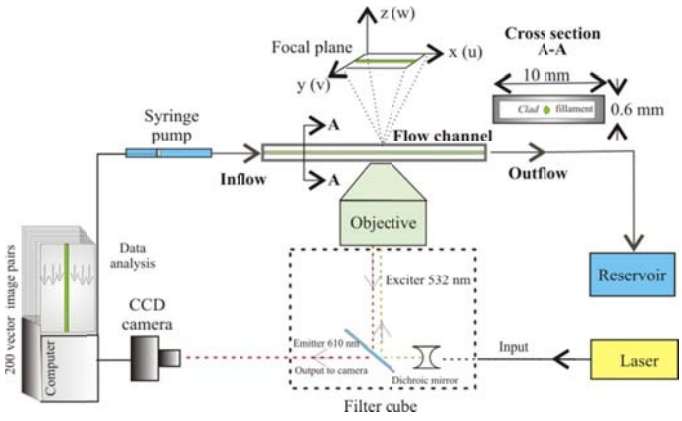


**Fig. 4.1** $\mu$PIV TSI system schematic.

In the setup, a fluid consisting of 1 $\mu$m diameter fluorescent polystyrene latex spheres (Thermo Fisher Scientific Inc., Waltham, Massachusetts, USA) suspended in ultra-pure water was pumped past individual filaments, tethered in the center of a high aspect ratio acrylic channel (1cm x 0.06 cm x 5 cm). Flow rates were controlled by a syringe pump (NE-500 model, New Era Pump Systems, Inc., NY, USA) and ranged from 0.5 to 5.0 mL/min (+/-0.05 mL/min) with corresponding discharge velocities from 0.14 cm $s^{-1}$ to

1.4 cm $s^{-1}$. This range was chosen to match the experimental velocity range to the velocity range measured within the algal mat in the field. Seed particles were illuminated by a double pulsed Nd:YAG laser (532 nm emission wavelength). The microscope objective was focused at the filament surface at a depth corresponding to the centerline of the filament. Image pairs were captured through an inverted microscope (Nikon Eclipse TE2000-S) with a 10X DIC objective lens (Nikon Plan Fluor) using a double frame CCD camera (pixel size 6.5 $\mu$m, PIVCAM 14-10). The displacement of each particle was determined by cross-correlation mapping of the two consecutive images over (96 pixel x 96 pixel) interrogation windows covering a total mapped area of 300 $\mu$m x 450 $\mu$m. The velocity field was time-averaged across 200 image pairs. Velocity fields were measured for 9 algal filaments and the steel wire at various flow rates resulting in 57 measured velocity fields.

### *4.2.4 Light-dark experimental setup*

The light-dark experiment was conducted using a three-dimensional (3-D) digital holographic system (Sheng et al. 2006) with a low energy, long wavelength laser (emission wavelength 632.8 nm). Similar to the $\mu$PIV system described above, velocity fields are measured by tracking particle displacement over a known time interval. In this system however, the laser light is split into two paths so that 3-D particle movement can be digitally reconstructed using depth information found in the interference fringes. To compare these results with results from the 2-D system above, a 20 μm deep slice was extracted from the volume data at the centerline of the filament and used to provide near surface, 2-D velocity information. The flow was seeded with a sparse suspension of 2.9

μm latex microsphere particles (Thermo Fisher Scientific Inc., Waltham, Massachusetts, USA) in ultrapure water. Effective particle density for the analysis was increased by building surrogate images consisting of 30-90 actual images randomly selected and overlaid. Two hundred surrogate pairs were averaged to generate the time-averaged surface velocity fields.

The light-dark experiment was conducted using a single algal filament for both sets of measurements. The channel and pump were identical to that used in the $\mu$PIV experiments. After measuring velocity fields near a fresh, photosynthesizing filament, the seed solution was pumped out of the channel and replaced with growth media. For the next 48 hours the filament was in total darkness, after which, the channel was again filled with seed solution and velocity fields were measured with the laser as the only light source. After the extended exposure to dark conditions, the experimental filament appeared brown, however, by exposing it to light until the chlorophyll appeared green (3 hours), was verified to be alive and photosynthesizing.

### *4.2.5 Determination of the velocity gradient*

Surface shear stress, $\tau_s$, was calculated from the slope of the velocity profiles at the surface of the filament where:

$$\tau_s = \mu \left. \frac{\partial \overline{U}}{\partial y} \right|_{y=0} \tag{4.1}$$

and $\mu$ (kg $m^{-1}$ $s^{-1}$) is the dynamic viscosity of the fluid. A spatially averaged velocity gradient adjacent to the filament surface was determined by averaging across all

individual gradients within the camera's field of view (FOV) ($\mu$PIV: 20 gradients within FOV of 0.35 mm x 0.45 mm, holographic PIV: 113 gradients within FOV of 1.4 mm x 1.4 mm). This was repeated for each flow rate and each filament. Surface shear stress was then used to calculate $C_D$, mathematically defined as:

$$C_D \equiv \frac{8\tau_s}{\rho U_D^2} \tag{4.2}$$

where $U_D$ (m $s^{-1}$) is the discharge velocity. The fluid physical properties density, $\rho$ (kg $m^{-3}$) and $\mu$, were obtained for water at 25 ºC. The results were compared across a range of flow conditions represented non-dimensionally with Reynolds number, Re where Re is defined as:

$$Re = \frac{\overline{U} D_h}{\nu} \tag{4.3}$$

and where $\nu$ ($m^2$ $s^{-1}$) is the kinematic viscosity and $D_h$ (m) is the hydraulic diameter of the channel. The velocity range used in laboratory experiments was determined from the field velocity measurements within *Cladophora* mats described above.

## 4.3 Results

Time-averaged, stream-wise velocity, $\overline{U}$ (m $s^{-1}$), measured within the *Cladophora* mat ranged from 0.008 cm $s^{-1}$ to 1.00 cm $s^{-1}$ (Fig. 4.2B); a decrease of over two orders of magnitude from the free-stream velocity to the lowest velocity within the mat. Within the same mat, Reynolds stresses, $-\overline{u'w'}$ ($m^2$ $s^{-2}$), which can be used to quantify the

strength of the turbulence of the flow, were essentially zero (Fig. 4.2C) and the flow was laminar.

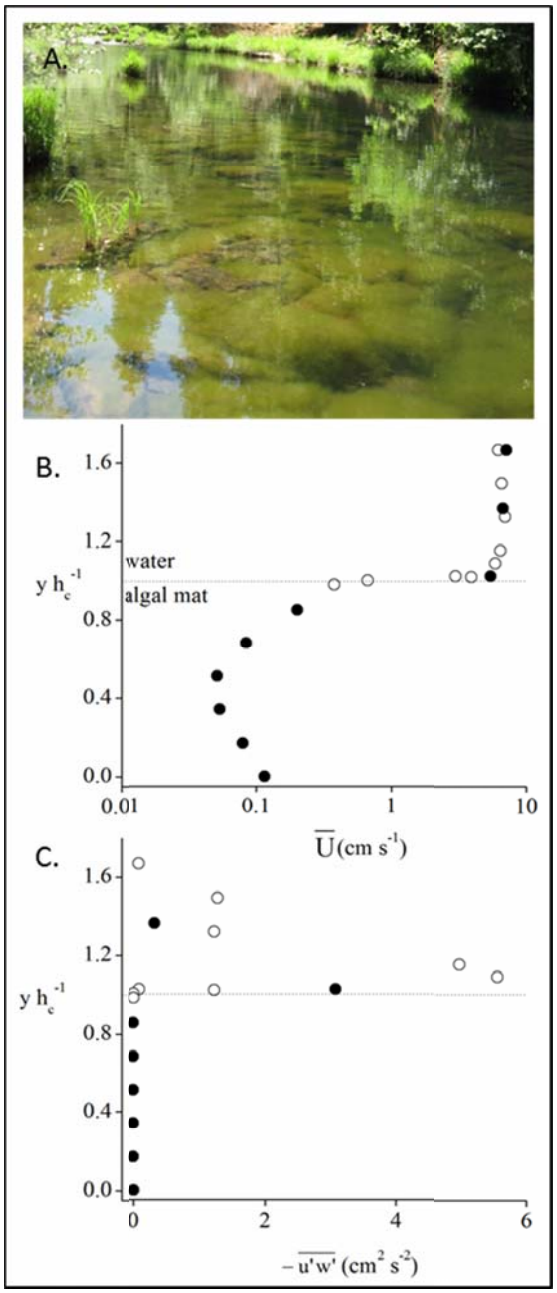


**Fig. 4.2** A. Photograph of the *Cladophora* mat where velocity was measured. B. Vertical time-averaged stream-wise velocity profiles through *Cladophora* mat. Open circles are from profile taken above the intact

mat. An opening was cut into the mat then a second profile (solid circles) was taken through the mat to bottom of the river channel. C. Measurable Reynolds stresses, $-\overline{u'w'}$ ($m^2\ s^{-2}$) did not extend into the mat.

In laboratory experiments, two-dimensional velocity fields next to the filament surface were measured and time-averaged using microscale particle image velocimetry ($\mu$PIV) (e.g. Fig. 4.3A). From the velocity field, the slope of each profile next to the filament was determined and averaged to calculate the spatially averaged velocity gradient $\langle \partial \overline{U} / \partial y \rangle$ at the filament surface. For all filaments, $\langle \partial \overline{U} / \partial y \rangle$ was larger for non-photosynthesizing filaments than for filaments that were photosynthesizing (Fig. 4.3B).

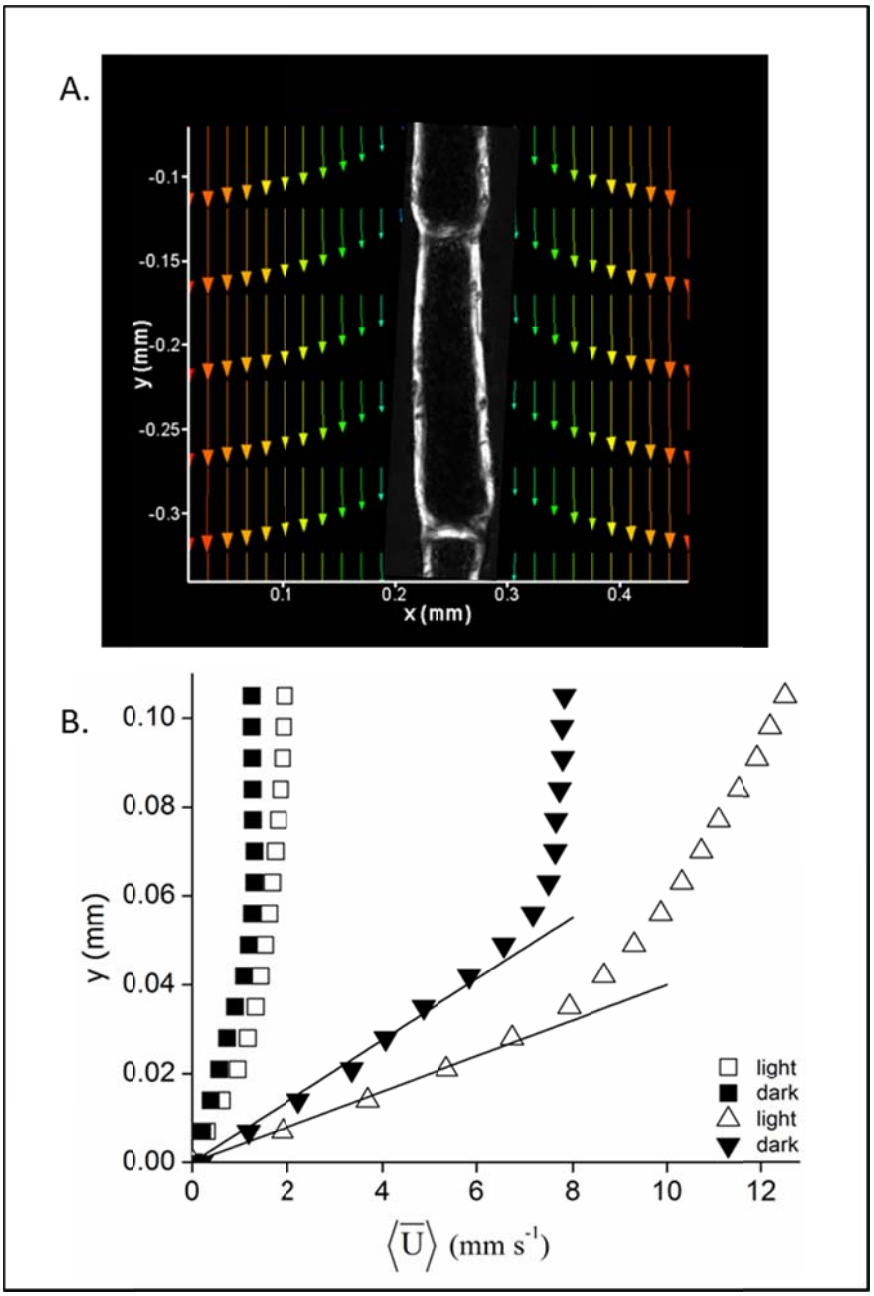


**Fig. 4.3** A. Illustration of time-averaged velocity data as measured using $\mu$PIV. For illustration purposes, a microscope image of a filament is superimposed on the velocity field and only 1/3 of the velocity vectors are shown. B. Time-averaged and spatially averaged velocity profiles next to a single filament for channel flow rates of Q = 0.5 mL $min^{-1}$ and Q = 3.0 mL $min^{-1}$. The experiment was run under light-exposed conditions (open symbols) then the system was covered up for 48 hours and the experiment was re-run under dark-exposed conditions (closed symbols).

From the velocity gradient and the pump flow rate, the drag coefficient, $C_D$ and the Reynolds number, Re, were determined for each filament at each flow rate. For all filaments $C_D$ was inversely proportional to Re, resulting in a straight line on a log-log scale (Fig. 4.4b).

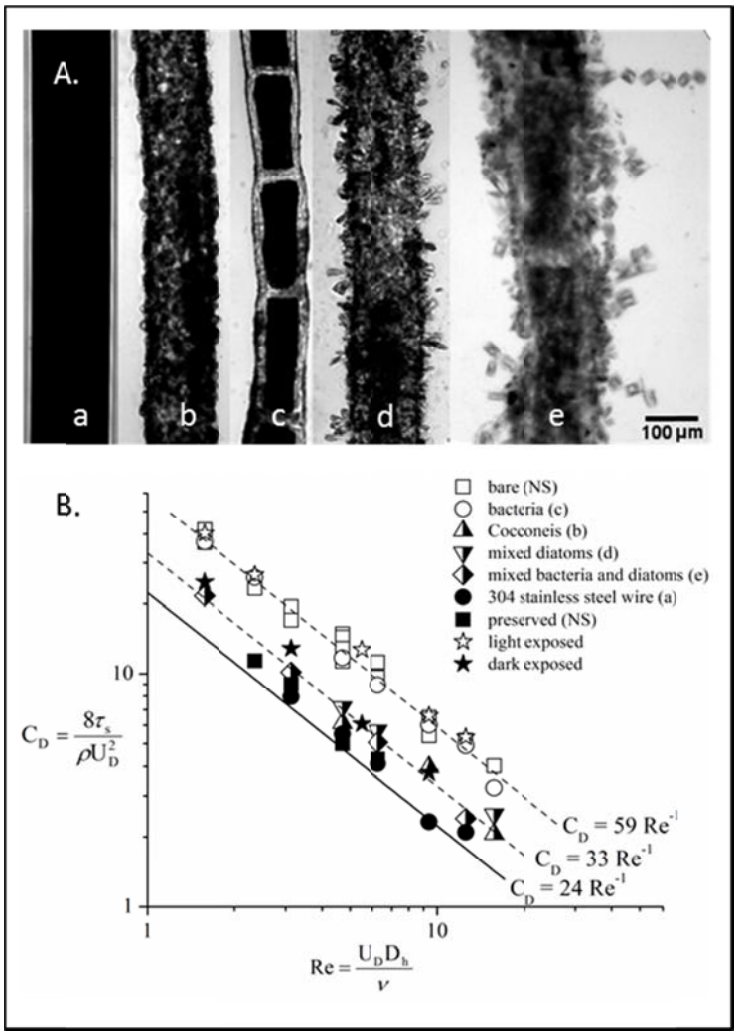


**Fig. 4.4** A. Microscope images of some of the filaments used for the experiments including; stainless steel wire (a), *Cocconeis spp.* diatom dominated assemblage (b), bacterial biofilm assemblage (c), mixed diatom assemblage (d), mixed diatom/bacteria assemblage (e). B. Experimental results demonstrating the

relationship between the drag coefficient, $C_D$, and the Reynolds number, Re. Black line represents the analytical solution to conservation of momentum for laminar flow in a closed rectangular channel with cross section dimensions of 10 mm x 0.6 mm.

All results for live, algal filaments fell above the theoretically predicted line for internal laminar flow, indicating that the surface shear stresses were higher at the surface of the live filaments than predicted by the analytical solution to flow through a closed rectangular channel. Results from live filaments with bacterial biofilms or with few surface micro-organisms collapse onto the line $C_DRe = 59$ ($r^2 = 0.98$, $n = 28$). Measurements near the stainless steel wire resulted in the relationship $C_DRe = 25$ ($r^2 = 0.99$, $n = 5$), which agrees well with the theoretically predicted relationship $C_DRe = 24$ for internal laminar flow between two parallel plates (e.g. Shaughnessy et al. 2005). This agreement indicates that error incurred from the experimental setup was minimal. Results for preserved algal filaments, $C_DRe = 27$ ($r^2 = 0.98$, $n = 4$), were also quite close to the analytical solution and to results from the steel wire. Results for live filaments with predominately diatoms on the filament surface fell between the results for live and preserved filaments. A further set of experiments was conducted to compare velocity fields for a single filament after extended exposure to either light or dark conditions. After 48 hours dark exposure, the filament still showed an enhanced shear stress compared to the preserved filament but it was much less than that recorded for the same filament under light conditions (Fig. 4.3b). Under light-exposed conditions, the filament behaved the same as all other live, photosynthesizing filaments in the experiment.

## 4.4 Discussion

Comparisons of results between light-dark and live-preserved filaments indicate that photosynthesis increased local surface shear stresses and skin drag for the filamentous algae *Cladophora* at velocities measured within mats in the field. Based on previous work on microscale surfaces, known causes for an increase in surface shear stress are; surface roughness, surface hydrophobicity, and surface gas layer (Neto et al. 2005). We suggest that the measured increased surface shear stresses were the result of bubbles or a gas layer near the filament surface. Results did not correlate with filament roughness. The observed enhanced surface shear stress would potentially result in higher nutrient availability, stimulating photosynthesis, higher contaminant exposure, and higher epiphyte immigration rates.

### *4.4.1 Nutrient uptake*

Velocity profiles measured within a *Cladophora* mat (Fig. 4.1) depicted exponential decay; similar to previously reported measurements (Escartin & Aubrey 1995, Dodds & Biggs 2002) (Fig. 4.2). The surface shear stresses at a photosynthesizing algal surface, shown to be over two times greater than predicted from laminar flow theory, can be used to estimate nutrient uptake by *Cladophora*. The nutrient flux at the algal surface, $J_s$, can be described as:

$$J_s = -D\frac{\partial C}{\partial y}\Big|_{y=0} \cong \frac{-D}{\delta_c}\Delta C \qquad (4.4)$$

where D is the coefficient of diffusion of the nutrient in water, $\delta_c$ is the concentration boundary layer thickness, and $\Delta C$ is the difference in nutrient concentration between the

bulk, in-mat nutrient concentration and the nutrient concentration at the filament surface. From scaling arguments at the edge of the concentration boundary layer (e.g. Steinberger & Hondzo 1999):

$$\delta_c = c_1 \frac{\nu}{u_*} Sc^{-1/3} \quad (4.5)$$

where $u_*$ is the shear velocity, and Sc is the Schmidt number where $Sc = \nu D^{-1}$. The constant $c_1$ is empirically derived and typically found to be between 10 and 20 (e.g. Steinberger & Hondzo 1999, Levich 1962, Dade 1993). Shear velocity, $u_*$ is defined as:

$$u_* \equiv \sqrt{\frac{\tau_s}{\rho}} \quad (4.6)$$

This can be expressed in terms of the drag coefficient using Eq. (4.2):

$$u_* = U_D \sqrt{8C_D} \quad (4.7)$$

Substituting Eq. (4.7) into Eq. (4.4), $J_s$ can be expressed in terms of $C_D$:

$$J_s = aU_D Sc^{-2/3} \Delta C \sqrt{C_D} \quad (4.8)$$

where $a = -\sqrt{8}/c_1$.

Substituting the expression for $C_D$ from Fig. 4.3B into Eq. (4.8) and examining the ratio, it is seen that the presence of diatom assemblages would decrease nutrient uptake by 25%. Similarly, nutrient uptake projections based on laminar flow theory (i.e. $C_D = 24\ Re^{-1}$) would underpredict actual flux by 46%, compared to flux calculations from experimentally measured velocity gradients.

### *4.4.2 Bubbles*

The reported increase in drag may be due to the presence of small stable bubbles which form due to supersaturated oxygen concentrations in the boundary layer near the filament. This phenomenon has been reported for photosynthetic microbial mats where stable, oxygen-rich, microscale bubbles formed at oxygen concentrations near the biomass of 200 μM (Bosak et al. 2010). For comparison, in field measurements within the sampled algal mat, DO concentrations were 300 μmol $L^{-1}$ at mid-day; well above a concentration for which bubble formation would occur. Based on our laboratory measurements, oxygen was released from *Cladophora* into the water at a rate of 175 μmol $O_2$ $hr^{-1}$ $(g\ DW)^{-1}$. At this flux rate, oxygen concentrations in the channel would be high enough for bubble formation to occur in little over one hour. Both oxygen supersaturated water and oxygen-rich bubbles would increase the effective viscosity of the near-surface fluid (Valukina & Kashinskii 1977; Pal 2007) resulting in a larger drag coefficient.

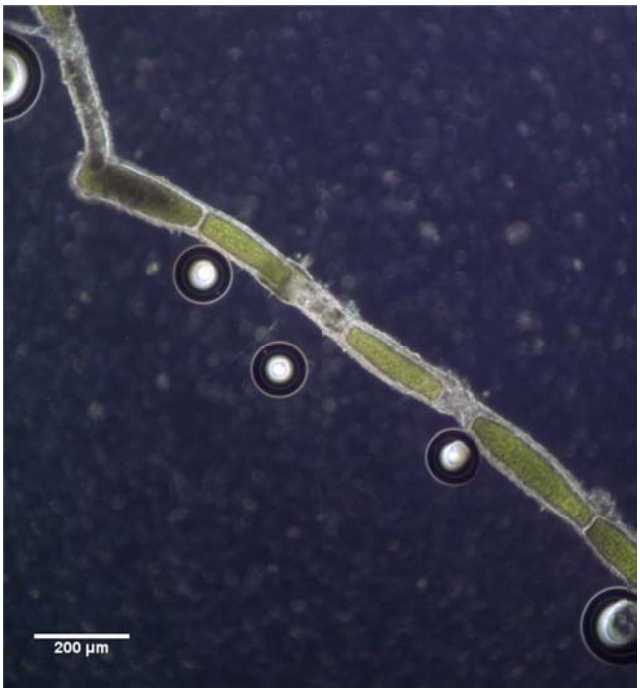


**Fig 4.5** Bubbles formed at surface of *Cladophora* filament after light exposure in solution of growth media and 1 $\mu$m seed particles.

Bubble formation occurred after 3 hours in sealed microscope slides with a 10% seeding solution in growth media (Fig. 4.5). Bubbles did not form in slides prepared with stainless steel wire. Bubbles did not form in slides with pure growth media; probably due to lack of nucleation sites. In the field, suspended sediment could provide bubble nucleation sites.

### *4.4.3 Epiphyte colonization*

Attached assemblages, consisting primarily of diatoms, lowered filament skin drag more than bacterial biofilms or sparse attached bacterial communities (Fig. 4.3B). Diatoms assemblages can cover large areas of the filament surface, decreasing the light

available to the filament, physically blocking gas exchange, and excreting mucilage, all of which may alter surface wettability. Previous studies at a mat scale, much larger than the scale at which this study was conducted, found that diatom assemblages decreased drag (Dodds 1991) and decreased photosynthesis (Sand-Jensen 1977). To our knowledge, no studies have examined both variables simultaneously. It has been shown that diatom assemblages decreased skin drag compared to bare filaments and that photosynthesis caused elevated skin drag for bare photosynthesizing filaments. It is not possible to conclude from the results of this study whether diatoms are blocking metabolic gas exchange or are blocking incident light.

### *4.4.4 Surface roughness*

Surface roughness did not have a measurable effect on surface shear stresses or drag in this experiment despite have been reported to change surface shear stresses at micro-scales (Harting et al. 2010) and to increase drag forces in macro-scale turbulent flows as is classically shown using the friction factor, $f$, mathematically equivalent to $C_D$, in the Moody diagram. If roughness had been responsible for the observed increase in surface shear stress, then the smooth, bare algal filaments (Fig. 4.2A, panel c.) should have behaved more like the stainless steel wire than like the filaments with surface diatom communities (Fig. 4.2A, panels b, d, e), which are much rougher. Additionally, if roughness had been responsible for increased surface shear stress, the preserved filament and dark exposed filaments would have behaved the same as the live, light-exposed filaments.

## 4.5 Conclusion

Through microscale studies at the surface of *Cladophora* filaments, shear stresses and thus drag forces were shown to be two times greater for photosynthesizing filaments than for preserved or non-photosynthesizing filaments. Nutrient uptake estimates based on fluid flow theory underpredict flux by nearly 50% compared to calculations done using measured velocity gradients in our study. The presence of diatom epiphytes decreased the surface shear stress compared to bare, photosynthesizing filaments, and thus decreased nutrient uptake by 25% under our experimental conditions. This suggests that *Cladophora* and possible other mat forming species, can overcome the physical and physiological constraints on nutrient and $CO_2$ uptake imposed by low flow rates through dense filament assemblages. Understanding how mat forming algal species persist could provide useful input for population control under nuisance conditions as well as valuable insight into ecological dynamics under all conditions.

# Chapter 5 Epiphytes decrease submerged aquatic vegetation uptake of phosphorus in a constructed wetland

Submerged aquatic vegetation (SAV) has major effects on the physical and chemical environment within its canopy, altering such characteristics as dissolved oxygen concentration, pH, temperature, light availability, and water motion. Due to some of the effects of SAV on the local environment, it is an important component of constructed wetland design. SAV leaves and stems typically host epiphyte assemblages which may alter SAV productivity by decreasing light and nutrient availability at the plant surface. We investigated the effect of epiphytes on water column concentrations of soluble reactive phosphorus (SRP) and dissolved oxygen (DO) inside a SAV canopy within an urban constructed wetland. These results show that epiphyte removal increased SAV productivity resulting in lower SRP and higher DO throughout the water column. Under controlled laboratory conditions, epiphyte detachment was shown to be a function of fluid velocity, which could be manipulated in the field. These findings could be used to better design and operate constructed wetlands through active management of the SAV epiphyte accumulation.

## 5.1 Introduction

Submerged aquatic vegetation (SAV) has major effects on the physical and chemical environment within its canopy and in surrounding waters, altering such characteristics as dissolved oxygen concentration, pH, temperature, light availability, and water motion. The production of oxygen, a byproduct of photosynthesis, in dense SAV canopies, can create diurnal oxygen fluctuations strong enough to support a daytime oxic layer and a nighttime anoxic layer with depleted oxygen concentrations at the sediment-water interface (Carpenter & Lodge 1986). In dense SAV canopies, total irradiance can be reduced by up to 95% in the upper 20 cm of the water column (Pokorny et al. 1984). Intense photosynthesis in SAV canopies can change pH and water temperature, creating strong vertical gradients in the water column (Carpenter & Lodge 1986). Vertical profiles of time-averaged velocity exhibit a decrease and an inflection point within the canopy whereas turbulent intensity has a sharp maximum at the top of the canopy then quickly decay to minimal levels (Raupach et al. 1996, Ghisalberti & Nepf 2002).

With its connection to the sediment through its roots and to the water column through its stem and leaves, SAV can access nutrients in both the sediment and the water column with the preferred pool determined by relative water and sediment concentrations and by plant species (Carignan & Kalff 1982). Although sediment phosphorus (P) concentrations are often an order of magnitude larger than water P concentrations, stem and leaf resistance is less and the bioavailable form of P, soluble reactive phosphorus (SRP), is readily accessed from the water column (Eugelink 1998, Madsen & Cedergreen, 2002). P uptake by SAV is largely driven by metabolic demand, however,

many plants, including *E. canadensis*, exhibit luxury P uptake and storage (Thiebaut & Miller 2003) thus contributing more to P drawdown than would be anticipated from productivity rates alone. At the end of the growing season when plants are senescing, SAV releases nutrients back into the water column as well as translocating nutrients to the roots for overwinter storage (Wetzel 2001). Although SAV itself does not represent a permanent storage for P, it temporarily dampens the magnitude of P exiting the wetland and may enhance P burial, contributing to intermediate storage.

Due to effects on local environmental conditions, the characteristics and functioning of SAV are important aspect of constructed wetland design. Constructed wetlands decrease the flow of P from urban stormwater runoff to lakes and rivers where it can lead to eutrophication. Wetlands capture excess phosphorus by slowing the water down, which allows P bound to suspended particles to settle out of the water column, and by autotrophic uptake of SRP from the water as it passes through the wetland (Kadlec & Wallace 2008, Reddy et al. 1999). SAV, with the majority of its biomass located in the water column, influences water P concentrations by; slowing in-canopy flow, releasing DO into the water column, and capturing P from the water column.

SAV leaves and stems typically host epiphyte assemblages which can consist of algae, bacteria, diatoms, and other micro-organisms, as well as attached fine sediments that have deposited out of the water column. Many epiphytes also take up P from the water column and both SAV and epiphytes influence local P water concentrations (Pelton et al. 1998). Although epiphytes easily access SRP in the water column, they also release it all back to the water column with no long term storage potential and much fast cycling

times than SAV (Pelton et al. 1998). In high nutrient conditions, epiphytic and planktonic algae may grow so dense that they cause the collapse of the SAV community by outcompeting for light (the alternate stable states) (May 1977, Scheffer 1993).

Through laboratory studies typically on single leaves, epiphytes have been shown to decrease the light available to SAV (Sand-Jensen 1977, Drake et al. 2003, Asaeda et al. 2004) although there is disagreement on whether this limits productivity under field conditions where turbidity, bank vegetation, and self-shading may have more important influences on light availability (Sand-Jensen et al. 2007, Kohler et al. 2010). We know of no studies that have examined SAV responses to epiphyte coverage spatially. It is possible that in the high light conditions near the air-water interface, epiphyte shading is not enough to suppress photosynthesis and also that near the sediment-water interface, light extinction is already so extreme that epiphyte coverage does not further contribute.

We investigated the effect of SAV epiphytes on the water column concentrations of SRP and DO inside a SAV canopy within an urban constructed wetland. We hypothesized that epiphyte removal would allow SAV greater access to light leading to higher DO concentrations, thus capturing more SRP from incoming flow and reducing SRP flux from the sediment into the water column. This was measured by taking direct DO measurements and precisely located water samples for vertical measurement profiles during 4 sample events before and after epiphyte removal. Through laboratory experiments a relationship was developed showing epiphyte detachment as a function of flow conditions. To our knowledge, this is the first study to provide vertical spatial resolution of the effect of epiphyte coverage on photosynthetic rates and SRP uptake

within an intact, functioning canopy. With a more mechanistic understanding of the role of the SAV epiphyte load on P dynamics, constructed wetlands could be designed to optimize P uptake by using flow characteristics to influence epiphyte load.

## 5.2 Methods

### *5.2.1 Site description*

Field experiments were conducted in dense, intact SAV canopies within a single cell of the Villa Park constructed wetland (VPCW) in Roseville, MN, USA (Fig. 5.1a). VPCW was constructed in 1985 as a best management practice to remove phosphorus and suspended sediment from stormwater runoff entering Lake McCarron, and ultimately, the Mississippi River (Villa Park Wetland Management Plan, 2009). VPCW is fed by runoff from 753 acres of fully developed, largely residential, urban land primarily via storm sewers (Villa Park Wetland Management Plan, 2009). SAV canopies consisted primarily of *Elodea canadensis*, elodea, and secondarily of *Ceratophyllum demersum*, coontail. *Lemna minor*, duckweed, was present but sparse until September 7, after which it completely covered the water surface (Fig. 5.1c). Except for 13 July, SAV canopies extended the depth of the water column on all sampling dates. All SAV canopies were located within 20 m from each other (Fig. 5.1a).


**Fig. 5.1** Field site and sampling setup. All field work was completed within the Villa Park Constructed Wetland (panel a), within a 20 m diameter sampling region (panel a, circled area). The star indicates location of the weather station (panel a). Also shown are the vertical profiling system (panel b) and a view downstream from the site during the *L. minor* bloom (panel c).

### *5.2.2 Field measurements and sample collection*

Vertical profiles of DO and SRP were measured in dense, intact SAV canopies over 5 sample dates between July 13, 2011 and September 17, 2011. Because the treatment changed the epiphyte coverage on SAV, measurements for each sampling event were in separate canopies. All samples were collected between 9:00 AM and 1:00 PM. Dissolved oxygen (DO) concentration was measured *in situ* using a Clark-type dissolved oxygen needle sensor (OX-N; Unisense, Aarhus, Denmark) connected to a pico-ammeter for signal amplification (PA2000; Unisense, Aarhus, Denmark). The DO sensor was mounted on a manual vertical profiling system with an accuracy of 0.2 cm in the z-direction (Fig 5.1b). The profiler was secured and leveled at the beginning of each

experiment after which it remained in the same location for the sample date. DO concentration was sampled for 3 minutes at 50 Hz sampling rate resulting in 9000 measurements per measurement location. DO sensors were calibrated each morning before sampling using a 2-point calibration with air saturated water and a sodium sulfide solution. Water samples were collected from each height in the profile using acid-washed silicone tubing and a 60 mL syringe mounted on the manual vertical profiler described above. For the treatment mechanism experiment, 3 water samples were drawn at a depth of 10 cm below the water surface. A preliminary draw of water from each location was used to rinse the syringe and bottle before sample collection. Water samples were stored in 60 mL, acid-washed Nalgene bottles in a cooler with ice packs until return to the lab.

On each sample date, initial profiles were collected in the undisturbed SAV canopy. Then, epiphytes and attached sediment were removed by gentle mechanical agitation of the SAV within an area of approximately 0.5 m diameter directly below the measurement probes. Care was taken to not disturb the sediment or to break the plant stems. Plants were periodically agitated for 30 minutes until there was no visible release of material in the surrounding water, and then were left undisturbed for 30 minutes. After the 30 minute settling period, another set of vertical profiles were measured at the same location. To verify that the released epiphytes were not suspended in the immediate sampling area, water samples were taken before and after agitation, filtered and dried to compare suspended material load. To quantify the effectiveness of the treatment at

removing the attached material, plant samples were collected before and after treatment for laboratory quantification of the epiphyte removal effectiveness.

Temperature, T (°C), pH, DO (% saturation), and specific conductivity, SC (mS $cm^{-1}$), were monitored throughout the summer using a calibrated Hydrolab DS5 Water Quality Sonde (Hach Corporation, Loveland, CO, USA) placed inside a SAV canopy within the sampling area. The Hydrolab distance from the sediment-water interface was increased at each placement in an effort to monitor water chemistry above the anoxic zone. Daily precipitation, average daily air temperature, and solar radiation data were obtained online as monitored by the Villa Park weather station (station KMNROSEV4 located at N 45 ° 0 ' 4 ", W 93 ° 7 ' 20 ").

### *5.2.3 Laboratory analysis*

All water samples were filtered through a GF/F glass-fiber filter with a nominal pore size of 0.7 μm (Whatman, Kent, UK) within 4 hours of collection. A preliminary experiment verified that filtering within 6 hours of collection did not affect SRP concentrations (1-way ANOVA, $P > 0.3$, $n = 10$). Filtered samples were stored at 4 °C for less than 48 hours before chemical analysis. SRP was analyzed using the molybdate colormetric analysis technique with a spectrophotometer on duplicate samples.

Plant samples were returned to the lab where they were vigorously shaken for 3 minutes to remove the majority of the epiphytes (Zimba & Hopson 1997). Plant tissue and the filtrate from the sample rinse water were dried at 105 °C for 2 days, weighed, then ashed in a muffle furnace at 500 °C for 1 hour. The epiphyte dry weight per plant

dry weight, $DW_{epi}$ / $DW_{plant}$ (g $g^{-1}$), was determined for composites of 5 samples. The percent lost on ignition was also determined and compared.

### *5.2.4 Epiphyte removal rates*

To quantify the response of epiphyte removal rates to fluid flow conditions, a laboratory experiment was conducted in a closed, recirculating flow cell (2.2 cm diameter, 75 cm length). The flow cell was filled completely with water, and then the plant sample was placed into the cell by lowering the collection tube over the flow cell tube until the plant was submerged. This method resulted in minimal addition of water from the collection tube to the flow cell as well as minimal disruption of the epiphyte coverage. Since the plant segment was not held in a fixed location, a flow dispersing screen was placed behind the plant segment. For each flow rate, and each plant segment, the flow cell was operated for 15 minutes, after which, the plant was removed with tweezers and the water was collected and filtered using a GF/F filter. Flow rates were run in a random order. Fresh water was added as the cell was prepared for the next segment. 3 plant segments were run for each flow rate to give a composite result. After completing the 3 segments, the flow cell was run with water only to rinse out any material that may have attached to the walls. The plant segment was immersed in de-ionized water and shaken vigorously by hand to remove any remaining epiphytes. This water was also collected and filtered. The plants, the flow cell filtrate and the remaining epiphyte filtrate were dried at 105 °C for 2 days then weighed. All plant samples were used within 48 hours of collection from the field site. In the analysis, epiphyte

detachment was related to flow conditions using the Reynolds number, Re, a dimensionless ratio of the inertial and viscous forces where:

$$\mathrm{Re} = \frac{\mathrm{UL_{eff}}}{\nu} \qquad (5.1)$$

U (m $s^{-1}$) is the depth-averaged approaching velocity, $L_{eff}$ (m) is the ratio of plant volume to frontal area (for *E. canadensis*, $L_{eff}$ =0.089 cm (Hansen et al. 2011a)), and ν ($m^2$ $s^{-1}$) is the kinematic viscosity.

### *5.2.5 Treatment mechanism*

The repeated mechanical agitation of the canopy which was used to remove epiphytes also enhanced mixing. SAV productivity could be stimulated by either increased incident light at the plant surface or increased local mixing (Sanford & Crawford 2000). To determine whether improved light or mixing was driving the DO and SRP response to the treatment, a separate, 2-day experiment was conducted with two SAV canopies, side by side, 1 m apart. On the first day, water was sampled at a 10 cm depth within both canopies. One DO profile was measured in the undisturbed canopy. Both canopies then received the treatment and sampling was repeated. On the second day both canopies had increased light availability, due to epiphyte removal treatment from the previous day, but only one canopy had a second treatment immediately before sampling. On the second day, water was again collected at 10 cm depth and DO profiles were measured in both canopies before and after the single canopy treatment.

## 5.4 Results

### *5.3.1 Dissolved oxygen*

Time-averaged DO concentrations declined over the season with the anoxic region steadily shifting upward in the water column (Fig. 5.2).

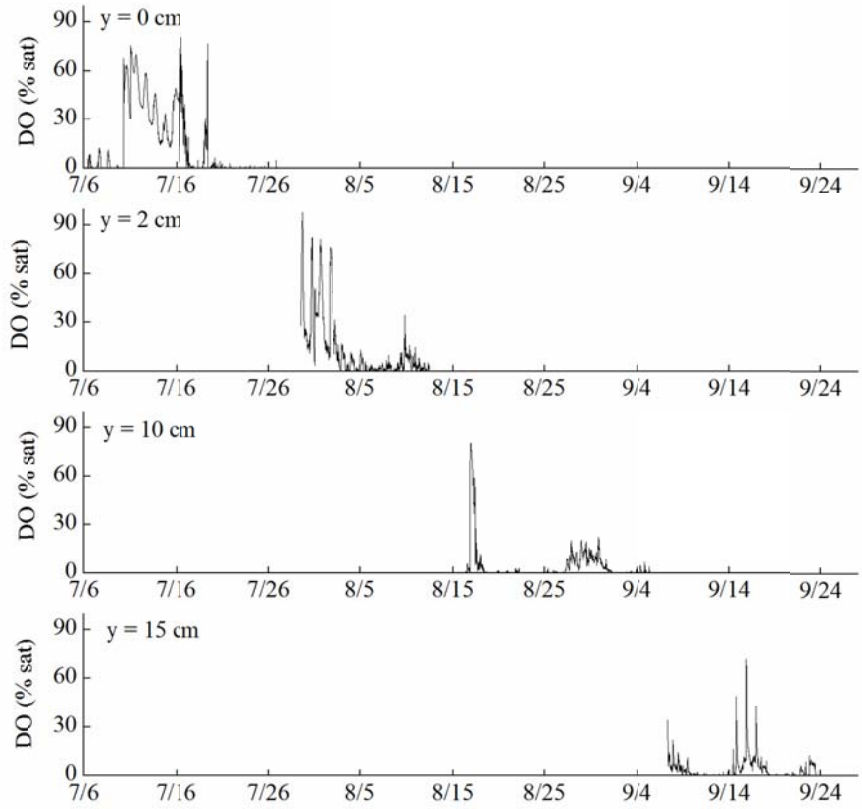


**Fig. 5.2** Dissolved oxygen measurements within SAV canopy throughout season. Each panel represents separate placement of the sensor at increasing distance from the sediment-water interface.

DO concentrations measured in both the undisturbed canopy and the canopy after epiphyte removal at the air-water interface, $DO_H$ (% sat), were proportional to incident solar radiation, S (W $m^{-2}$), based on a non-linear least squares regression where $DO_H$ =

$0.0027(S)^{1.64}$, $R^2 = 0.83$, $n = 12$ (Fig. 5.3). Early in the season, i.e. July 13, the SAV canopy height was approximately half the water depth. Because of this, DO at the air-water interface was not thought to be controlled by photosynthesis and these measurements were not included in the regression but are shown (Fig. 5.3).

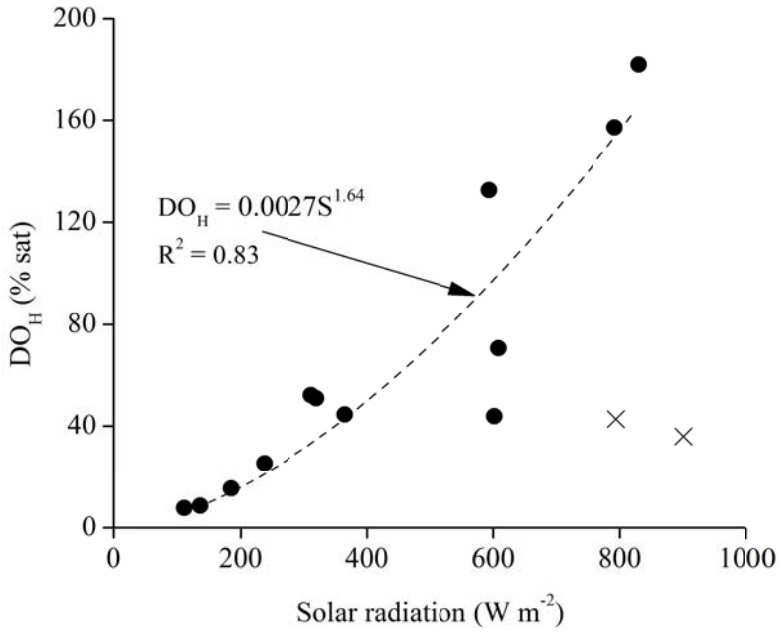


**Fig. 5.3** Dissolved oxygen at the air-water interface as function of solar radiation. Solid circles represent experimentally measured DO at the air-water interface within the SAV canopy. The two "X" symbols are data from July 13 which were not included in the least squares regression fit to the data.

To account for differences in solar radiative forcing, all DO measurements were normalized by $DO_H$. Average $DO_H$ during sampling ranged from 21% to 133% saturation (Table 5.1).

| Date | Solar radiation ($W\ m^{-2}$) | $T_{water}$ (°C) | pH | SC ($mS\ cm^{-1}$) | $DO_H$ (% sat) |
|---|---|---|---|---|---|
| 13-Jul | 847 | 22.6 | 7.1 | 12.8 | 42.8 |
| 27-Jul | 484 | 23.9 | 7.2 | 73.2 | 44.6 |
| 16-Aug | 712 | 21.5 | 7.2 | 16.6 | 132.6 |
| 7-Sep | 700 | 15.9 | 7.5 | 27.9 | 70.7 |
| 16-Sep | 320 | 11.4 | 7.6 | 32.9 | 51.0 |
| 17-Sep | 197 | 11.9 | 7.6 | 33.5 | 21.1 |

**Table 5.1.** Physical conditions during wetland sampling events. Measurements of solar radiation, water temperature, pH, specific conductivity and water surface DO concentration. Reported values are the average of measurements taken during the entire sampling event. $T_{water}$, pH and SC were measured at 15 minute intervals within a nearby SAV canopy. $DO_H$ represents the average of the two surface measurements (before and after epiphyte removal) during the sampling event.

For all sample dates, DO $(DO_H)^{-1}$ was lower after the treatment (open symbols) than before the treatment (closed symbols) throughout the profiles (Fig 5.4). For all sample events, the sediment-water interface was anoxic prior to treatment and the anoxic region extended into the water column (Fig. 5.4, dashed lines). For all experiments, the anoxic water zone disappeared after treatment.

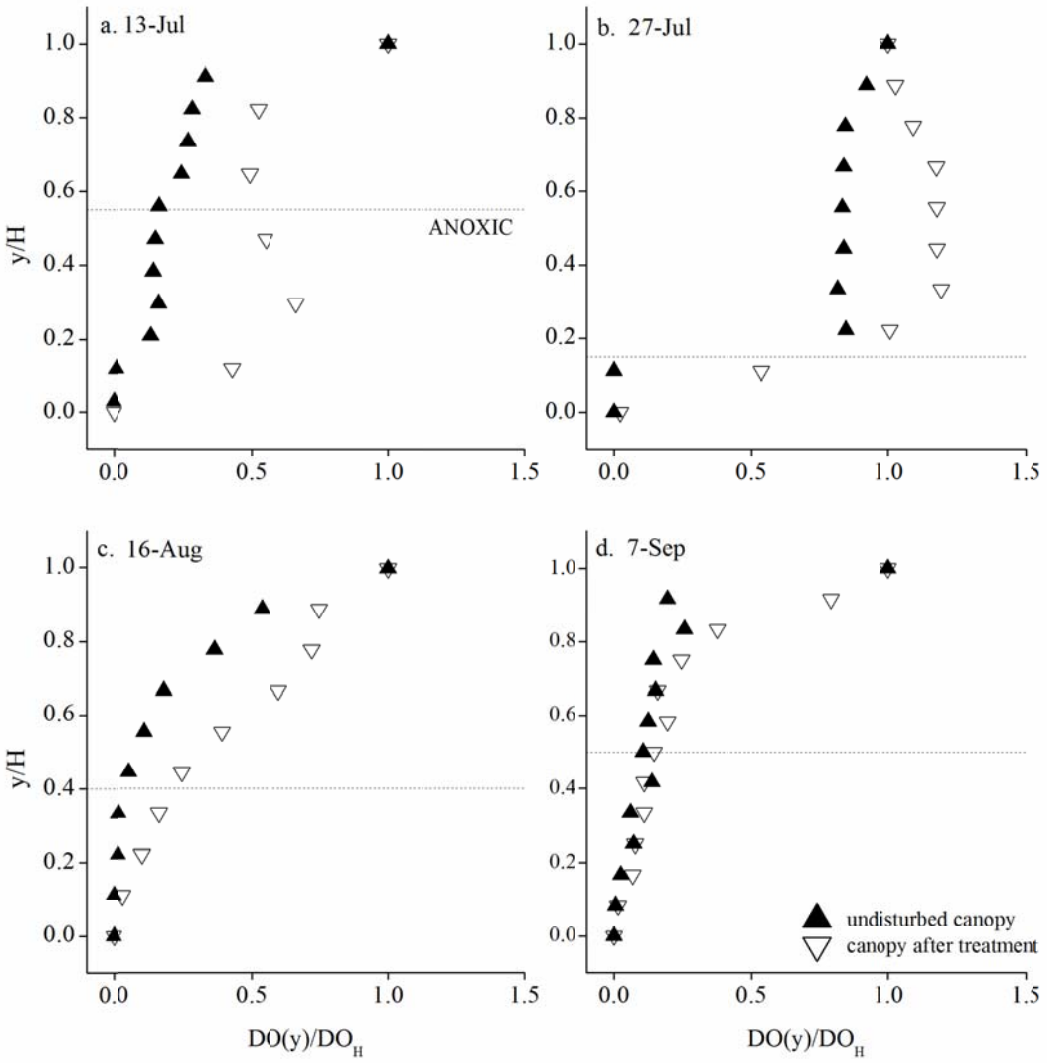


**Fig. 5.4** DO profiles within SAV canopy before and after epiphyte removal for 4 sampling events. Solid symbols represent measurements made in the undisturbed canopy and open symbols represent measurements in the same location following epiphyte removal and a brief settling period. The x-axis is measured DO normalized by the DO concentration at the air-water interface, $DO_H$. The y-axis is the distance from the sediment surface normalized by the water depth, H.

### *5.3.2 SRP concentrations*

SRP concentrations decreased through the water column after epiphyte removal, with the largest change seen early in the season (Fig. 5.5a). Near the sediment-water interface, SRP was smaller after epiphyte removal for all 4 sample dates. Further away from the sediment, SRP was significantly lower throughout the profile after epiphyte removal on July 13 (Fig. 5.5a). Data from July 27 (Fig. 5.5b), immediately following a precipitation event, fluctuated through the water column with no clear treatment effect. SRP concentrations on August 16 were lower after epiphyte removal (Fig. 5.5c). There was no discernible trend on Sept 7, when most measured concentrations were under 20 $\mu g\ L^{-1}$ (Fig. 5.5d). Comparing the 4 dates, there was a significant seasonal decline in undisturbed SAV canopy water SRP concentrations (Fig. 5.5).

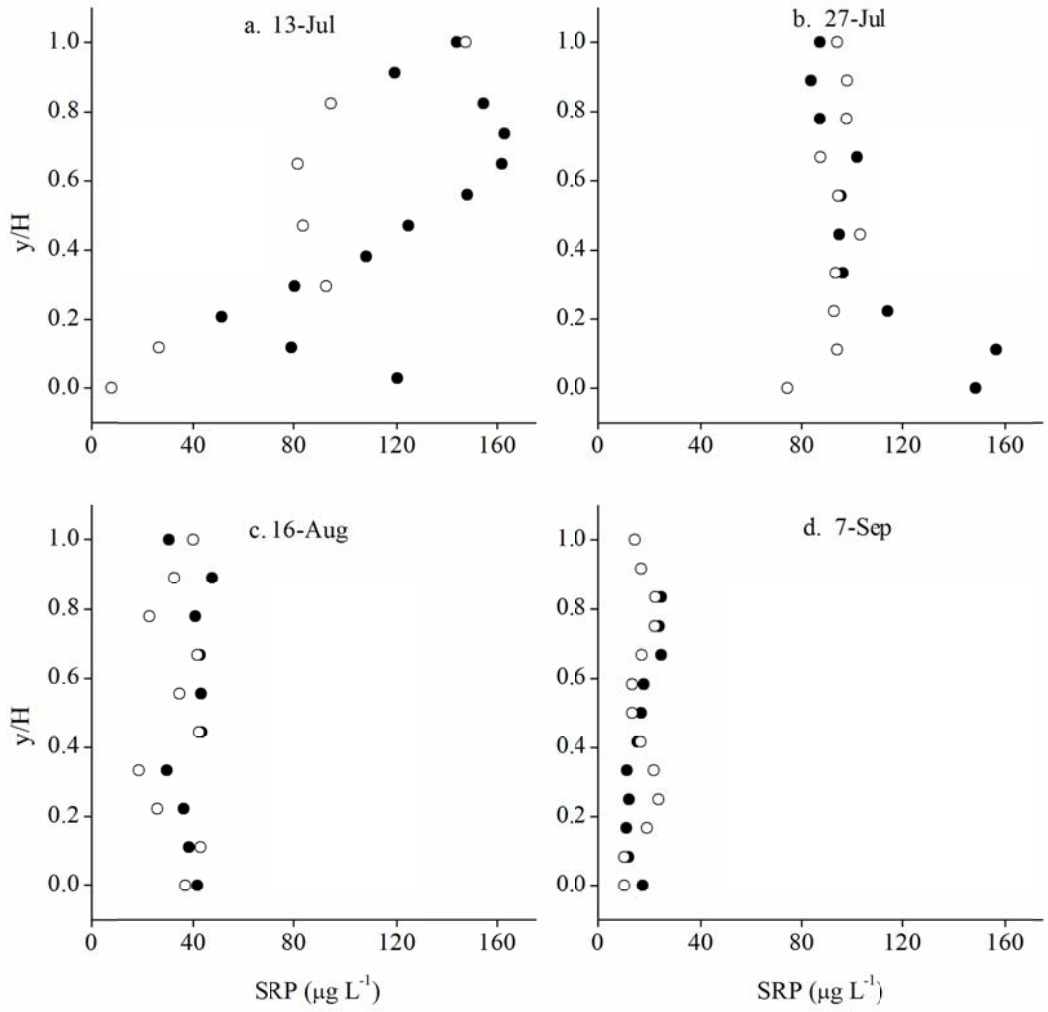


**Fig. 5.5** SRP profiles within the SAV canopy before and after epiphyte removal for 4 sampling events. Each symbol is the average of duplicate samples. Solid symbols represent measurements in the undisturbed canopy and open symbols represent measurements in the same location following epiphyte removal and a brief settling period. The y-axis is the distance from the sediment surface normalized by the water depth, H.

### *5.3.3 Treatment quantification and mechanism*

The mechanical agitation used to remove epiphytes in this study resulted in an average removal of 80% of loosely attached epiphytes (Table 5.2). For both the total

epiphytes and the epiphytes remaining after the treatment, approximately 25% of the biomass was volatile and 75% was non-volatile (Table 5.2). The undisturbed epiphyte biomass per plant biomass varied between 0.35 to 0.89 g $g^{-1}$ with no seasonal trend.

| Date | Undisturbed $DW_{epi}/DW_{plant}$ (g/g) | % epiphytes removed | undisturbed canopy % LOI | post treatment % LOI |
|---|---|---|---|---|
| 29-Jul | 0.89 | 80 | 26 | 31 |
| 16-Aug | 0.35 | 72 | 23 | 25 |
| 16-Sep | 0.52 | 86 | 29 | 28 |

**Table 5.2**. Treatment removal effect. Data included is epiphyte coverage in the undisturbed SAV canopy, $DW_{epi}\ DW_{plant}^{-1}$ (g $g^{-1}$), percent epiphytes removed by the treatment, and the percent biomass loss on ignition, LOI (g), for plant samples collected before and after treatment.

In the two-day experiment to determine the treatment mechanism, there was no significant difference in DO or SRP between the enhanced light canopy and the enhanced light + mixing canopy. $DO/DO_H$ was lower prior to epiphyte removal on the first day than any profiles from the second day (Fig. 5.6). One the second day, when only the light + mixing canopy received a second treatment, both canopies had higher $DO/DO_H$ in the first profile of the day (grey symbols) than in the second profile (open symbols).

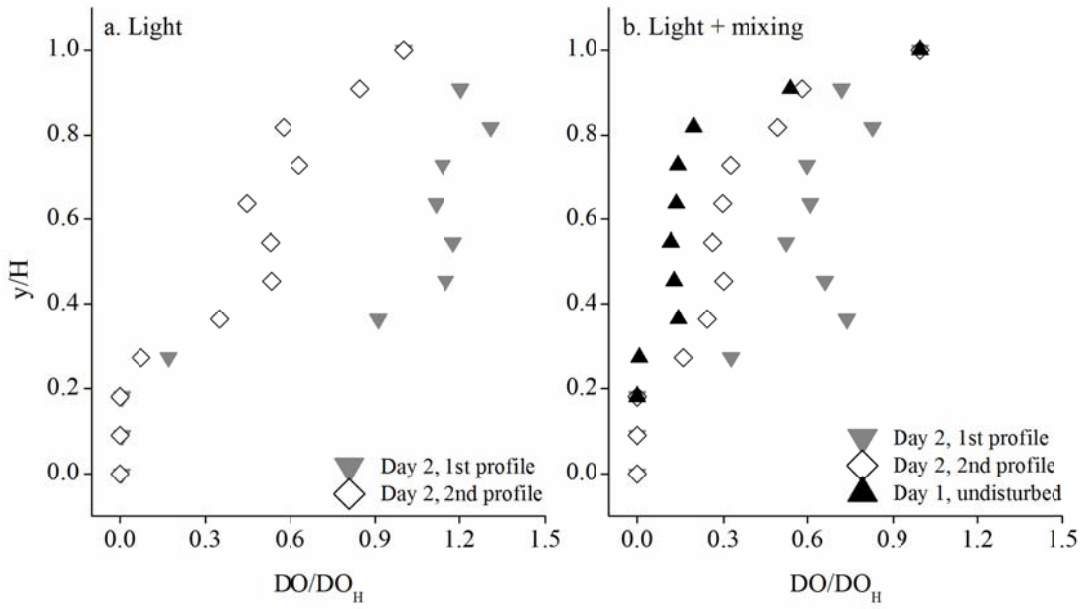


**Fig. 5.6** Vertical DO profiles from treatment mechanism study. One canopy received epiphyte removal treatment the first day only (light; panel a) and the other canopy received the treatment on both days (light + mixing; panel b). Profiles include; the undisturbed canopy (solid black symbols), the canopy on day two where epiphytes were removed the previous day (solid grey symbols) and the second profile of the second day (open symbols). The x-axis is measured DO normalized by the DO concentration at the air-water interface, $DO_H$. The y-axis is the distance from the sediment surface normalized by the water depth, H.

For both canopies, SRP was significantly lower the second day than the first, after epiphytes were removed from both canopies (Fig. 5.7). In the light + mixing canopy, the average SRP concentration in this canopy was lower after treatment although the difference was not significant (Fig. 5.7b). SRP levels showed no significant change between the two profiles on the second day in the canopy that did not receive a second treatment (Fig 5.7a).

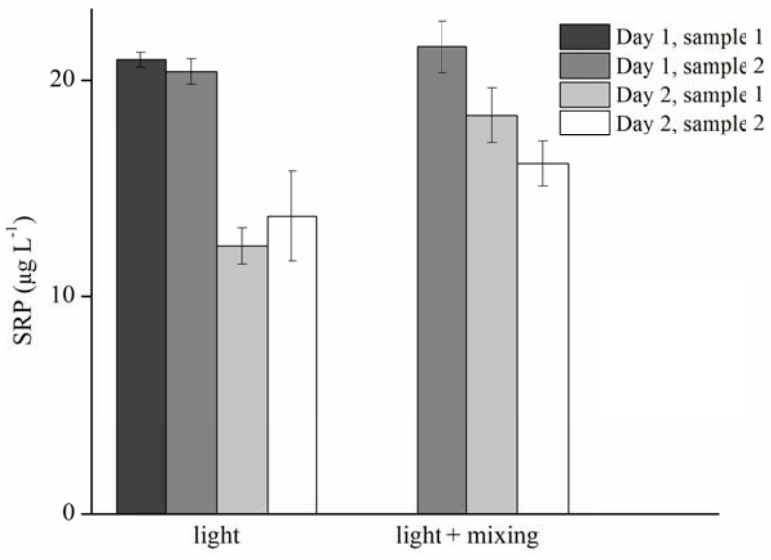


**Fig. 5.7** Average water SRP concentrations from treatment mechanism study. All samples were drawn at a depth of 10 cm from the air-water interface. Error bars represent one standard deviation ($n$ = 6).

### *5.3.4 Epiphyte removal rates*

Based on the laboratory flow cell experiment, epiphyte removal, $DW_{epi}\ (DW_{plant})^{-1}$ (g $g^{-1}$) appeared to be a linear function of Reynolds number, Re, where $Re = UL_{eff}\ \nu^{-1}$, for Re above 20 ($DW_{epi}\ (DW_{plant})^{-1} = 0.041Re + 0.04$, $r^2 = 0.99$, $n = 4$) (Fig. 5.8). Below the threshold Reynolds number of 20, epiphyte removal was independent of the fluid flow conditions.

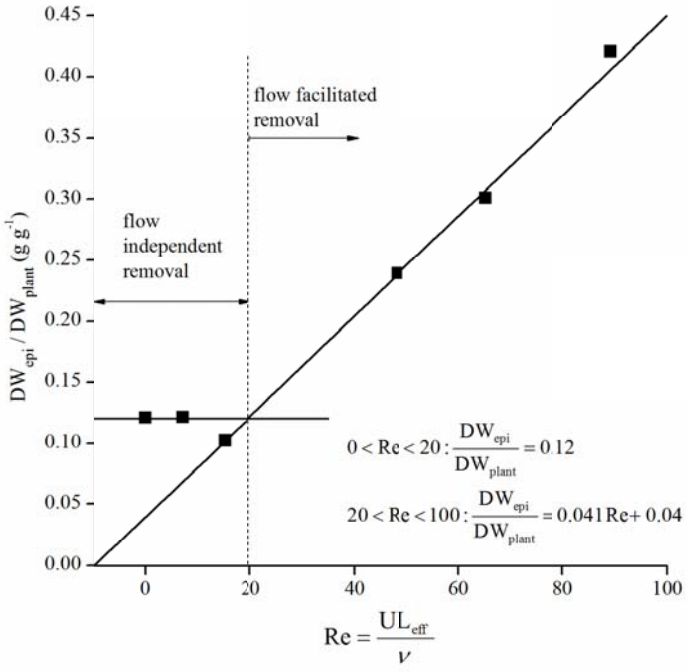


**Fig. 5.8** Relationship between epiphyte removal and Reynolds number as measured in a laboratory flow cell where $Re = UL_{eff}\nu^{-1}$. U is the depth averaged approaching velocity and $L_{eff}$ is the ratio of plant volume to frontal area for *E. canadensis*. The dashed diagonal line indicate a linear fits to data ($y = (0.041x + 0.04$; $r^2 = 0.99$, $n = 4$).

### *5.3.5 Environmental conditions*

Physical parameters measured over the season within a SAV canopy are reported in Table 5.1. Incident solar radiation, a function of cloud cover, varied dramatically across sample dates. Water temperature was between 12 to 24 °C and peaked in late July. pH was relatively neutral and constant with values between 7 and 7.6. Specific conductivity was only notable on 27 July, following a morning precipitation event. DO at the air-water interface was highest in mid-August; presumably when SAV biomass was also greatest.

## 5.5 Discussion

The results from this study indicate that epiphytes suppress SAV photosynthesis, decreasing overall water DO concentrations and increasing the thickness of the anoxic layer above the sediment-water interface. Early in the season, while SAV growth was rapid, epiphyte removal resulted in a measured decrease in SRP concentrations throughout much of the water column. SRP measurements in undisturbed canopies decreased through the season so, although SRP concentrations were always lower after epiphyte removal the change was more difficult to detect. Through a laboratory experiment we quantified epiphyte removal rates that could be obtained in practice with controlled flushing events. Together, these results show that epiphyte coverage altered SAV productivity and subsequent effect on wetland water chemistry, potentially decreasing the wetland effectiveness at capturing dissolved phosphorus.

### *5.4.1 Dissolved oxygen*

The results show that $DO/DO_H$ increased after epiphyte removal throughout the water column for all depths and on all sample dates (Fig 5.4), indicating that net photosynthesis was greater after epiphyte removal throughout the season; unlike Kohler et al. (2010) who reported a seasonal significance only. Solar radiation was a driving environmental variable that was accounted for by normalizing the DO profiles with the DO value at the air-water interface, $DO_H$. Because the treatment was subtractive the undisturbed canopy was always sampled earlier in the day when solar radiation tends to be lower than the treated canopy. Some measurements of $DO_H$ were above 100 % saturation (Table 5.1), indicating that water DO concentrations were strongly influenced

by active photosynthetic pumping of oxygen and not just diffusion through the air-water interface. Oxic conditions near the sediment-water interface were established after epiphyte removal; a condition that is important for controlling P solubility in both the sediment and the suspended particles (e.g. Kalff 2005).

### *5.4.2 SRP concentrations*

SRP concentrations decreased after epiphyte removal with the most notable changes measured early in the season when plant growth rates tend to be highest (Reddy et al. 1999). SRP concentrations decreased close to the sediment-water interface for all sample dates (Fig 5.6). Late in the season, SRP concentrations in the canopy were low enough that changes in the concentration were minimal and within measurement error. Based on the large SRP decrease measured 24 hours after treatment in the treatment mechanism study, it is probable that the experimental protocol did not capture the full impact of epiphyte removal on SRP concentrations within the canopy. In the 2-day experiment, there was a large decrease in SRP after 24 hours in both profiles, although, no significant change was captured on the samples taken immediately after treatment (Fig. 5.7), consistent with sample profiles (Fig. 5.4). Differences in solar radiation were not accounted for in interpreting the SRP data as no correlation between S and SRP was seen. It is not known if SAV switched partitioning of P source to a greater reliance on water column SRP, now that the resistance to shoot uptake had decreased, or if total P uptake had increased. Both changes represent enhanced SAV functioning towards the CW goal of reduced P output, whether source is incoming stormwater or SAV root mining of sediment P pool.

SRP concentrations decreased as the season progressed, reaching a minimum of approximately 20 $\mu$g $L^{-1}$ by 7, September (Fig. 5.5). Although visual observation of the SAV indicated that *E. canadensis* and *C. demersum* were starting to senesce, water SRP concentrations did not rise as was expected. It is possible that a community shift was delaying the seasonal P release. Two changes in the canopy assemblage were observed although not quantified. First, the epiphytic filamentous algae population within the canopy became much more abundant. Second, the population of *L. minor,* which had been minimal through the season, exploded until it completely covered the water surface throughout the wetland (Fig. 5.1c). The dense water surface coverage by *L. minor* decreased the light available to the submerged plants, accelerating SAV decline and possibly causing increased release of SRP from the senescing tissue into the water column where *L. minor* and the filamentous algae could access it (Parr et al. 2002).

### *5.4.3 Treatment mechanism*

In the treatment mechanism study, the largest changes in DO and SRP were measured after epiphyte removal for both canopies (Figs. 5.6 & 5.7). There was no significant difference in either SRP or DO profiles on the second day after one canopy received an additional treatment, indicating that mixing was not the mechanism responsible for the measured changes in profiles taken throughout this study. Based on these results, we conclude that increased light availability was the cause of the increased DO and decreased SRP after treatment.

### *5.4.4 Effect of flow on epiphyte removal rates*

There appeared to be a minimum velocity threshold below which, epiphytes are stably attached to host and above which, the rate of epiphyte removal is flow dependent (Fig. 5.8). After surpassing this threshold, epiphyte removal rates were linear within the tested velocity range. This trend should have a maximum velocity limit that is determined by the load carrying capacity of the leaves and stem. This analysis provides a solid basis supporting uni-directional flushing events in a constructed wetland to control epiphyte load. Although a similar trend is expected in a system with baseflow, such as a stream, the epiphytes would be expected to be more strongly attached and the corresponding Re to detach them would also be larger than what was measured from the wetland samples.

Removing epiphytes from a SAV canopy resulted in an increase in DO and a decrease in SRP throughout the depth of the canopy with the largest changes seen early in the season. These results show that the impact of a heavy epiphyte load extends throughout the depth of the water column with serious implications for P solubility at the sediment-water interface. In a nutrient rich light poor environment such as constructed wetlands, the light limitation due to epiphyte coverage decreases SAV photosynthetic rates and thus the capacity of SAV to alter P. The laboratory results showed that epiphyte detachment rates were linearly proportional to flow conditions within the tested velocity range and provide a mechanistic starting point for management for epiphyte removal. In practice, epiphyte coverage could be controlled through periodic increases in baseflow, through increasing grazer populations or through enhanced bioturbation levels.

Active epiphyte control could improve the ability of the SAV canopy to meet the constructed wetland design objective of removing P from the water column.

# Bibliography


Arnold KE and Manley SL (1985) Carbon allocation in *Macrocystis pyrifera* (Phaeophyta): Intrinsic variability in photosynthesis and respiration. J Phycol 21:154-167

Asaeda T, Sultana M, Manatunge J, Fujino T (2004) The effect of epiphytic algae on the growth and production of *Potamogeton perfoliatus L*. in two light conditions. Environ Exp Bot 52:225-238

Azcue J and A Mudroch (1994) Comparison of different washing, ashing, and digestion methods for the analysis of trace-elements in vegetation. International Journal of Environmental Analytical Chemistry 57: 151-162.

Baldy V, M Tremolieres, M Andrieu and J Belliard (2007) Changes in phosphorus content of two aquatic macrophytes according to water velocity, trophic status and time period in hardwater streams. Hydrobiologia 575: 343-351.

Bird RB, Stewart WE, Lightfoot EN (2002) Transport phenomena, 2nd edn. John Wiley and Sons, Inc., New York

Borchart MA (1996) Nutrients in: Algal Ecology, Stevenson RJ, Bothwell ML and Lowe RL (eds) Algal Ecology. Academic Press, Inc., San Diego, CA, p. 183

Bosak T, Bush JWM, Flynn MR, Liang B, Ono S, Petroff AP, Sim MS (2010) Formation and stability of oxygen-rich bubbles that shape photosynthetic mats. Geobiology 8:45-55

Brooks RR, J Lee, RD Reeves and T Jaffre (1977) Detection of nickeliferous rocks by analysis of herbarium specimens of indicator plants. Journal of Geochemical Exploration 7: 49-57.

Burmeister LC (1993) Convective heat transfer, 2nd edn. John Wiley and Sons, Inc., New York

Carignan R and Kalff J (1982) Phosphorus release by submerged macrophytes: Significance to epiphyton and phytoplankton. Limnol Oceanogr 27:pp. 419-427

Carollo F, Ferro V, Termini D (2002) Flow velocity measurements in vegetated channels. Journal of Hydraulic Engineering-ASCE 128:664-673

Carpenter S and Lodge D (1986) Effects of submersed macrophytes on ecosystem processes. Aquat Bot 26:341-370

Chen C, D Huang and J Liu (2009) Functions and toxicity of nickel in plants: Recent advances and future prospects. Clean – Soil, Air, Water 37: 304-313.

Chimney MJ, Wenkert L, Pietro KC (2006) Patterns of vertical stratification in a subtropical constructed wetland in south florida (USA). Ecol Eng 27:322-330

Colombo-Pallotta MF, Garcia-Mendoza E, Ladah LB (2006) Photosynthetic performance, light absorption, and pigment composition of *Macrocystis pyrifera* (Laminariales, Phaeophyceae) blades from different depths. J Phycol 42:1225-1234

Cornelisen CD and FIM Thomas (2002) Ammonium uptake by seagrass epiphytes: Isolation of the effects of water velocity using an isotope label. Limnology and Oceanography 47: 1223-1229.

Cornelisen CD and FIM Thomas (2006) Water flow enhances ammonium and nitrate uptake in a seagrass community. Marine Ecology Progress Series 312: 1-13.

Cornelisen CD and Thomas FIM (2009) Prediction and validation of flow dependent uptake of ammonium over a seagrass hardbottom community in Florida bay. Mar Ecol Prog Ser 386:71-81

Cussler EL (1984) Diffusion: Mass transfer in fluid systems, Cambridge University Press, New York

Dade W (1993) Near-bed turbulence and hydrodynamic control of diffusional mass-transfer at the sea-floor. Limnol Oceanogr 38:52-69

Dayton PK (1985) Ecology of kelp communities. Annu Rev Ecol Syst 16:215-245

Denny M and Roberson L (2002) Blade motion and nutrient flux to the kelp, *Eisenia arborea*. Biol Bull 203:1-13

Dhir B, P Sharmila and PP Saradhi (2009) Potential of aquatic macrophytes for removing contaminants from the environment. Critical Reviews in Environmental Science and Technology 39: 754-781.

Dodds W (1991) Community interactions between the filamentous alga *Cladophora glomerata (L)* Kuetzing, its epiphytes, and epiphyte grazers. Oecologia 85:572-580

Dodds W and Biggs B (2002) Water velocity attenuation by stream periphyton and macrophytes in relation to growth form and architecture. J N Am Benthol Soc 21:2-15

Dodds WK and Gudder DA (1992) The ecology of *Cladophora*. J Phycol 28:415-427

Drake L, Dobbs F, Zimmerman R (2003) Effects of epiphyte load on optical properties and photosynthetic potential of the seagrasses *Thalassia testudinum* Banks ex *Konig* and *Zostera marina L*. Limnol Oceanogr 48:456-463

Edwards MS and Kim KY (2010) Diurnal variation in relative photosynthetic performance in

giant kelp *Macrocystis pyrifera* (Phaeophyceae, Laminariales) at different depths as estimated using PAM fluorometry. Aquat Bot 92:119-128

Enriquez S and Rodriguez-Roman A (2006) Effect of water flow on the photosynthesis of three marine macrophytes from a fringing reef lagoon. Mar Ecol Prog Ser 323:119-132

Escartin J and Aubrey D (1995) Flow structure and dispersion within algal mats. 3344-2008. Estuarine Coastal and Shelf Science 40:451-472

Eugelink A (1998) Phosphorus uptake and active growth of *Elodea canadensis Michx*. and *Elodea nuttallii (Planch.) St. John*. Water Science and Technology 37:59-65

Falter JL, Atkinson MJ, Merrifield MA (2004) Mass transfer limitation of nutrient uptake by a wave dominated reef flat community. Limnol Oceanogr 49:1820-1831

Fram JP, Stewart HL, Brzezinski MA, Gaylord B, Reed DC, Williams SL, MacIntyre S (2008) Physical pathways and utilization of nitrate supply to the giant kelp, *Macrocystis pyrifera*. Limnol Oceanogr 53:1589-1603

Fritioff A and M Greger (2003) Aquatic and terrestrial plant species with potential to remove heavy metals from stormwater. International Journal of Phytoremediation 5: 211-224.

Fritioff A, L Kautsky and M Greger (2005) Influence of temperature and salinity on heavy metal uptake by submersed plants. Environmental Pollution 133: 265-274.

Gaylord B, Reed DC, Washburn L, Raimondi PT (2004) Physical-biological coupling in spore dispersal of kelp forest macroalgae. J Mar Syst 49:19-39

Gaylord B, Rosman JH, Reed DC, Koseff JR, Fram J, MacIntyre S, Arkema K, McDonald C, Brzezinski MA, Largier JL, and others (2007) Spatial patterns of flow and their modification within and around a giant kelp forest. Limnol Oceanogr 52:1838-1852

Gerard VA (1982) *In situ* water motion and nutrient-uptake by the giant kelp *Macrocystis pyrifera*. Mar Biol 69:51-54

Gerard VA (1986) Photosynthetic characteristics of giant kelp (*Macrocystis pyrifera*) determined *in situ*. Mar Biol 90:473-482

Ghisalberti M and Nepf H (2006) The structure of the shear layer in flows over rigid and flexible canopies. Environmental Fluid Mechanics 6:277-301

Ghisalberti M and Nepf HM (2002) Mixing layers and coherent structures in vegetated aquatic flows. Journal of Geophysical Research-Oceans 107:3011

Gonen Y, Kimmel E, Friedlander M (1993) Effect of relative water motion on photosynthetic

rate of red alga *Gracilaria conferta*. Hydrobiologia 261:493-498

Gosselain V, C Hudon, A Cattaneo, P Gagnon, D Planas and D Rochefort (2005) Physical variables driving epiphytic algal biomass in a dense macrophyte bed of the St. Lawrence River (Quebec, Canada). Hydrobiologia 534: 10-22.

Graham MH, Vasquez JA, Buschmann AH (2007) Global ecology of the giant kelp *Macrocystis*: From ecotypes to ecosystems. Oceanography and Marine Biology, 45:39-88

Gross EM, C Feldbaum and A Graf (2003) Epiphyte biomass and elemental composition on submersed macrophytes in shallow eutrophic lakes. Hydrobiologia 506: 559-565.

Haferburg G and E Kothe (2007) Microbes and metals: interactions in the environment. Journal of Basic Microbiology 47: 453-467.

Hansen AT, Stark RA, Hondzo M (2011) Uptake of dissolved nickel by *Elodea canadensis* and epiphytes influenced by fluid flow conditions. Hydrobiologia 658:127-138

Hansen AT, Hondzo M, Hurd CL (2011) Photosynthetic oxygen flux by *Macrocystis pyrifera*: A mass transfer model with experimental validation. Marine Ecology-Progress Series 434:45-55

Harting J, Kunert C, Hyvaluoma J (2010) Lattice Boltzmann simulations in microfluidics: Probing the no-slip boundary condition in hydrophobic, rough, and surface nanobubble laden microchannels RID B-4884-2008. Microfluidics and Nanofluidics 8:1-10

Hepburn CD and Hurd CL (2005) Conditional mutualism between the giant kelp *Macrocystis pyrifera* and colonial epifauna. Mar Ecol Prog Ser 302:37-48

Hepburn CD, Holborow JD, Wing SR, Frew RD, Hurd CL (2007) Exposure to waves enhances the growth rate and nitrogen status of the giant kelp *Macrocystis pyrifera*. Mar Ecol Prog Ser 339:99-108

Higgins SN, Malkin SY, Howell ET, Guildford SJ, Campbell L, Hiriart-Baer V, Hecky RE (2008) An ecological review of *Cladophora glomerata (Chlorophyta*) in the Laurentian Great Lakes. J Phycol 44:839-854

Hondzo M, Feyaerts T, Donovan R, O'Connor BL (2005) Universal scaling of dissolved oxygen distribution at the sediment-water interface: A power law. Limnol Oceanogr 50:1667-1676

Hudson RJM (1998) Which aqueous species control the rates of trace metal uptake by aquatic biota? Observations and predictions of non-equilibrium effects. Science of the Total Environment 219: 95-115.

Hurd CL (2000) Water motion, marine macroalgal physiology, and production. J Phycol

36:453-472

Hurd CL and Pilditch CA (2011) Flow induced morphological variations affect boundary-layer thickness of *Macrocystis pyrifera* (Heterokontophyta, Laminariales). J Phycol 47:

Hurd CL and Stevens CL (1997) Flow visualization around single and multiple bladed seaweeds with various morphologies. J Phycol 33:360-367

Hurd CL, Harrison PJ, Druehl LD (1996) Effect of seawater velocity on inorganic nitrogen uptake by morphologically distinct forms of *Macrocystis integrifolia* from wave-sheltered and exposed sites. Mar Biol 126:205-214

Hurd CL, PJ Harrison and LD Druehl (1996) Effect of seawater velocity on inorganic nitrogen uptake by morphologically distinct forms of Macrocystis integrifolia from wave-sheltered and exposed sites. Marine Biology 126: 205-214.

Hurd CL, Quick M, Stevens CL, Laval BE, Harrison PJ, Druehl LD (1994) A low volume flow tank for measuring nutrient uptake by large macrophytes. J Phycol 30:892-896

Ikeda S and Kanazawa M (1996) Three-dimensional organized vortices above flexible water plants. Journal of Hydraulic Engineering-Asce 122:634-640

Ishii S, Yan T, Shively DA, Byappanahalli MN, Whitman RL, Sadowsky MJ (2006) *Cladophora (chlorophyta) spp.* harbor human bacterial pathogens in nearshore water of Lake Michigan. Appl Environ Microbiol 72:4545-4553

Jackson GA (1977) Nutrients and production of giant kelp, *Macrocystis pyrifera*, off southern California. Limnol Oceanogr 22:979-995

Kahkonen MA and PKG. Manninen (1998) The uptake of nickel and chromium from water by Elodea canadensis at different nickel and chromium exposure levels. Chemosphere 36: 1381-1390.

Kaj S (1977) Effect of epiphytes on eelgrass photosynthesis. Aquat Bot 3:55-63

Kalff J (2002) Limnology. Prentice Hall, New Jersey

Kays WM, ME Crawford and B Weigand (2005) Convective Heat and Mass Transfer. 4th ed. McGraw-Hill, New York.

Kljakovic-Gaspic Z, BAntolic, T. Zvonaric and A. Baric, 2004. Distribution of cadmium and lead in Posidonia oceanica (L.) delile from the middle Adriatic sea. Fresenius Environmental Bulletin 13: 1210-1215.

Koch EW (1994) Hydrodynamics, diffusion boundary layers and photosynthesis of the

seagrasses *Thalassia testudinum* and *Cymodocea nodosa*. Mar Biol 118:767-776

Koehler J, Hachol J, Hilt S (2010) Regulation of submersed macrophyte biomass in a temperate lowland river: Interactions between shading by bank vegetation, epiphyton and water turbidity RID C-4783-2011. Aquat Bot 92:129-136

Lakatos G, M Kiss and I Meszaros (1999) Heavy metal content of common reed (Phragmites australis/Cav./Trin. ex Steudel) and its periphyton in Hungarian shallow standing waters. Hydrobiologia 415: 47-53.

Larned ST, Nikora VI, Biggs BJF (2004) Mass-transfer-limited nitrogen and phosphorus uptake by stream periphyton: A conceptual model and experimental evidence. Limnol Oceanogr 49:1992-2000

Laufer J (1951) Investigation of turbulent flow in a two-dimensional channel. National Advisory Committee for Aeronautics Report 1053: 10-14.

Levich VG (1962) Physiochemical hydrodynamics. Prentice-Hall, Englewood Cliffs, NJ

Longstaff BJ, Kildea T, Runcie JW, Cheshire A, Dennison WC, Hurd C, Kana T, Raven JA, Larkum AWD (2002) An *in situ* study of photosynthetic oxygen exchange and electron transport rate in the marine macroalga *Ulva lactuca* (Chlorophyta). Photosynthesis Res 74:281-293

Losee, RF and RG Wetzel (1993) Littoral flow-rates within and around submersed macrophyte communities. Freshwater Biology 29: 7-17.

Losic D, Mitchell JG, Voelcker NH (2009) Diatomaceous lessons in nanotechnology and advanced materials RID B-2436-2009. Adv Mater 21:2947-2958

Lowe RL, Rosen BH, Kingston JC (1982) A comparison of epiphytes on *Bangia atropurpurea (Rhodophyta)* and *Cladophora glomerata (Chlorophyta)* from northern Lake Michigan. J Great Lakes Res 8:164-168

Maberly SC (1990) Exogenous sources of inorganic carbon for photosynthesis by marine macroalgae. J Phycol 26:439-449

Madsen J, Chambers P, James W, Koch E, Westlake D (2001) The interaction between water movement, sediment dynamics and submersed macrophytes. Hydrobiologia 444:71-84

Madsen TV and Cedergreen N (2002) Sources of nutrients to rooted submerged macrophytes growing in a nutrient-rich stream. Freshwat Biol 47:283-291

Madsen TV and E Warncke (1983) Velocities of currents around and within submerged aquatic vegetation. Archiv Für Hydrobiologie 97: 389-394.

Maleva MG, GF Nekrasova, P Malec, MNV Prasad and K Strzalka (2009) Ecophysiological tolerance of Elodea canadensis to nickel exposure. Chemosphere 77: 392-398.

Marks JC and Power ME (2001) Nutrient induced changes in the species composition of epiphytes on *Cladophora glomerata kutz. (Chlorophyta).* Hydrobiologia 450:187-196

Mass T, Genin A, Shavit U, Grinstein M, Tchernov D (2010) Flow enhances photosynthesis in marine benthic autotrophs by increasing the efflux of oxygen from the organism to the water. Proc Natl Acad Sci U S A 107:2527-2531

Maxwell K and Johnson GN (2000) Chlorophyll fluorescence - a practical guide. J Exp Bot 51:659-668

May R (1977) Thresholds and breakpoints in ecosystems with a multiplicity of stable states. Nature 269:471-477

Miller HL and Dunton KH (2007) Stable isotope (C-13) and O-2 micro-optode alternatives for measuring photosynthesis in seaweeds. Mar Ecol Prog Ser 329:85-97

Mortimer DC (1985) Fresh-water aquatic macrophytes as heavy-metal monitors - the Ottawa River experience. Environmental Monitoring and Assessment 5: 311-323.

Nepf H and Ghisalberti M (2008) Flow and transport in channels with submerged vegetation RID C-6202-2008. Acta Geophysica 56:753-777

Neto C, Evans DR, Bonaccurso E, Butt HJ, Craig VSJ (2005) Boundary slip in Newtonian liquids: A review of experimental studies. Reports on Progress in Physics 68:2859-2897

Nezu I and Rodi W (1986) Open-channel flow measurements with a laser Doppler anemometer. Journal of Hydraulic Engineering-Asce 112:335-355

Nishihara GN and Ackerman JD (2006) The effect of hydrodynamics on the mass transfer of dissolved inorganic carbon to the freshwater macrophyte *Vallisneria americana.* Limnol Oceanogr 51:2734-2745

Nishihara GN and Ackerman JD (2007) On the determination of mass transfer in a concentration boundary layer. Limnol Oceanogr -Methods 5:88-96

Pal R (2007) Steady laminar flow of non-Newtonian bubbly suspensions in pipes. J Non Newtonian Fluid Mech 147:129-137

Parr L, Perkins R, Mason C (2002) Reduction in photosynthetic efficiency of *Cladophora glomerata,* induced by overlying canopies of *Lemna spp*. Water Res 36:1735-1742

Pelton DK, Levine SN, Braner M (1998) Measurements of phosphorus uptake by macrophytes and epiphytes from the LaPlatte river (VT) using P-32 in stream microcosms. Freshwat

Biol 39:285-299

Plew DR, Cooper GG, Callaghan FM (2008) Turbulence-induced forces in a freshwater macrophyte canopy. Water Resour Res 44:W02414

Pokorny J, Kvet J, Ondok J, Toul Z, Ostry I (1984) Production ecological analysis of a plant community dominated by *Elodea canadensis Michx*. Aquat Bot 19:263-292

Power M, Lowe R, Furey P, Welter J, Limm M, Finlay J, Bode C, Chang S, Goodrich M, Sculley J (2009) Algal mats and insect emergence in rivers under Mediterranean climates: Towards photogrammetric surveillance. Freshwat Biol 54:2101-2115

Rai, PK (2009) Heavy metal phytoremediation from aquatic ecosystems with special reference to macrophytes. Critical Reviews in Environmental Science and Technology 39: 697-753.

Raupach MR, Finnigan JJ, Brunet Y (1996) Coherent eddies and turbulence in vegetation canopies: The mixing-layer analogy. Bound -Layer Meteorol 78:351-382

Reddy K, Kadlec R, Flaig E, Gale P (1999) Phosphorus retention in streams and wetlands: A review. Crit Rev Environ Sci Technol 29:83-146

Reed DC, Rassweiler A, Arkema KK (2008) Biomass rather than growth rate determines variation in net primary production by giant kelp. Ecology 89:2493-2505

Rosman JH, Koseff JR, Monismith SG, Grover J (2007) A field investigation into the effects of a kelp forest (*Macrocystis pyrifera*) on coastal hydrodynamics and transport. Journal of Geophysical Research-Oceans 112:C02016

Samecka-Cymerman, A and AJ Kempers (2003) Biomonitoring of water pollution with Elodea canadensis. A case study of three small Polish rivers with different levels of pollution. Water Air and Soil Pollution 145: 139-153.

Sand-Jensen K (1977) Effect of epiphytes on eelgrass photosynthesis. Aquatic Botany 3:55-63

Sand-Jensen K, Binzer T, Middelboe AL (2007) Scaling of photosynthetic production of aquatic macrophytes - a review. Oikos 116:280-294

Sand-Jensen K, Revsbech NP, Jorgensen BB (1985) Microprofiles of oxygen in epiphyte communities on submerged macrophytes. Mar Biol 89:55-62

Sand-Jensen, K and O Pedersen (1999) Velocity gradients and turbulence around macrophyte stands in streams. Freshwater Biology 42: 315-328.

Sanford LP and Crawford SM (2000) Mass transfer versus kinetic control of uptake across solid-water boundaries. Limnol Oceanogr 45:1180-1186

Sato, H, M Yui and H Yoshikawa (1996) Ionic diffusion coefficient of Cs+, Pb2+, Sm3+, Ni2+, SeO42- and TcO4- in free water determined from conductivity measurements. Journal of Nuclear Science and Technology 33: 950-955.

Schlacher-Hoenlinger, MA and TA Schlacher (1998) Accumulation, contamination, and seasonal variability of trace metals in the coastal zone - patterns in a seagrass meadow from the Mediterranean. Marine Biology 131: 401-410.

Schlichting H (1979) Boundary-layer theory, 7th edn. McGraw-Hill, Inc., New York

Shaughnessy EJ, Katz IM, Schaffer JP (2005) Introduction to fluid mechanics. Oxford University Press, New York, NY

Sheng J, Malkiel E, Katz J (2006) Digital holographic microscope for measuring three-dimensional particle distributions and motions RID A-7624-2010. Appl Opt 45:3893-3901

Steinberger N and Hondzo M (1999) Diffusional mass transfer at sediment-water interface. Journal of Environmental Engineering-Asce 125:192-200

Steneck RS, Graham MH, Bourque BJ, Corbett D, Erlandson JM, Estes JA, Tegner MJ (2002) Kelp forest ecosystems: Biodiversity, stability, resilience and future. Environ Conserv 29:436-459

Stevens CL, Hurd CL, Isachsen PE (2003) Modelling of diffusion boundary layers in subtidal macroalgal canopies: The response to waves and currents. Aquat Sci 65:81-91

Stewart HL, Fram JP, Reed DC, Williams SL, Brzezinski MA, MacIntyre S, Gaylord B (2009) Differences in growth, morphology and tissue carbon and nitrogen of *Macrocystis pyrifera* within and at the outer edge of a giant kelp forest in California, USA. Marine Ecology-Progress Series 375:101-112

Thiebaut G and Muller S (2003) Linking phosphorus pools of water, sediment and macrophytes in running waters. Annales De Limnologie-International Journal of Limnology 39:307-316

Thomas, FIM and MJ Atkinson (1997) Ammonium uptake by coral reefs: Effects of water velocity and surface roughness on mass transfer. Limnology and Oceanography 42: 81-88.

UN Educ. Sci. Cult. Organ. (UNESCO) (2009) The United Nations World Water Development Report 3: Water in a Changing World. Paris/New York: UNESCO/Berghahn Books

UN Enviro. Prog. Global Enviro. Monitoring Sys. (UNEP/GEMS) (2007) Water quality outlook. ISBN 95039-11-4

Valukina NV and Kashinskii ON (1979) Investigation of the friction stress on a wall in a monodispensed gas-liquid flow. Journal of Applied Mechanics and Technical Physics

20:69-73

Vanden Heuvel A, McDermott C, Pillsbury R, Sandrin T, Kinzelman J, Ferguson J, Sadowsky M, Byappanahalli M, Whitman R, Kleinheinz GT (XXXX) The green alga, *Cladophora*, promotes growth and contamination of recreational waters in Lake Michigan. J Environ Qual :333

Weis, JS and P Weis (2004) Metal uptake, transport and release by wetland plants: implications for phytoremediation and restoration. Environment international 30: 685-700.

Wenck Associates Inc. for Capitol Region Watershed District (2009) Villa Park Wetland Management Plan. Wenck File #1486-14

Wereley ST and Meinhart CD (2010) Recent advances in micro-particle image velocimetry. Annu Rev Fluid Mech 42:557-576

Wetzel RG (2001) Limnology, lakes and river ecosystems, 3rd Edition. Academic Press, San Diego, California

Wheeler WN (1980) Effect of boundary-layer transport on the fixation of carbon by the giant kelp *Macrocystis pyrifera*. Mar Biol 56:103-110

Whitman RL, Shively DA, Pawlik H, Nevers MB, Byappanahalli MN (2003) Occurrence of *Escherichia coli* and *Enterococci* in *Cladophora (Chlorophyta*) in nearshore water and beach sand of Lake Michigan. Appl Environ Microbiol 69:4714-4719

Wilson, NR and RH Shaw (1977) Higher-order closure model for canopy flow. Journal of Applied Meteorology 16: 1197-1205.

Zhang, YS, ZY Zhang, K Suzuki and T Maekawa (2003) Uptake and mass balance of trace metals for methane producing bacteria. Biomass and Bioenergy 25: 427-433.

Zheljazkov, VD and P McNeil (2008) Comparison of five digestion procedures for recovery of nutrients and trace elements in plant tissue. Journal of Plant Nutrition 31: 1937-1946.

Zimba PV and Hopson MS (1997) Quantification of epiphyte removal efficiency from submersed aquatic plants. Aquat Bot 58:173-179

Zimmerman RC and Kremer JN (1986) *In situ* growth and chemical composition of the giant kelp, *Macrocystis pyrifera* - response to temporal changes in ambient nutrient availability. Mar Ecol Prog Ser 27:277-285